

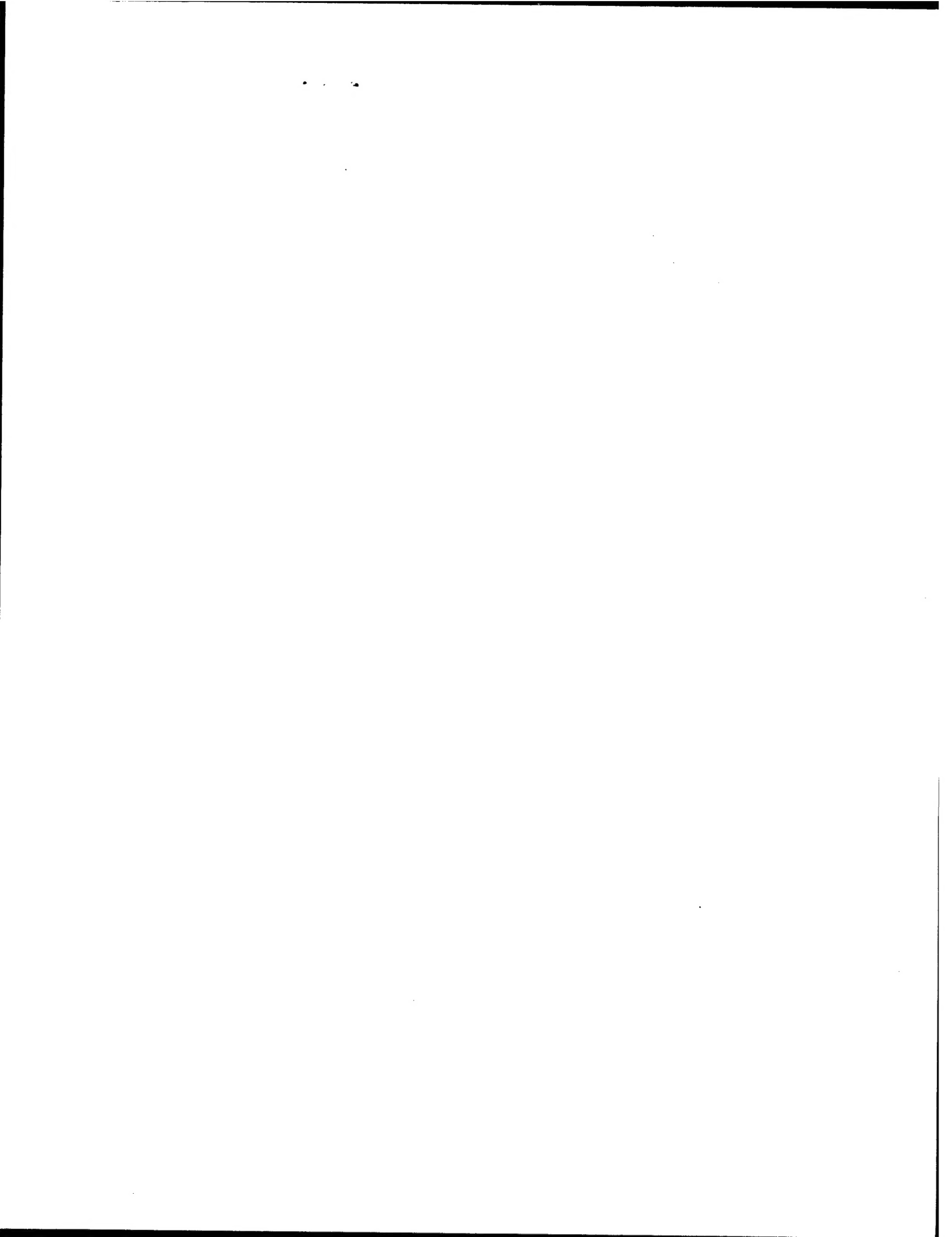
REPORT DOCUMENTATION PAGE

AFRL-SR-BL-TR-01-

0496

**ources,
of this
fferson**

<p>Public reporting burden for this collection of information is estimated to average 1 hour per response, including gathering and maintaining the data needed, and completing and reviewing the collection of information. If you have comments or suggestions for reducing this burden, to Washington Headquarters Service, Davis Highway, Suite 1204, Arlington, VA 22202-4302, and to the Office of Management and Budget, Paperwork Reduction Project 0496-0001.</p>			
1. AGENCY USE ONLY (Leave blank)		2. REPORT DATE August 2001	3. REPORT TYPE FINAL REPORT 1 Jun 97 - 31 May 01
4. TITLE AND SUBTITLE (AASERT97) BIAXIAL FAILURE ANALYSIS OF GRAPHITE REINFORCED POLYIMIDE AND EPOXY FABRIC COMPOSITES		5. FUNDING NUMBERS F49620-97-1-0426 3484/WS 61103D	
6. AUTHOR(S) MACIEJ S. KUMOSA, PAUL K. PREDECKI, B. BENEDIKT, D. DRAGOI, L. KUMOSA, P. RUPNOWSKI, AND D. ARMENTROUT		8. PERFORMING ORGANIZATION REPORT NUMBER	
7. PERFORMING ORGANIZATION NAME(S) AND ADDRESS(ES) UNIVERSITY OF DENVER 2390 SOUTH YORK DENVER, CO 80208		10. SPONSORING/MONITORING AGENCY REPORT NUMBER	
9. SPONSORING/MONITORING AGENCY NAME(S) AND ADDRESS(ES) AIR FORCE OFFICE OF SCIENTIFIC RESEARCH 801 N. RANDOLPH STREET, ROOM 732 ARLINGTON, VA 22203-1977		11. SUPPLEMENTARY NOTES	
12a. DISTRIBUTION AVAILABILITY STATEMENT APPROVED FOR PUBLIC RELEASE, DISTRIBUTION IS UNLIMITED		12b. DISTRIBUTION CODE AIR FORCE OFFICE OF SCIENTIFIC RESEARCH (AFOSR) NOTICE OF TRANSMITTAL DTIC. THIS TECHNICAL REPORT HAS BEEN REVIEWED AND IS APPROVED FOR PUBLIC RELEASE. LAW AFR 190-12. DISTRIBUTION IS UNLIMITED.	
13. ABSTRACT (Maximum 200 words) Comprehensive analyses of residual stresses in unidirectional and fabric graphite/polyimide composites were conducted in this study. In the experimental part of this research, numerous XRD measurements were made to determine residual strains and stresses in embedded Al and Ag inclusions placed in four ply 8 harness satin (8HS) woven and 6 ply unidirectional graphite/PMR-15 composites. In the modeling part of this research, the residual thermal stresses in the unidirectional and woven composites were evaluated by performing linear and visco-elastic computations. In addition, analytical approaches were used to predict the magnitudes of the residual thermal stresses in the composites as a function of temperature, time, composite architecture and external loads. The numerically and analytically determined residual stresses in the composites were subsequently compared to the residual stresses determined from the X-ray analysis in conjunction with the application of the linear elastic and visco-elastic Eshelby models for multiple ellipsoidal inclusions. The effect of external bending loads on the residual strains and stresses in the embedded particles was also experimentally and numerically investigated. A new methodology was proposed for the evaluation of interfacial residual thermal stresses in unidirectional and woven polymer matrix composites based on XRD measurements of residual stresses in embedded crystalline inclusions in conjunction with the application of the visco-elastic Eshelby method for multiple inclusions.			
14. SUBJECT TERMS		15. NUMBER OF PAGES 33	
		16. PRICE CODE	
17. SECURITY CLASSIFICATION OF REPORT U	18. SECURITY CLASSIFICATION OF THIS PAGE U	19. SECURITY CLASSIFICATION OF ABSTRACT U	20. LIMITATION OF ABSTRACT



**BIAXIAL FAILURE ANALYSIS OF GRAPHITE REINFORCED
POLYIMIDE AND EPOXY FABRIC COMPOSITES**

FINAL REPORT

JUNE 1, 1997- AUGUST 31, 2001

TOTAL FUNDING - \$101,000

**MACIEJ S. KUMOSA, PRINCIPAL INVESTIGATOR
PAUL K. PREDECKI, CO-PRINCIPAL INVESTIGATOR**

CONTRIBUTORS:

**B. BENEDIKT, D. DRAGOI, L. KUMOSA, P. RUPNOWSKI
AND D. ARMENTROUT**

**CENTER FOR ADVANCED MATERIALS AND STRUCTURES
DEPARTMENT OF ENGINEERING
UNIVERSITY OF DENVER
2390 SOUTH YORK, DENVER CO 80208**

SPONSORED BY:

**AIR FORCE OF SCIENTIFIC RESEARCH (AFOSR)
UNDER GRANT: F49620-97-1-0426**

20011005 128

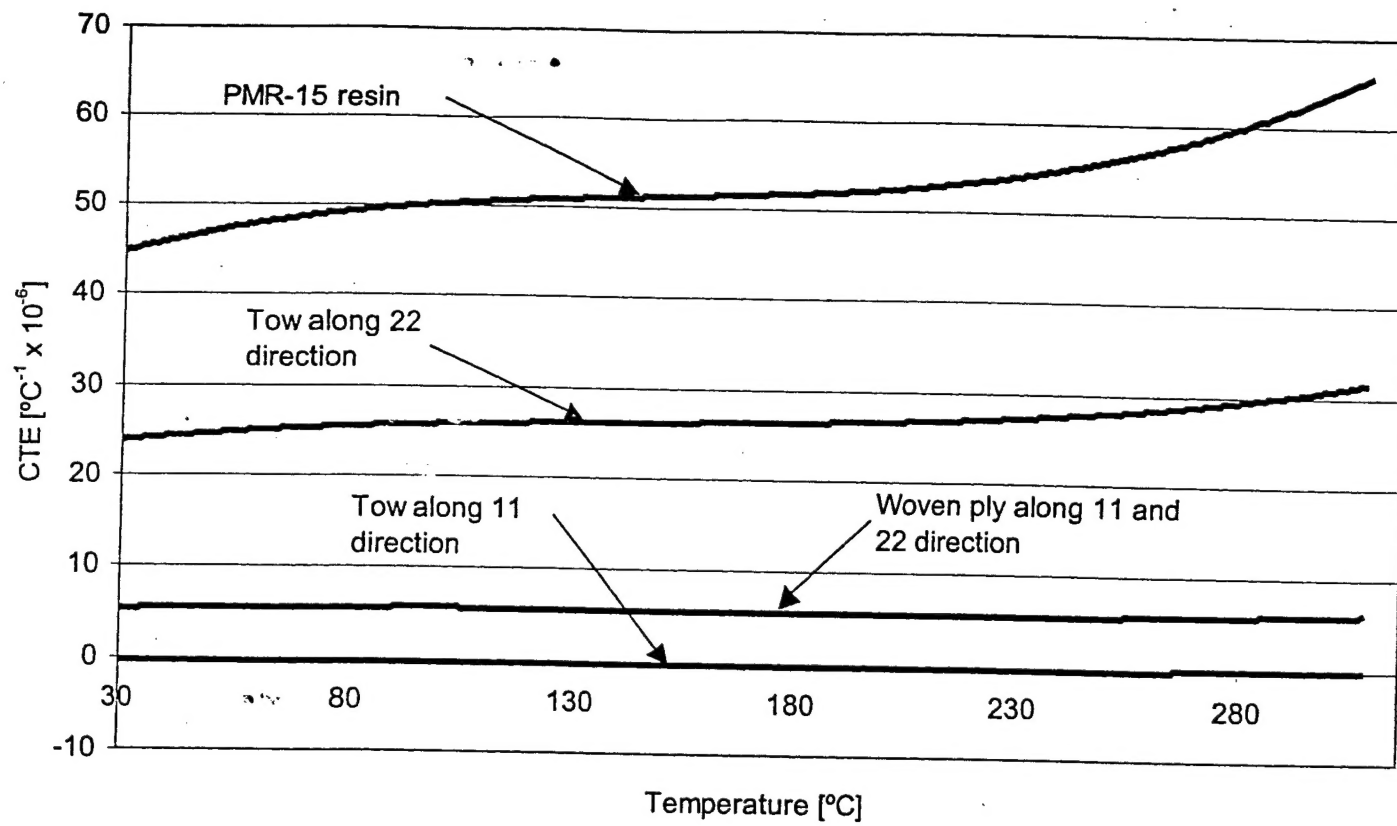


Figure 7

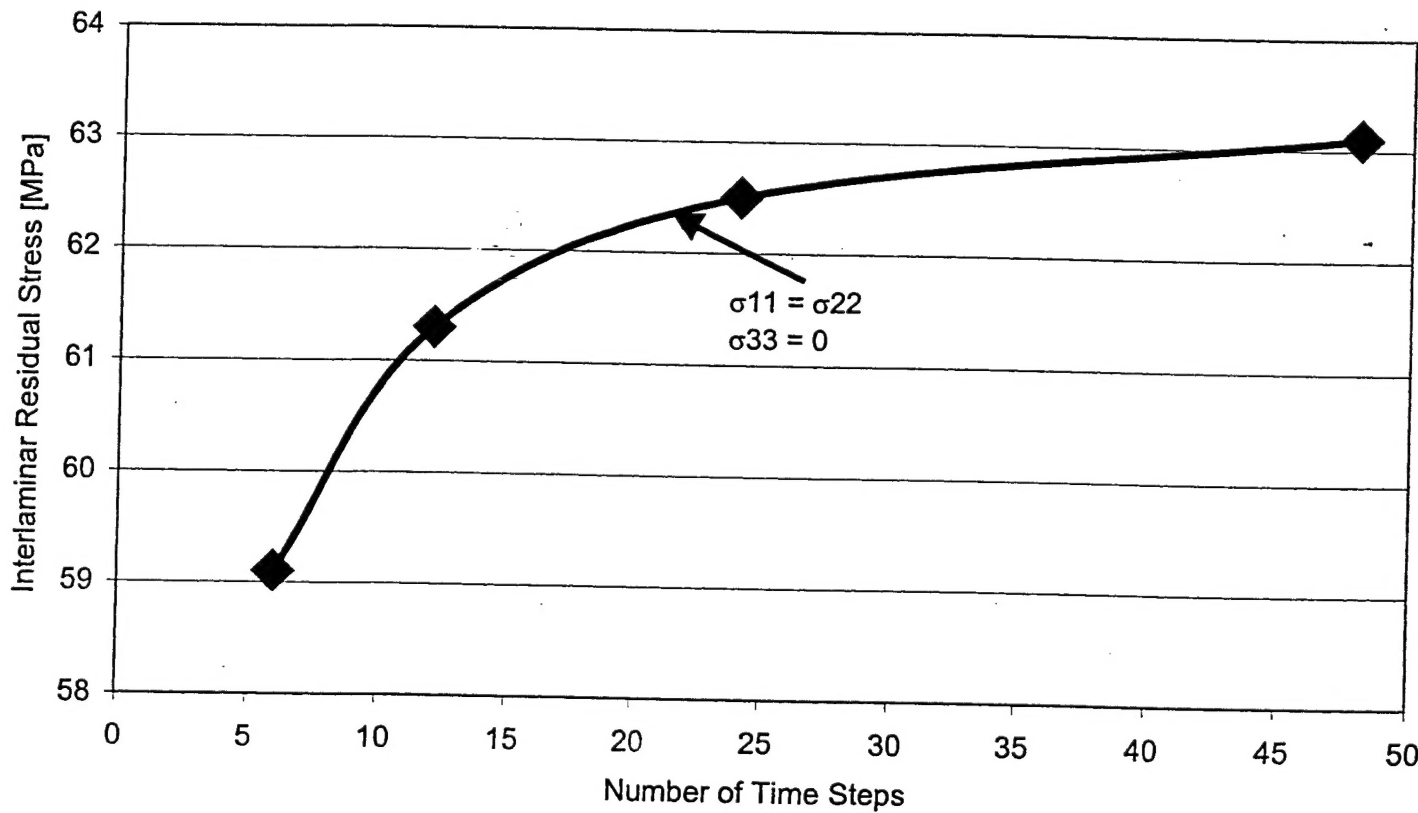


Figure 8

Objectives

The aim of this project was to develop a testing methodology for the evaluation of residual thermal stresses in the polymer matrix of unidirectional and woven polymer matrix composites based on X-ray diffraction (XRD) measurements of thermal residual strains in embedded crystalline particles.

Abstract

Comprehensive analyses of residual stresses in unidirectional and fabric graphite/polyimide composites were conducted in this study. In the experimental part of this research, numerous XRD measurements were made to determine residual strains and stresses in embedded Al and Ag inclusions placed in four ply 8 harness satin (8HS) woven and 6 ply unidirectional graphite/PMR-15 composites. In the modeling part of this research, the residual thermal stresses in the unidirectional and woven composites were evaluated by performing linear and visco-elastic computations. In addition, analytical approaches were used to predict the magnitudes of the residual thermal stresses in the composites as a function of temperature, time, composite architecture and external loads. The numerically and analytically determined residual stresses in the composites were subsequently compared to the residual stresses determined from the X-ray analysis in conjunction with the application of the linear elastic and visco-elastic Eshelby models for multiple ellipsoidal inclusions. The effect of external bending loads on the residual strains and stresses in the embedded particles was also experimentally and numerically investigated. A new methodology was proposed for the evaluation of interlaminar residual thermal stresses in unidirectional and woven polymer matrix composites based on XRD measurements of residual stresses in embedded crystalline inclusions in conjunction with the application of the visco-elastic Eshelby method for multiple inclusions.

Executive Summary

1. Introduction

Residual thermal stresses in embedded crystalline particles in polymer matrix composites were first measured by Predecki and Barrett [1-3] by performing XRD measurements. They found that the residual and applied strains transferred to various crystalline particles were high enough to be detected by XRD. However, knowing the state of strain in the particles, they were unable to determine the actual residual stresses in the surrounding polymer matrix. In the initial stages of this project, preliminary XRD analyses of the residual thermal stresses in unidirectional and woven graphite/PMR-15 composites were conducted by D. Dragoi and the results were presented in his Ph.D. thesis entitled "Residual Stress Analysis of Graphite/Polyimide Composites using the Concept of Metallic Inclusions" [4]. The preliminary results clearly showed that the residual stresses in Al and Ag inclusions could be measured if the inclusions are embedded in a polymer resin between the first and second ply in six ply unidirectional and four ply woven fabric graphite/polyimide (PMR-15) composite plates. However, the actual determination of the residual interlaminar thermal stresses in the composites from the strains and stresses in the embedded inclusions between the plies was found to be much more complex than was initially assumed. The simple linear elastic model developed by Dragoi turned out to be highly insufficient for the proper evaluation of the state of stress in the polyimide matrix. The preliminary research performed by D. Dragoi had to be significantly expanded in order to determine the magnitudes of the residual stresses in the composites with a significantly higher degree of accuracy. Therefore, additional research efforts were undertaken in the remaining two years of the project to improve the accuracy of the XRD measurements and to provide a comprehensive numerical/analytical methodology which could allow the proper evaluation of the actual thermal stresses in the composites from the residual strains and stresses in the embedded particles. In order to accomplish these tasks, comprehensive elastic and visco-elastic numerical/analytical calculations of residual stresses in unidirectional and woven graphite/polyimide composites were performed [5-7]. In addition, numerous XRD measurements were made on unidirectional and woven (8HS) graphite/PMR-15 composite specimens with embedded Al and Ag inclusions to assess the accuracy of the measured X-ray strains and stresses and the point-to-point variation of these quantities in the laminates [5-7]. The XRD measurements were conducted on the composite specimens with and without external bending loads. In the tests with external

loads, the composite specimens were subjected to four point bending and the residual strains and stresses in Al and Ag particles were determined as a function of load.

2. Numerical Calculations of Interlaminar Residual Thermal Stresses in Unidirectional and Woven Graphite/PMR-15 Laminates

2.1 Linear elastic computation of residual stresses

Using linear elastic classical laminate theory, the distributions of the thermal residual stresses and strains in unidirectional and woven 8HS graphite/PMR-15 composite laminates were determined [5-7]. The analytical predictions were subsequently checked by performing two and three-dimensional finite element computations. The distributions of the thermal residual stresses and strains in the laminates were obtained as a function of the thickness of the polyimide layer between the unidirectional composite plies. Excellent agreements were achieved between the results from the application of the laminate theory and the linear elastic finite element computations.

Since the unidirectional and woven graphite/PMR-15 specimens in the X-ray diffraction tests were subjected to four point bending, the internal stress and strain distributions in the two types of composite plates were determined by subjecting the specimen to four point bending simulating the experimental conditions. The following methods were used:

- Levi method (the solution is expanded in Fourier series)
- variational Raleigh - Ritz method
- one dimensional approximation
- two and three-dimensional finite element computations

The deformation, internal stresses and strains from the analytical and numerical predictions were found to be very close to each other. By superimposing the solutions of the residual stresses and strains from the thermal analysis with the stress and strain solutions under four point bending, the total stresses and strains in the laminates were determined under linear elastic conditions.

The distribution of the thermal residual stresses and strains was also obtained for a unidirectional composite laminate without the presence of polymer layers [5]. The Tanaka Mori approach, a modification of the Eshelby method with multiple inclusions (graphite

fibers), was employed to evaluate the average stresses and strains due to temperature change. This approach allowed the determination of the intralaminar residual stresses and strains in the unidirectional composite. Thus, the combined effect of temperature and bending on the stress and strain distributions in the unidirectional composite plate could be evaluated for both the intralaminar and interlaminar situations. From the above analytical and numerical computations, the upper limits of the residual and applied (from bending) interlaminar and intralaminar stresses in the unidirectional composite were established.

2.2 Visco-elastic models of interlaminar residual thermal stresses

A visco-elastic analysis with nonisothermal conditions in conjunction with classical lamination theory was used to determine the effects of curing temperature history on residual stresses in the unidirectional graphite/PMR-15 composite plate [5,6]. In this case, the time-dependent stresses and strains are also functions of the temperature. The calculations were performed, following the numerical procedure presented in Ref. 8, assuming that the thermal expansion coefficients of the polymer layer and the unidirectional plies can be non-linear functions of temperature and that the elastic properties of the polymer and composite layers are also strongly dependent on time and temperature. The thermal expansion coefficients and elastic properties for the PMR-15 resin were provided by NASA Glenn [9]. These properties of the unidirectional composite plies were determined using the Hashin model [10]. The results from the visco-elastic analysis indicated that the residual thermal stresses were substantially reduced in comparison to the linear elastic prediction. For the temperature cycle simulating the actual manufacturing process the residual stresses were reduced by 35 to 40% [5].

In the next stage, the visco-elastic approach was employed to evaluate the effects of temperature and time on the residual thermal stresses in the woven graphite/PMR-15 composite [7]. The stiffness properties and thermal expansion coefficients of the woven plies were numerically determined using the bridging model proposed by Ishikawa and Chou [11-13]. The geometrical properties of the woven composite were taken from Ref. 14. The properties of the tows were numerically determined [7] as a function of time and temperature assuming that the tows are unidirectional composites that were made from a visco-elastic polymer matrix reinforced by transversely isotropic fibers with their properties independent of time and temperature. Then, visco-elastic plate theory was used to predict the interlaminar thermal residual stresses in the polymer plies of the investigated 8HS laminate. The convergence of the solution was checked by performing the calculations for

various numbers of time steps (from 6 up to 48 time steps) covering the final stages of the post curing cycle. Similar to the analysis of the residual stresses in the unidirectional system [5], the residual stress in the woven composite at 315°C of the post curing cycle were assumed to be zero. The manufacturing cycles for the unidirectional and woven systems were provided by NASA Glenn.

The numerical and analytical results of the residual thermal stresses clearly indicate that the linear elastic predictions grossly overestimate the magnitudes of the residual stresses in the unidirectional and woven graphite/PMR-15 composite. The stresses are also significantly affected by the curing cycle and are strongly dependent on the magnitude of the thermal-expansion coefficient of the polymer resin and its change with temperature. It is clear that for the accurate determination of the residual stresses either numerically or analytically, the actual physical time and temperature dependent properties of unidirectional and woven composite (elastic constants, thermal-expansion coefficients) must be known a priori for a particular composite system.

3. X-Ray Diffraction Measurements

3.1 SEM analyses of Ag and Al inclusions

The distribution of the Al and Ag particles in the unidirectional and woven graphite/PMR-15 composite specimens used in the X-ray diffraction measurements was examined using scanning electron microscopy [5,7]. It was found that the distributions were not uniform and varied significantly even within one specimen. The average volume fraction of the inclusions could also vary significantly from specimen to specimen. The average volume fraction of the Al inclusions ($40 \pm 7\%$) is noticeably higher than that of the Ag inclusions ($25 \pm 6\%$) in the unidirectional composite. It was also found that the Al inclusions were spherical in nature and possessed a wide size distribution ($1-30\mu\text{m}$). However, the shape of the Ag inclusions was irregular and the size was quite uniform ($2-3\mu\text{m}$) but smaller than the Al particles. The distributions of the particles in the woven specimens were similarly non-uniform.

3.2 Acid digestion, thermal mechanical and gravimetric analyses.

Acid digestion tests and thermal mechanical and gravimetric (TMA and TGA) analyses were performed at NASA Glenn to determine void and fiber contents as well as the glass transition T_g and decomposition T_d temperatures of the investigated composites. The data from these tests are presented in Refs. 5-7.

3.3 X-Ray diffraction measurements

XRD measurements were performed on four types of specimens, namely unidirectional and woven (8HS) graphite/PMR-15 composites with embedded either Al or Ag particles [5-7] using the approaches described in Refs. 1-3. For each system, fiber orientation and type of inclusion, several XRD measurements were made to evaluate the reproducibility of the X-ray data and to evaluate the effect of non-uniformity in the distribution of inclusions on the X-ray results. Temperature and relative humidity were closely monitored during the measurements, and the data corrected for changes in ambient temperature. Two types of XRD experiments were performed. In the first case, unidirectional and woven composite specimens with the embedded particles were tested without external loads. Each specimen was first placed on a glass plate before it was inserted into a Siemens D-500 diffractometer with pseudo-parallel beam optics and a solid-state detector. In the second case, the specimen (either unidirectional or woven) was mounted into a four-point bend fixture (designed and manufactured in this project) and subsequently placed into the diffractometer. In both cases, the specimen location was checked with a dial gage and micro flat accurate to 0.025 mm. Then, the residual thermal strains in the embedded particles (with and without bending) were determined in both the composite systems [5-7].

Despite the fact that noticeable scatter was detected in the residual strains and stresses in the particles for each system, the results showed several important trends. Most importantly, the X-ray strains and stresses in the particles were quite symmetric in the case of the woven specimens [7], with the magnitudes of the stresses along the tow and fill directions being very similar. In the unidirectional specimens the largest residual stresses in the particles were determined along the fibers with the in-plane stresses in the direction perpendicular to the fibers approximately two times smaller [5]. In both cases, the residual stresses in the particles through the thickness were found to be non zero and much larger in the fabric specimens [7].

4. Determination of Residual Thermal Stresses in Unidirectional and Woven Composites from the X-Ray Residual Strains in Al and Ag Particles

The magnitudes of the thermal residual strains in the unidirectional and woven graphite/polyimide composites cannot be directly determined from the residual X-ray strains and stresses in the Al and Ag particles. The X-ray strains in the particles contain two components assumed to be additive. The first component is the local strain caused by the difference in the thermal-expansion coefficients and the elastic properties of the particles and the surrounding polymer matrix. The second component is generated by the global residual strains in the composite caused by the difference in the thermal-expansion coefficients and elastic properties between the polymer layer containing the particles and the overall composite. Therefore, for the proper evaluation of the global residual strains in the composites, the local interaction between the particles and the polymer resin in the interlaminar model must be determined. However, the local strains in the particles are also highly dependent on the temperature cycle. They also depend very strongly on the local volume fraction of inclusions in the irradiated volume during XRD measurements, and the overall shape of the inclusions. One of the methods which could be used for this purpose is the visco-elastic Eshelby method for multiple ellipsoidal inclusions [15-17]. Major efforts were undertaken to determine the local strains and stresses in the Al and Ag inclusions using this method. The local strains and stresses in the inclusions were calculated as a function of the volume fraction of inclusions, their geometry and the temperature cycle (as a function of time and temperature). After determining the global residual strains and stresses in the polymer matrix of the composites from the local strains in the particles (using the visco-elastic Eshelby approach) and the experimental X-ray strains in the particles, the global thermal residual strains and stresses in the polymer matrix obtained from these analyses were compared to the global residual strains and stresses in the composites from the visco-elastic laminate computations. As an example, the interlaminar residual stresses in the 8HS composite determined from the XRD measurements using Al inclusions and plate theory are shown in Table 1.

Table 1. Interlaminar residual thermal stresses in the 8HS composite from XRD measurements and the Eshelby model as well as from laminated plate theory with linear-elastic and visco-elastic assumptions

	X-Ray with Eshelby			Plate theory		
	σ_{11} [MPa]	σ_{22} [MPa]	σ_{33} [MPa]	σ_{11} [MPa]	σ_{22} [MPa]	σ_{33} [MPa]
Linear elastic	70.7 ± 17	71.1 ± 17	36.7 ± 16	94	94	0
Visco-elastic	67.3 ± 17	67.6 ± 16	33 ± 16	63.1	63.1	0

The average interlaminar residual thermal stresses determined from the XRD data with the application of the visco-elastic Eshelby model for multiple inclusions in the unidirectional and woven graphite/PMR-15 systems are presented in Table 2. The data presented in this table were obtained from the XRD tests performed with and without four point bending.

Table 2. Comparison between the interlaminar residual stresses in the unidirectional and woven (8HS) graphite/PMR-15 composites.

	Excluding bending			Including bending			Volume fraction of Al inclusions
	σ_{11} [MPa]	σ_{22} [MPa]	σ_{33} [MPa]	σ_{11} [MPa]	σ_{22} [MPa]	σ_{33} [MPa]	
unidirectional	53.5 ± 9	39.6 ± 8	25 ± 5	55 ± 6	40.5 ± 5	26.6 ± 4	40 ± 7%
8HS woven	67.3 ± 17	67.6 ± 16	33 ± 16	62.3 ± 8	61.7 ± 8	27.6 ± 7	46 ± 7.4%

It can be seen that the magnitudes of the interlaminar residual stresses along the fibers (σ_{11} , unidirectional) and along the tows ($\sigma_{11}=\sigma_{22}$, 8HS) in the both graphite/PMR-15 systems are high. The scatter in the XRD measurements is predominately caused by the non-uniform distribution of the particles and the non-uniform distribution of residual stresses in the composites. It should be strongly emphasized here that the accuracy of the entire analysis of the residual stresses is very strongly dependent on the physical properties

of the investigated composite system. The temperature and time dependent physical properties of the composites and inclusions must be known for the accurate determination of the residual stresses either from laminate theory or from XRD measurements.

5. Major Conclusions from the Performed Study

1. A new methodology for the evaluation of interlaminar residual thermal stresses in unidirectional and woven polymer matrix composites based on XRD measurements of residual stresses in embedded crystalline inclusions in conjunction with the application of the visco-elastic Eshelby method for multiple inclusions was proposed. It was successfully applied to the determination of the interlaminar residual thermal stresses in unidirectional and woven (8 harness satin) graphite/PMR-15 composites.
2. The best agreement between numerically predicted interlaminar thermal stresses and the stresses determined by X-ray and the Eshelby model was obtained when Al inclusions were used. A strong effect of particle shape on the measured X-ray stresses was found. In particular, the highly irregular Ag particles significantly overestimated the residual stresses in the composite if the shape of the particles was assumed to be spherical. Despite the fact that the distribution of the particles was not purely interlaminar, the residual stresses in the composites determined from the analysis agreed quite well with the interlaminar assumptions both for the unidirectional and woven (8HS) systems. The accuracy of the method could be significantly increased if the distribution of either interlaminar or intralaminar particles was strictly controlled.
3. The interlaminar residual stresses in the unidirectional and 8HS composites were found to be three dimensional in nature with significant stresses present between the plies in the thickness direction of the specimens. These stresses cannot be determined using visco-elastic laminated plate theory. The stresses are caused by the non-uniform thickness of the polyimide layer between either unidirectional or woven plies.
4. The newly developed methodology for the evaluation of residual strains and stresses inside crystalline particles embedded in unidirectional and woven polymer matrix composites was further verified by performing additional XRD measurements of internal strains and stresses inside Al inclusions embedded in unidirectional and woven graphite/PMR-15 composite specimens subjected to four point bending conditions. The X-ray strains in the particles were found to be linearly dependent on the applied axial strain in

the specimens caused by four-point bending. The magnitudes of the total strains ϵ_{11} and ϵ_{33} in the particles increased linearly with increasing applied strain. However, the effect of bending on the ϵ_{22} strain component inside the inclusions was found to be negligible. The change in the strain components ϵ_{11} and ϵ_{22} inside the Al inclusions as a function of bending can be quite accurately predicted using laminate theory with an interlaminar distribution of the particles in conjunction with the application of the Eshelby method for multiple inclusions. The ϵ_{33} strain component inside the inclusions differs significantly however from the numerical predictions. Very similar observations were made with respect to the stress components inside the inclusions.

5. The thermal residual stresses in the interlaminar regions of the 8HS woven graphite/PMR-15 composite were noticeably higher than in the case of the unidirectional system. Especially, the large tensile stresses along the tows (62.3 ± 8 MPa) might create cracking of the polyimide layers in service since they are only slightly lower than the tensile strength of the PMR-15 resin, which is approximately 80 MPa. They might be even higher in graphite/polyimide composite structures subjected to large temperature variations in-service.

References

1. P. Predecki and C. S. Barrett, Stress Measurement in Graphite/Epoxy Composites by X-ray Diffraction from Fillers, *J. Comp. Mat.*, vol. 13, p. 61-71, 1979
2. P. Predecki, C. S. Barrett, Residual Stresses in Resin Matrix Composites, In E. Kula, editor, *28th Sagamore Army Materials Research Conference*, p. 409-424, Lake Placid, July 13-17 1981
3. C. S. Barrett and P. Predecki, Stress Measurements in Graphite/Epoxy Uniaxial Composites by X-rays, *Polymer Composites*, vol. 1, p. 2-6, 1980
4. D. Dragoi, Residual Stress Analysis of Graphite/Polyimide Composites Using the Concept of Metallic Inclusions, Ph.D. Thesis, Department of Engineering, University of Denver, Denver, Colorado, June 1999.
5. B. Benedikt, M. Kumosa, P.K. Predecki, L. Kumosa, M.G. Castelli and J. K. Sutter, An Analysis of Residual Thermal Stresses in a Unidirectional Graphite/PMR-15 Composite Based on the X-ray Diffraction Measurements, *Composite Science and Technology*, in press.
6. B. Benedikt, P. K. Predecki, L. Kumosa, D. Armentrout, J. K. Sutter and M. Kumosa, The Use of X-ray Diffraction Measurements to Determine the Effect of Bending

Loads on Internal Stresses in Aluminum Inclusions Embedded in a Unidirectional Graphite Fiber /PMR-15 Composite, *Composites Science and Technology*, in press.

7. B. Benedikt, P. Rupnowski, L. Kumosa, J. K. Sutter, P.K. Predecki and M. Kumosa, Determination of Interlaminar Residual Thermal Stresses in a Woven 8HS Graphite/PMR-15 Composite Using X-Ray Diffraction Measurements, *Mechanics of Composite Materials and Structures*, submitted (August 2001).
8. T. M. Wang and M. Daniel, Thermoviscoelastic Analysis of Residual Stresses and Warpage in Composite Laminates, *Journal of Composite Materials*, vol. 26, p. 883-899, 1992
9. G. D. Roberts, D. C. Malarik and J. O. Robaidek, Viscoelastic Properties of Addition-Cured Polyimides Used in High Temperature Polymer Matrix Composites, Composites Design, Manufacturing, and Applications; *Proceedings of the Eight International Conference on Composite Materials*, S. W. Tsai and G. S. Springer, Eds., Society for Advanced Materials and Process Engineering, Covina, CA 1991, p. 12-H-1 to 12-H-10
10. Z. Hashin, Analysis of Properties of Fiber Composites with Anisotropic Constituents, *Journal of Applied Mechanics*, vol. 46, p. 543-550, 1979
11. T. Ishikawa and T.W. Chou, Nonlinear Behavior of Woven Fabric Composites, *Journal of Composite Materials*, vol. 17, p.399-413, 1983
12. T. Ishikawa and T.W. Chou, In-plane Thermal Expansion and Thermal Bending Coefficients of Fabric Composites, *Journal of Composite Materials*, vol. 17, p.92-104, 1983
13. T. W. Chou, Microstructural Design of Fiber Composites, *Cambridge University Press*, Cambridge 1992
14. K. Searles, G. Odegard, M. Kumosa, Micro- and Mesomechanics of 8-Harness Satin Woven Fabric Composites: I. Evaluation of Elastic Behavior, *Composites: Part A applied science and manufacturing*, in press.
15. J. D. Eshelby, The Determination of the Elastic Field of an Ellipsoidal inclusion, and Related Problems, *Proc. R. Soc. London*, vol. A241, p. 376-396, 1957
16. T. Mura, *Micromechanics of Defects in Solids*, 2nd edition, Martinus Nijhoff Publishers, Dordrecht, 1987
17. T. Mori and K. Tanaka, Average Stress in Matrix and Average Elastic Energy of Materials with Misfitting Inclusions, *Acta Metall.*, vol. 21, p. 571-574, 1973

Publications based on this study

The following manuscripts have been prepared based on the research performed in this project. The most important publications (#1, #2 and #5) are attached.

1. B. Benedikt, M. Kumosa, P.K. Predecki, M.G. Castelli and J.K. Sutter, An Analysis of Residual Thermal Stresses in a Unidirectional Graphite/PMR-15 Composite Based on the X-ray Diffraction Measurements, *Composites Science and Technology*, in press (2001).
2. B. Benedikt, P. Predecki, L. Kumosa, D. Armentrout, J. K. Sutter and M. Kumosa, The Use of X-Ray Diffraction Measurements to Determine the Effect of Bending Loads on Internal Stresses in Aluminum Inclusions Embedded in a Unidirectional Graphite/PMR-15 Composite, *Composites Science and Technology*, in press (2001).
3. M. Kumosa, P.K. Predecki, G. Odegard, K. Searles, B. Benedikt, D. Armentrout, L. Kumosa, M. Gentz and J.K. Sutter, Analysis of Failure Mechanisms and Residual Stresses in Unidirectional and Woven Graphite/PMR-15 Composites Subjected to Shear Dominated Biaxial Loads, HIGH TEMPLE Workshop XXI, 12-15 February 2001, Clearwater Beach, Florida.
4. B. Benedikt, P.K. Predecki, L. Kumosa, P. Rupnowski and M. Kumosa, Measurements of Residual Stresses in Polymer Matrix Fiber Reinforced Composites Based on X-ray Diffraction, presented at the 50th Annual Denver X-Ray Conference, July 30 - August 3, 2001 , to be published in the conference proceeding in October 2001.
5. B. Benedikt, P. Rupnowski, L. Kumosa, J. K. Sutter, P.K. Predecki and M. Kumosa, Determination of Interlaminar Residual Thermal Stresses in a Woven 8HS Graphite/PMR-15 Composite Using X-Ray Diffraction Measurements, *Mechanics of Composite Materials and Structures*, submitted (August 2001).

Dissertations

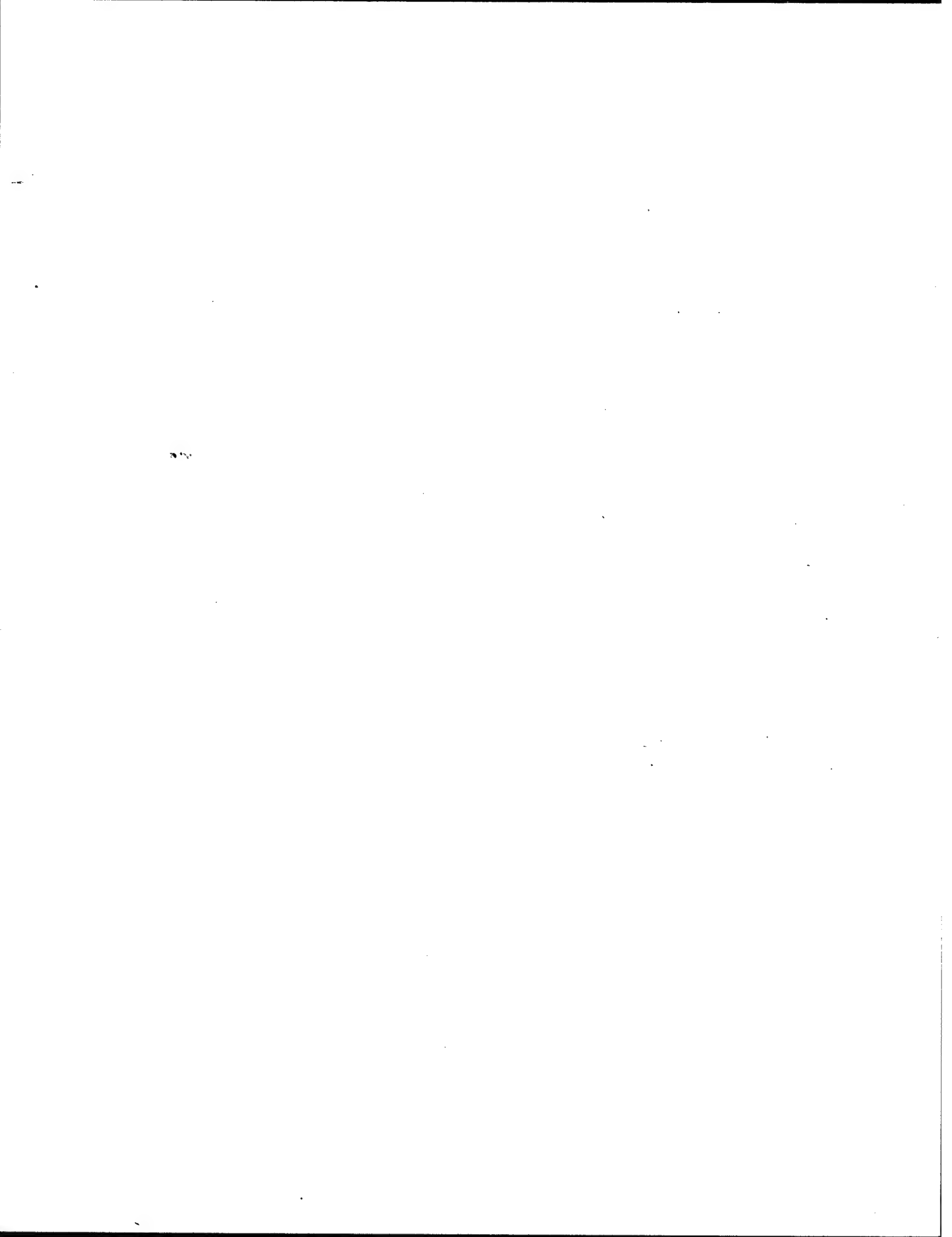
1. D. Dragoi, Residual Stress Analysis of Graphite/Polyimide Composites Using the Concept of Metallic Inclusions, Ph.D. Thesis, Department of Engineering, University of Denver, Denver, Colorado, June 1999.
2. B. Benedikt, Evaluation of Residual Thermal Stresses in Graphite/Polymer Matrix Unidirectional and Woven Composites Based on X-ray Diffraction Measurements (preliminary title), to be completed in August 2002.

Personnel Supported

Two Ph.D. graduate students (D. Dragoi and B. Benedikt) and one undergraduate research assistant (L. Kumosa) were involved in this project. D. Dragoi graduated in June 1999 with a Ph.D. in Materials Science from the Department of Engineering at the University of Denver. For the remaining two years of the study Mr. B. Benedikt was hired. Mr. Benedikt should graduate with a Ph.D. in Materials Science in August 2002. The students were jointly supervised by Dr. M. Kumosa and Dr. P. Predecki.

Interactions

This study was performed in close collaboration with the NASA Glenn Research Center (Mr. M. Castelli and Dr. J. K. Sutter). NASA provided all composites tested in this study. In addition, NASA provided the physical characterizations of the tested composites. Numerous technical discussions with the NASA personnel took place during the progress of this study.



Composites Science & Technology, in press.

**An Analysis of Residual Thermal Stresses in a Unidirectional
Graphite/PMR-15 Composite Based on the X-Ray Diffraction
Measurements**

B. Benedikt, M. Kumosa, P. K. Predecki, L. Kumosa, M. G. Castelli*
and J. K. Sutter*

**Center for Advanced Materials and Structures
Department of Engineering
University of Denver
2390 South York St., Denver, Colorado 80208**

***NASA Glenn Research Center at Lewis Field
21000 Brookpark Rd.
Cleveland, OH 44135**

Abstract

The purpose of this research is to determine residual thermal stresses in a unidirectional graphite/PMR-15 polyimide composite using crystalline inclusions. X-ray diffraction (XRD) measurements have been made to determine residual stresses in embedded Al and Ag inclusions placed between the first and second ply of six ply unidirectional graphite/PMR-15 composite specimens. In the modeling part of this research, residual thermal stresses in unidirectional graphite/polyimide composite plates and in the embedded Al and Ag inclusions with interlaminar and intralaminar particle distributions have been modeled using elastic and visco-elastic laminate theories and the Eshelby method. The numerically determined residual stresses in the particles have been subsequently compared to the residual stresses determined from the XRD analysis. It has been shown in this research that the residual stresses in the unidirectional graphite/polyimide composite can be obtained with a reasonable accuracy by using the X-

X-ray diffraction technique in conjunction with the application of the visco-elastic Eshelby method of multiple inclusions. The modeling has also shown that the distribution of the Al and Ag particles and their geometries have a strong effect on the XRD data and the thermal stress analysis based on the concept of embedded crystalline inclusions.

1. Introduction

A direct consequence of the shrinkage of the polymeric matrix around the reinforcement during cooling is the creation of residual stresses. These stresses exist on both macroscopic and microscopic scales. Tensile residual stresses in the matrix are particularly important since they may significantly decrease the strength of the polymer and can lead to premature fracture of a composite structure. Prediction and measurement of residual stresses become therefore important in relation to production, design and performance of composite materials.

Numerous methods have been developed to determine both experimentally and analytically the residual stresses in polymer matrix composites. Generally one can divide all experimental methods into two categories, namely destructive and non-destructive methods. The basic drawback of destructive methods (hole drilling [1], sectioning/cutting [2], first ply failure test [3]) is the fact that they can not be used for in situ measurements, since they require the specimen to be destroyed during testing. The second category – non-destructive methods includes among others warpage measurements on laminated composites [4], the cure reference method [5] and methods using embedded sensors such as strain gages, fiber optics [6] or crystalline materials with a diffraction method (X-ray or neutron). The warpage measurement can be used only for unsymmetrical ply sequences, which makes this method useless for other laminate architectures. Jeronimidis and Parkyn [7] used classical laminated plate theory [8] to determine the residual stresses in a composite plate taking into account the changes in thermoelastic properties of the composite plies. A time dependent model, also based on classical laminated plate theory, was described by Wang et al. [9]. The unidirectional composite was assumed to be thermorheologically simple and the time-temperature superposition principle was used to

obtain a master curve for viscoelastic properties. Finite elements computations of process-induced residual stresses during cure were presented by White et al. [10]. In that paper, the influence of stress relaxation time, equilibrium modulus, the level of chemical shrinkage, and curing conditions on residual stresses before cool-down were discussed.

Residual stresses inside embedded crystalline particles in polymer matrix composites were first measured by Predecki and Barrett [11-13] by performing XRD measurements. It was found that residual and applied strains transferred to various crystalline particles were high enough to be detected by X-ray diffraction. However, knowing the state of strain in the particles, they were unable to determine the actual residual stresses in the surrounding polymer resin. Recently Dragoi [14] has made an attempt to calculate matrix residual stresses based on measured (X-ray diffraction) strains in Al and Ag inclusions embedded in graphite/polyimide unidirectional and fabric composites, but his simple linear elastic model turned out to be insufficient for the proper evaluations of the state of stress in the polyimide matrix.

The purpose of this study is to develop a testing methodology for the most accurate evaluation of residual stresses in the polymer matrix of a unidirectional polymer matrix composite based on XRD measurements of residual stresses in embedded crystalline particles. At first, the residual thermal stresses in a unidirectional graphite polyimide composite were determined by performing visco-elastic computations assuming interlaminar (Figure 1a) and intralaminar (Figure 1b) composite architectures. Secondly, the residual stresses in Al and Ag particles were obtained through XRD measurements and from the application of the visco-elastic Eshelby method for multiple ellipsoidal inclusions [16-18]. Finally, the residual stresses in the polymer matrix were extracted from the X-ray stresses in the particles and subsequently compared with the stresses obtained from the interlaminar and intralaminar analyses.

2. Experimental Procedures

XRD measurements were made on several unidirectional six ply graphite/PMR-15 specimens with Al and Ag inclusions. The particles were embedded between the first and second ply. A detailed SEM analysis of particle distribution was also performed and shown in Figures 2-5.

2.1 Materials Tested

Unidirectional composite plates with and without embedded Al and Ag inclusions were manufactured at the NASA Glenn Research Center in the form of three 152 x 152 mm plates per the following specifications:

Fibers:	T650-35
Matrix:	PMR-15
Ply arrangement:	six ply unidirectional
Cure:	simulated autoclave and postcure: a laminate was prepared by using a commercially supplied prepreg consisting of 6 plies of graphite fiber fabric/PMR-15 cut and stacked together in a steel mold. In the mold, the prepreg was symmetrically placed between the following processing aids: non-porous Teflon® peel ply, 2 layers of E-glass, and porous Teflon® peel ply. The non-porous plies were placed on the outside (mold-side) of the ply lay-up. The porous peeled plies sandwiched the prepreg. Finally, an about 6 mm thick steel plate was placed on top of the nonporous peel ply and the 6 plies of prepreg. The mold was covered in a large sheet of 50 µm thick Kapton® and secured with a metal frame to ensure a vacuum during processing. The steel mold containing the 6 plies of prepreg was placed in a hydraulic press at room temperature. Stops were inserted between the press platens to prevent excessive resin flow during the initial heating stages of the processing cycle. Vacuum (150mm Hg) was applied to the mold and the Kapton® quickly conformed to the 6 mm thick tool containing the prepreg. The press was heated at 2.8°C/minute until the mold temperature reached 149°C, then the vacuum was increased to 625 mm Hg, after which the press was further heated at a ramp rate of 1.1°C /minute until the mold temperature reached 232°C

and was maintained at that temperature for 60 minutes. After this hold at 232 °C, a pressure of 1.38 MPa was applied to the mold and the mold temperature was ramped up to 315°C at the same ramp rate of 1.1°C /minute. The mold was then held at 315°C for 120 minutes and then cooled to 204°C over three hours.

The plates were post cured in air in the following five steps:

- Step 1. From room temperature to 246° C in 100 min (no hold).
- Step 2. From 246° C to 288° C in 150 min and hold at 288° C for 300 min.
- Step 3. Ramp to 315° C in 100 min and hold at 315° C for 600 min.
- Step 4. Cool to 204° C in 50 min (no hold).
- Step 5. Cool to room temperature over 180 min.

The plates were C-scanned at NASA GRC using through-transmission techniques with a Physical Acoustic Corp. Model UPKI-T equipped with a 5MHz transducer. The thickness of the plates was measured in eight randomly selected locations. The average thickness of the three plates was found to be

Plate A (with Al inclusions)	1.035 mm, ranging from 1.016 mm to 1.067 mm
Plate B (with Ag inclusions)	1.038 mm, ranging from 1.016 mm to 1.067 mm
Plate C (without inclusions)	1.035 mm, ranging from 0.991 mm to 1.067 mm

In addition, acid digestion tests were performed at NASA to determine void and fiber contents in the three composite plates following the accepted ASTM standards: ASTM D2734-70 and ASTM D3171-76, respectively. Three samples were taken from three different locations for each plate. The samples were taken approximately 10 mm from the edges. The results from the acid digestion tests are shown in Table 1. The negative values given for the void volume (*) are due to the assumptions made for theoretical densities of just the resin and fibers. Therefore, the actual density measurements do not account for the metal particles being embedded in the composites. This should also slightly affect the

fiber volume measurements. However, cross-sectional micrographs confirmed that the void volumes were less than 2%.

Thermal mechanical and gravimetric analyses (TMA and TGA) were performed on TA Instruments Models 2940 and 2950, respectively. Both analyses were conducted at a heating rate of $10^{\circ}\text{C}/\text{min}$. Glass transition (T_g) and decomposition (T_d) temperatures determined from TMA and TGA experiments were calculated from the intersection of lines tangent to the knee of their respective transitions. All T_g and T_d values were determined while heating the composites in an air environment. The glass transition and decomposition temperatures for the three plates are shown in Table 2.

2.2 SEM Analyses of Particle Distributions

The distributions of the Al and Ag particles in the composite specimens were determined using scanning electron microscopy. Three samples of each material were prepared for the SEM study from three different locations of the as supplied composite plates. After being polished, the samples were placed into a JEOL JSM-5800LV Scanning Electron Microscope. The samples with the Al particles were observed at 350X magnification whereas the silver samples were observed at 1000X magnification. The samples were scanned using backscatter electron detection in a low vacuum. It was important to find an effective accelerating voltage for the electron beam since too strong a beam would penetrate the sample surface and produce larger visible areas of particles. SEM images of regions with the Al and Ag particles were acquired using the LPi hardware and LPi "SEM ImageScan 4.0" software plug-in in conjunction with NIH Image v1.62 software. The images were then investigated and particle rich regions were cut out and saved. To produce these cutouts, a border was set inside a certain particle rich region in a manner regardless of individual particle location and the location of small areas of particle deficiency within the particle rich region. The region inside this border was then cut out using the software's "cut selection" feature. These cutouts were then measured in terms of pixels to obtain an area measurement. Next, the particles in each cutout image were analyzed using the "Analyze Particles" feature in the NIH Image software and a "Density slice" feature, giving us the area in pixels of each particle. The area of all the particles

was found and divided by the total area of the cutout and multiplied by 100%. This provided the area fraction of the particles, assumed to be equal to the volume fraction of particles in a particle rich region, with respect to the total area of the particle rich region.

As examples, the Al particle rich areas are shown in Figures 2a, b and c whereas the areas with the Ag particles are presented in Figures 3a, b and c. The most important observation was that the particles were not uniformly distributed across the specimens in the regions between the first and second plies. This statement applies to the specimens with the Al and Ag particles. The particles formed large groups in the interlaminar regions of the specimens between the unidirectional plies (see Figures 2a,b and 3a,b). Significant numbers of the particles were also found in the intralaminar regions in the polyimide matrix between the fibers (see Figures 2c and 3c). In the case of the Al samples, the particles were randomly distributed in the interlaminar and intralaminar regions without forming noticeable amounts of particle clusters. However, in the Ag samples the particles formed larger clusters which appeared to be randomly distributed. Very few particles were noticed to be present in the composite specimens outside the clusters.

The volume fractions of the Al and Ag particles obtained from the SEM measurements are listed in Tables 3 and 4, respectively. The total average volume fraction of the Al inclusions based on 24 measurements (24 particle rich interlaminar and intralaminar regions) was found to be 40% with the total standard deviation of 7%. For the specimens with the Ag particles the total average volume fraction was 27% with the standard deviation of 4.9%. Eighteen particle rich regions were selected in the three different Ag specimens.

The shapes of the Al and Ag particles were also carefully analyzed. Samples of Al and Ag powders were taken and analyzed using the SEM. The particle size was also measured on the cross sections of the composite specimens. It was found that the Al particles were ellipsoidal in nature (see Figure 4a) with the average major to minor axes ratio about 1.45, ranging from 1.0 to 6.8 whereas the average diameter of the Al

inclusions was 1.95 μm ranging from 0.41 μm to 33.41 μm . Since the Ag particles always formed particle clusters (see Figure 4b) the average size of the particle could not be measured. Instead, the average size of the Ag clusters was measured and was found to be 6.74 μm ranging from 1.76 μm to 22.19 μm . The distributions of the average size of the Al particles and the Ag clusters are illustrated in Figures 5a and 5b.

It is clear from the data presented above that the distributions of the Al inclusions and Ag clusters cannot be treated either as interlaminar or intralaminar in nature. It appears that the global distributions of the Al and Ag particles are somewhat mixed with the ratios of the interlaminar to intralaminar distributions changing from place to place. The dominant number of the particles however were distributed in the interlaminar regions of the composite specimens. In addition, the Ag inclusions cannot be assumed to be individually and randomly spaced since they always form large clusters consisting of several inclusions with the overall shapes of the clusters being highly irregular. As far as the Al particles are concerned, their shape appears to be highly ellipsoidal with their aspect ratios close to one. In addition, their distribution appears to be random with very few interactions between the inclusions. Both the distributions of the particles in the composite specimens and their overall geometries should have a profound effect on the X-ray data from the XRD measurements.

2.3 X-Ray Diffraction Measurements

The intent of the experiment was to measure the state of strain inside the particles using XRD. The concentration of the particles must be high enough to yield adequate diffracted intensity, but on the other hand it should minimally affect the state of stress inside the specimen. In the present study, two types of metal powders Al and Ag were used as filler particles, and were placed between first and second plies of 6-ply unidirectional laminates during lay-up. This was done by painting a suspension of the metal powder in acetone onto the lamina then after drying placing the second and subsequent plies on top of this layer. The concentrations of metal powders are given in Table 5. These concentrations were selected after preliminary experiments and calculations to provide

sufficient diffracted intensity with a convention sealed-tube diffraction system. The specimens used in the XRD experiments were manufactured at NASA Glenn Reserach Center.

To measure the state of strain inside the particles the procedure described in [15] was used. First, the lattice spacing d_0 of the (4 2 2) planes for unstressed Ag and Al metal particles had to be determined. The free particles were painted in a thin layer onto a quartz plate substrate and placed into a Siemens D500 diffractometer fitted with pseudo parallel-beam optics and a solid state detector. Diffraction conditions are shown in Table 6. Temperature was monitored during each run inside the diffractometer chamber. Lattice spacing d_0 was calculated using Bragg's law:

$$d_0 = \frac{\lambda}{2 \sin \theta_{Bragg}} \quad (1)$$

where θ_{Bragg} is the measured $\kappa\alpha_1$ peak position obtained by fitting a Pseudo-Voigt function to the peak profile. The direction of the incident beam with respect to the specimen's coordinates was determined by two angles: ψ and φ (see Figure 6). Measurements were made at an arbitrary angle $\varphi=0^\circ$ with ψ varying from 0° to 45° in six steps. For each ψ value a slightly different d_0 was obtained (see Tables 7a and 7b). The final d_0 was calculated by correcting the values to a single temperture using the thermal expansion coefficient of the metal, then taking the average of the six measurements performed at different ψ .

From the composite plates 50 mm by 16 mm specimens were cut using a Buehler diamond saw. The top and bottom surfaces were polished lightly with 400 grit paper to reduce surface roughness. Each specimen was mounted on a flat glass plate with silicone rubber and placed into the D-500 specimen holder with glass shims so that the specimen surface was within $\pm .025$ mm of the plane containing the θ rotation axis of the goniometer. The specimen location was checked with a dial gage and micro flat accurate

to .0025 mm. Measurements were made at $\varphi=0^\circ$ and 90° and at six ψ angles from 0° to 45° for each φ angle. The direction $\varphi=0$ was chosen parallel to the fibers. Lattice spacings $d_{\varphi\psi}$ were obtained in the same way as for d_0 . The strain components ε_{ij} ($i,j=1, 2, 3$) in the specimen coordinate system were obtained from:

$$\begin{aligned}\varepsilon_{\varphi\psi} = \frac{d_{\varphi\psi} - d_0}{d_0} &= \varepsilon_{11} \cos^2 \varphi \sin^2 \psi + \varepsilon_{12} \sin 2\varphi \sin^2 \psi + \\ &\quad \varepsilon_{22} \sin^2 \varphi \sin^2 \psi + \varepsilon_{33} \cos^2 \psi + \varepsilon_{13} \cos \varphi \sin 2\psi + \varepsilon_{23} \sin \varphi \sin 2\psi\end{aligned}\tag{2}$$

where the value of d_0 was corrected to the same temperature as that at which the corresponding $d_{\varphi\psi}$ was measured.

Since φ angles of 0° and 90° were used and it was assumed that the fiber direction, the in-plane normal to the fiber direction and the plate normal were the principal axes hence equation (2) was simplified to:

$$\varepsilon_{\varphi=0\psi} = \frac{d_{\varphi=0\psi} - d_0}{d_0} = (\varepsilon_{11} - \varepsilon_{33}) \sin^2 \psi + \varepsilon_{33}\tag{3a}$$

$$\varepsilon_{\varphi=90\psi} = \frac{d_{\varphi=90\psi} - d_0}{d_0} = (\varepsilon_{22} - \varepsilon_{33}) \sin^2 \psi + \varepsilon_{33}\tag{3b}$$

Figures 7.a – d show examples of $\varepsilon_{\varphi\psi}$ vs. $\sin^2 \psi$ plots for unidirectional graphite/polyimide composites containing silver and aluminum inclusions. All $\sin^2 \psi$ plots were linear within experimental error. The normal strain ε_{33} was taken to be an average between $\varepsilon_{\varphi=0\psi=0}$ and $\varepsilon_{\varphi=90\psi=0}$. In order to determine the slope of a straight line on $\varepsilon_{\varphi\psi}$ vs. $\sin^2 \psi$ plot the least squares method was used. ε_{11} and ε_{22} were obtained from the slopes of the $\sin^2 \psi$ plots at $\varphi=0^\circ$ and 90° respectively using least squares linear fits. In order to determine residual stresses in the particles X-ray elastic constants for the 422 reflection were calculated by taking the mean of the Reuss and Voigt models [15, p.70],

using literature values of the single crystal elastic compliances. This procedure gave Young's modulus E and Poisson ratio ν values of $E=71$ GPa, $\nu=0.351$ for aluminum, and $E=85.5$ GPa, $\nu=0.359$ for silver. The stresses were subsequently calculated from the strains assuming isotropic Hooke's law. The values of the slopes, strain, and stress components for each measurement are given in Tables 8a and 8b.

The effect of point to point variation in the strains and stresses was investigated by making XRD measurements on three specimens cut from three different locations on a given plate (designated as -a, -b, and -c in Tables 8a and 8b). Then, three sets of measurements were made on one of these specimens using slightly different irradiated areas (designated as -c, -c, -c). The average values of the stresses and strains in the Al and Ag inclusions for all these measurements are presented in Table 8a and 8b together with their standard deviations. It is evident that the point to point variation in a given specimen is comparable to the specimen to specimen variations. Repeat measurements using the same irradiated area on a given specimen gave much smaller variation: less than $\pm 0.003^{\circ} 2\theta$ in peak position and is related to counting statistics.

3. Thermoviscoelastic Analysis of Residual Stresses in Unidirectional Composite Plates

In general, the state of stress inside metallic particles embedded in the polymer matrix of a polymer matrix composite can be affected by two factors. First, uniform compression is induced by the difference between the thermal expansion coefficients of the particles and the polymer. The magnitude of this compression can be evaluated using the Eshelby approach [16, 17, 18, 19]. Second, during the cooling down phase the actual thermal residual stresses develop in the matrix due to the presence of fibers. These stresses can be determined either using a linear visco-elastic model of the laminated plate (interlaminar model) or using the Eshelby model once again, where the fibers are treated as cylindrical inclusions (intralaminar model). Both the inter and intralaminar solutions were put into Eshelby equations modeling spherical inclusions embedded in a polymer matrix. Calculated in this way, residual stresses inside the particles were compared to stresses

obtained by X-ray diffraction. The reverse comparison can also be performed, namely one can calculate using the Eshelby procedure the residual stresses in the polymer knowing the time and temperature dependent properties of the matrix and inclusions, manufacturing history and average state of stress in the inclusions from XRD measurements. Then, the obtained stresses can be compared to the stresses determined from either the inter- or intralaminar models.

In the numerical analyses of residual stresses either in the inter- or intralaminar models and in the analysis of residual stresses in the Al and Ag particles determined from the application of the visco-elastic Eshelby model it was assumed that the composite was subjected to the cooling cycle specified in the last three steps of the post curing procedure. In the analyses the composite specimens were cooled down from 315^0C to 204^0C over a period of 50 minutes and then immediately cooled down to room temperature over 180 minutes.

By making these assumptions it was stipulated that there were no residual stresses in the composite and in the embedded particles after 600 minutes at 315^0C of the post-curing process. Actually, the entire cycle (including manufacturing and post-curing) could have been modeled using the procedures described in the sections below. However, due to the lack of experimental data on the physical properties of the polyimide resin, the non post cure shear modulus and thermal expansion coefficient, the full analysis of the residual stresses was not done.

3.1. Fiber and matrix properties

The PMR-15 matrix in the unidirectional composite was modeled as a visco-elastic material with its thermal expansion coefficient α depending upon temperature and its shear modulus G depending on both time and temperature. The Poisson ratio of the resin was assumed to be constant. The experimental values of the shear modulus G as a function of time and temperature were taken from [20] and the thermal expansion coefficient of the post cured in air polyimide were provided by the NASA Glenn

Research Center. The values of G and α were subsequently curve fitted to obtain $G(t, T)$ and $a(T)$ functions. These relations are shown in Table 9. In Table 9, the shear modulus is given as a function of time at $T_{ref}=288C$ (the master curve). The vertical, $a_v(T)$, and horizontal, $a_h(T)$, shift functions were estimated from the data presented in Ref. [20] and are also listed in Table 9. The horizontal shift function is used in the definition of reduced time $\xi(t)$ (see equation 4).

$$\xi(t) = \int_0^t \frac{dt'}{a_h[T(t')]} \quad (4)$$

The application of the horizontal and vertical shift functions allows the determination of the $G(t, T)$ function from the master curve. However, this is only valid for a temperature range from room temperature to $348^0 C$ and a range of time from 0 to $10^{6.5}$ sec.

The following properties of the graphite fibers were used in the modeling part of this study:

Thermal expansion coefficients of the fibers:

$$\alpha_{Lf} = -0.5 \cdot 10^{-6} K^{-1} \text{ (longitudinal)}, \alpha_{Tf} = 10 \cdot 10^{-6} K^{-1} \text{ (transverse)},$$

Elastic properties of the fibers:

$$E_{Lf} = 241 \text{ GPa (longitudinal Young's modulus)}, E_{Tf} = 20 \text{ GPa (transverse Young's modulus)}, K_f = 20 \text{ GPa (bulk modulus)}, \nu_{Lf} = 0.2 \text{ (longitudinal Poisson ratio)}, \nu_{Tf} = 0.4 \text{ (transverse Poisson ratio)}, G_{Lf} = 27 \text{ GPa (longitudinal shear modulus)}, G_{Tf} = 11 \text{ GPa (transverse shear modulus)}.$$

3.2 Interlaminar model of residual thermal stresses

Classical lamination theory was used to predict the visco-elastic response of a laminated composite plate consisting of an isotropic polymer layer between two unidirectional orthotropic plies (see Figure 8) during cooling from $315^0 C$ to $30^0 C$. The thickness of the

orthotropic layers was 375 μm and the thickness of the polymer layer was taken as 250 μm . The geometry of the assumed laminate model was equivalent to the unidirectional composite plates used in the XRD measurements consisting of six unidirectional 125 μm thick plies and five 50 μm thick polymer layers. These geometrical properties were found to be most representative based on the SEM investigation.

The performed numerical procedure employs constant time increments and computes the resultant residual stresses after each time interval [9]. For unidirectional composite plies the elastic properties can be determined from the Hashin equations [21] for each time interval if the stiffness properties of the fibers and matrix as well as the volume fraction of the fibers are known and then the value of the time dependent stiffness matrix Q_k for k^{th} ply can be obtained. The thermal expansion coefficients of unidirectional composites in both fiber and transverse directions can also be calculated using Hashin's model as a function of temperature. Since the stiffness properties and thermal expansion coefficients of unidirectional composites do not strongly depend upon time and temperature they were assumed to be constant in this analysis. In addition, the Poisson ratio ν_{12} was also assumed to be independent of time and temperature. However, the transverse stiffness properties were assumed to be temperature and time dependent and the transverse thermal expansion coefficient of the composite was assumed to be only dependent on temperature.

The resultant forces $N^T(t_f)$ in the composite can be calculated as a function of time and temperature from equations 5a and 5b and the residual strains and stresses in the polymer ply can be determined from equations 5c and 5d [9].

$$N^T(t_f) = \sum_{j=0}^{f-1} \sum_{k=1}^n (a_v^k(j) Q_k (\xi(f) - \xi(j)) \cdot \int_{Temp(j)}^{Temp(j+1)} \alpha(T) dT \cdot (z(k) - z(k+1))) \quad (5a)$$

$$N^T(t_f) = \sum_{j=0}^{f-1} \sum_{k=1}^n (a_v^k(j) Q_k (\xi(f) - \xi(j)) \cdot (\varepsilon(j+1) - \varepsilon(j)) \cdot (z(k) - z(k+1))) \quad (5b)$$

$$\varepsilon_{res}(t_f) = \varepsilon(t_f) - \sum_{j=0}^{f-1} \int_{Temp(j)}^{Temp(j+1)} \alpha(T) dT \quad (5c)$$

$$\sigma_{res}(t_f) = \sum_{j=0}^{f-1} (a_v^{polymer}(t) Q_{polymer}(\xi(f) - \xi(j)) \cdot (\varepsilon_{res}(j+1) - \varepsilon_{res}(j))) \quad (5d)$$

where z is the coordinate through the thickness and $\varepsilon(t)$ is the midplane strain.

Comparing equations (5a) and (5b) for $f=1$, where f is the time step number, one can calculate $\varepsilon(t_{f=1})$ provided that $\varepsilon(t_{f=0})=0$. Putting $\varepsilon(t_{f=1})$ into equations (5c) and (5d) the residual strains and stresses can be determined in the polymer layer after the first time step. Repeating this procedure, residual stresses and strains can be calculated for different time steps if $\varepsilon(t_f)$ from previous time steps are determined. It should be pointed out that for the composite $a_v(t)$ was assumed to be 1. The results from the performed computations of the residual stresses in the visco-elastic interlaminar model are presented in section 6.

3.3 Intralaminar model of residual thermal stresses

Since a significant number of Al and Ag inclusions were found to be widely distributed between the fibers in the first and second unidirectional plies it was not clear if the interlaminar calculations of residual stresses performed in the previous section could be compared to the residual stresses in the composite determined through the X-ray measurements. Therefore, an intralaminar model of the composite was also considered. The Eshelby model and its modified version for multiple inclusions [17, 18] were used to calculate residual stresses in the polyimide matrix between the graphite fibers under time and temperature dependent conditions. The model assumes that the matrix is a visco-elastic continuum, while the properties of the graphite fibers are purely linear elastic. The matrix was assumed to be isotropic while fibers were modeled as transversely isotropic bodies. The residual stresses and strains in the polyimide matrix can be determined from equations 6a - 6c:

$$\sum_{i=0}^{f-1} C_I \left(S\epsilon^T(i) + \epsilon^{Res}(i) - \epsilon^T(i) \right) = \sum_{i=0}^{f-1} C_M (\xi(f) - \xi(i)) \left(S\epsilon^T(i) + \epsilon^{Res}(i) - \epsilon^T(i) \right) \quad (6a)$$

$$\epsilon^{Res}(j) + V_f \left(S\epsilon^T(j) - \epsilon^T(j) \right) = 0, \text{ for } j=0, 1, 2, \dots, f \quad (6b)$$

$$\sigma_{polymer}(f) = \sum_{i=0}^{f-1} [C_M (\xi(f) - \xi(i)) \epsilon^{Res}(i)] \quad (6c)$$

where S is the Eshelby tensor for cylindrical inclusions, C_I is the tensor of the elastic properties of the fibers, C_M is the time and temperature dependent tensor of the elastic properties of the matrix, ϵ^T is the stress free transformation strain, ϵ^{Res} is the average residual strain in the matrix generated by the fibers, ϵ^{T*} is the stress free transformation strain of the inhomogeneous inclusion, and V_f is the volume fraction of the fibers. Similar to the interlaminar analysis described in section 3.2 the residual strains and stress in the polymer can be calculated for any time step provided that the strains $\epsilon^R(i)$ and $\epsilon^T(i)$ for the previous time steps are determined. The volume fraction of fibers was taken as 53% that agreed with the acid digestion test results (see Table 1).

The results of the residual stresses from the visco-elastic intralaminar computations are shown in Tables 10-12 in section 6 and compared with the residual stress from the interlaminar model.

4. Visco-Elastic Analysis of Residual Stresses in Embedded Al and Ag Particles

There are two types of residual stresses in the Al and Ag particles embedded in the composite, namely the close and long range stresses. The close range residual stresses are caused by the differences in the elastic properties and thermal expansion coefficients between the inclusions and the matrix and are dependent on the volume fraction of inclusions. The long range stresses in the particles are caused by the global residual stresses in the composite. Both types of stresses can be calculated using the visco-elastic

Eshelby method for multiple inclusions provided that the inclusions are ellipsoidal in nature. The total residual stress in the particles is a superposition of the close and long range stresses. The stresses in the particles determined by XRD measurements are the total stresses. Therefore, in order to predict the residual X-ray stresses in the particles the total stresses must be determined from the Eshelby method.

The total residual stresses in the particles can be calculated from equations 7a-7c:

$$\sum_{i=0}^{f-1} C_I \left(S(\varepsilon^T(i) + \varepsilon^R(i) + \varepsilon^{Res}(i+1) - \varepsilon^{Res}(i) - \varepsilon^{T*}(i)) \right. \\ \left. + \sum_{i=0}^{f-1} C_M (\xi(f) - \xi(i)) \left(S\varepsilon^T(i) + \varepsilon^R(i) + \varepsilon^{Res}(i+1) - \varepsilon^{Res}(i) - \varepsilon^T(i) \right) \right) \quad (7a)$$

$$\varepsilon^R(j) + V_f \left(S\varepsilon^T(j) - \varepsilon^T(j) \right) = 0, \text{ for } j=0, 1, 2, \dots, f \quad (7b)$$

$$\sigma_{particle}(f) = \sum_{i=0}^{f-1} C_I \left(S(\varepsilon^T(i) + \varepsilon^R(i) + \varepsilon^{Res}(i+1) - \varepsilon^{Res}(i) - \varepsilon^{T*}(i)) \right) \quad (7c)$$

where ε^{Res} is the residual strain in the polymer which can be determined either from the interlaminar or intralaminar plate solutions and ε^R is an average strain caused by the presence of multiple inclusions. The other symbols are the same as in equations 6. The numerical procedure is essentially the same as in the intralaminar residual stresses analysis in the composite. Equations 7a-7c can also be used to calculate the close range stresses in the particles if ε^{Res} is assumed to be zero. The long range stresses can also be determined from these equations if only ε^{T*} is zero. The total and close range residual stresses in the Al and Ag particles are shown in Tables 10-12 in section 6.

5. Determination of the Residual Stresses in the Composite from the X-ray Stresses

There were two goals of this research. The first goal was to measure residual stresses in the Al and Ag particles embedded in the unidirectional graphite/polyimide composite and subsequently to compare them with their numerical predictions. The second goal, which was even more important than the first one, was to determine the residual stresses in the polyimide matrix from the XRD measurements and compare them with the residual stress analysis of the composite from both the inter- and intralaminar models.

The residual strains and stresses in the composite can be calculated if the residual strains and stresses in the particles are known, for example from the X-ray measurements, following the schematic depicted in Figure 9. In this case, the residual strain ϵ^{Res} is unknown and can be determined if $\epsilon^{\text{X-Ray}}$ (the X-ray strains in the particles) and ϵ^{CR} (the close range strains in the particles) are known. This problem can be easily solved if the linear elastic Eshelby model for multiple inclusions is applied. The problem is linear elastic and does not require tedious visco-elastic computations provided that the close range strains are determined through the application of the visco-elastic Eshelby method.

The calculations of the residual strains and stresses in the composite were performed assuming room temperature elastic properties and thermal expansion coefficients of the polymer matrix and using the previously established close range-strains in the particles and the X-ray strains. The residual stresses in the composite were subsequently compared to the residual stresses from the intralaminar and interlaminar visco-elastic computations. The stress results from this analysis are presented in the section below.

6. Numerical Results of Residual Stresses Calculations

The numerical results of residual thermal stresses in the unidirectional graphite/polyimide composite calculated with the interlaminar and intralaminar assumptions as well as the predicted total residual thermal stresses in the Al and Ag particles (*) and the close range stresses (**) are shown in Tables 10 and 11 and Figures 10 a,b and c. In addition, the

residual stresses in the composite determined from the X-ray diffraction experiments in conjunction with the application of the Eshelby method for multiple inclusions are also shown in these two tables (indicated by ***). The results presented in Table 10 were obtained under visco-elastic conditions as a function of the number of time steps. The number of the time steps ranged from 6 to 48 with the time steps ranging from 1800 seconds to 225 seconds. The results for the Ag particles in Table 11 were only shown for 24 time steps since the relations between the number of time steps and the calculated stresses were very similar to the results presented in Table 10 for the Al inclusions. The stresses in the inclusions (total (*) and close range (**) stresses) and the stresses in the composite (****) were determined assuming the average volume fractions of inclusions to be 40% for the Al inclusions and 29% for the Ag inclusions, as established from the SEM analyses (see Tables 3 and 4). The data listed in Tables 12a and 12b for the Al and Ag particles were obtained under purely linear elastic conditions.

The effect of volume fractions of inclusions on the predicted residual stresses in the Al and Ag inclusions were also examined. These results are shown in Figures 11a,b and 12a,b for both the interlaminar and intralaminar models with 24 time steps. The residual stresses in the particles determined from the X-ray diffraction tests are indicated in these figures for comparison. It can be clearly seen that the predicted residual stresses in the particles depend strongly on the number of particles.

6. Discussion

If the data presented in Tables 8b and 10 are examined it can be clearly seen that the measured and predicted residual stresses (σ_{11} and σ_{22} stress components) in the Al inclusions are very close to each other with the exception of σ_{33} if the interlaminar model is used. In the case of the intralaminar model only the σ_{11} stress component agrees with the experimental data. The average σ_{11} and σ_{22} stress components from the X-ray analysis are 50 MPa and 29 MPa, respectively whereas the stress components from the visco-elastic interlaminar analysis with 48 time steps are 49.4 MPa and 25.4 MPa, respectively. The σ_{11} components from the inter and intralaminar models are very similar

however the σ_{22} components are entirely different. Therefore, the numerical residual stresses in the Al inclusions from the interlaminar model appear to be much closer to the experimental data than the predicted stresses in the inclusions from the intralaminar model. The σ_{33} components are discussed later.

The results from the visco-elastic analysis of the interlaminar and intralaminar residual stresses in the polymer and the close range stresses in the Al particles performed as a function of the number of time steps presented in Table 10 and Figures 10(a-c) clearly indicate that the stress results almost stabilize around 48 steps. The error in the stress calculations between the analyses performed with 24 and 48 time steps is less than 1%. Therefore, it is not necessary to increase the number of time steps to more than 48 in order to improve the accuracy of the visco-elastic computations of the residual stresses in the particles and the composite.

The visco-elastic Eshelby method for multiple inclusions was used in this research to determine the close-range stresses in the inclusions caused by the differences in the thermal expansion coefficients and elastic properties between the matrix and multiple inclusions. Then, the close-range stresses were used to determine the stresses in the composite using the residual X-ray stresses. The visco-elastic Eshelby method was also used in this research to calculate the intralaminar thermal stresses in the composite plates. Since considerable volume fractions of inclusions and fibers were considered it was unclear if such large densities of inclusions can be accurately modeled using the Eshelby method. It has been shown by Hsueh and Becher [22] that the linear elastic Eshelby method can be successfully applied for multiple inclusion cases if the volume fraction of is less than 30%. Up to this value excellent agreements between the residual stresses in ellipsoidal inclusions determined from finite elements and the Eshelby method were obtained. However, even for higher volume fractions (up to 60% of hexagonally distributed fibers) the agreement was also quite good. Therefore, the assumed volume fractions of Al and Ag inclusions (40% and 29%) and graphite fibers (53%) should not have generated significant errors in the stress analysis.

Another important observation which can also be made by evaluating the data listed in Table 10 is that the predicted residual stresses in the composite from the interlaminar model are also very close to the estimated residual stresses in the composite from the X-ray tests and the Eshelby model, with the exception of the through-the-thickness stress σ_{33} . However, contrary to the plane stress conditions obtained from the interlaminar model the residual stresses in the composite estimated from the X-ray stresses in the Al particles are triaxial.

It can also be seen in the data presented in Table 10 and 12a that the linear elastic assumptions in the analysis of the residual stresses in the polymer of the composite are incorrect. The linear elastic model grossly overestimates the stresses in comparison with the visco-elastic conditions. However, the residual stresses in the composite (****) determined from the X-ray stresses in the Al inclusions and the linear elastic Eshelby model for multiple inclusions (see Table 12a) are not significantly different in comparison with the stresses from the X-ray analysis and the visco-elastic Eshelby model (see Table 10). The linear elastic Eshelby model of multiple inclusions overestimates the σ_{11} , σ_{22} and σ_{33} stress components (****) in the composite by approximately 10%, 11% and 20%, respectively in comparison with the visco-elastic model.

The numerical residual stress results in the Al inclusions and the residual stresses in the polyimide matrix obtained from the numerical close range stresses and the X-ray stresses were determined for the average volume fraction of Al inclusions (40%) and the average stresses from the XRD measurements. However, noticeable scatter in the X-ray data (see Table 8b) and the volume fraction of the particles (see Table 3) were observed. To evaluate the effect of the scatter in the Al distribution and the resulting scatter in the X-ray data, the residual stresses in the composite were additionally computed considering both types of scatter and assuming the interlaminar model. By doing this, the lower and upper ranges of the residual stresses in the composite determined from the X-ray data and the visco-elastic Eshelby model of multiple inclusions were established. This set of data is presented in Table 13. It can be seen that the highest residual stresses in the composite exist if the upper range in the X-ray data is taken with the lower range of the particle

volume fraction. Under these conditions the residual stresses increase to $\sigma_{11} = 59.6 \text{ MPa}$, $\sigma_{22} = 45.1 \text{ MPa}$ and $\sigma_{33} = 28.8 \text{ MPa}$. If the lower range in the X-ray data is taken in combination with the upper range in the particle volume fraction the estimated residual stresses decrease to $\sigma_{11} = 44.5 \text{ MPa}$, $\sigma_{22} = 29.9 \text{ MPa}$ and $\sigma_{33} = 17.2 \text{ MPa}$. Obviously, there is a strong effect of the particle volume fraction on the estimated residual thermal stresses in the composite. If the particle volume fraction in the composite was constant the scatter in the estimated residual stresses would be much lower. Considering the aforementioned, the average residual stress components in the resin, σ_{11} , σ_{22} and σ_{33} , in the unidirectional graphite/polyimide composite with the embedded Al inclusions are $52.2 \text{ MPa} \pm 14\%$, $37.6 \text{ MPa} \pm 20\%$ and $23 \text{ MPa} \pm 25\%$, respectively. The highest tensile stresses exist in the direction of the fibers and are lower than the tensile strength of the polyimide resin at room temperature (approximately 80 MPa) [23].

This research shows that the residual stresses in inclusions determined from the X-ray strains are noticeably higher for the Ag (see Table 8a) inclusions than for the Al inclusions (see Table 8b). At the same time the residual stresses in the composite calculated from the X-ray stresses in the inclusions using the visco-elastic Eshelby model for multiple inclusions are also significantly higher for the composite with the embedded Ag (see Table 11) inclusions than for the composite samples with the Al inclusions (see Table 10). In addition, the residual stresses in the composite specimens with the Ag inclusions do not agree with the prediction of the stresses in the composite (without inclusions) determined from the visco-elastic classical laminate theory (see Table 11). In order to explain this surprising difference in the residual stress values the effect of inclusion shape on the stresses in the Al and Ag inclusions needs to be investigated. It should be remembered that in order to determine the residual stresses in the composite specimens with Al and Ag inclusions, the inclusions were assumed to be ellipsoidal in nature. This assumption satisfied very well the actual conditions for the Al inclusions which were found to be almost spherical. However, this assumption is certainly not valid for the Ag inclusions. As can be seen in Figure 4b the Ag inclusions are highly irregular forming actually large clusters of inclusions which are also non-spherical. By comparing the overall shapes of the two different types of inclusions (Al and Ag) it is not surprising

that the X-ray stresses are so different in the two cases. The effect of inclusion shape on the internal stresses can be very easily evaluated by performing very simple linear-elastic finite element computations of internal stresses in two Ag inclusions with different shapes (see Figure 13a and b). The first inclusion was assumed to be spherical (see Figure 13a) whereas the other one was slightly irregular (Figure 13b). The elastic properties and thermal expansion coefficients of the matrix and inclusions were assumed to be the same in both cases. The only difference was the inclusion shape. Both systems were cooled down by 285° C. The average internal stresses in the spherical inclusion were found to be approximately 12% lower than the average stresses in the irregular inclusion. In addition, the stress distribution in the irregular inclusion was found to be non-uniform. It can be expected that the difference in the stresses in the spherical and irregular inclusions will increase if the amount of inclusion distortion is increased. Since the observed clusters of Ag inclusions are highly irregular it is not surprising that the obtained X-ray stresses in the Ag inclusions were so much higher than in the Al inclusions. Since the residual stresses in the composite can only be obtained from the X-ray stresses if an inclusion shape is assumed to be ellipsoidal (spherical, oblate, disc, etc.) the application of the highly irregular Ag inclusions in the X-ray experiments creates obvious problems. This type of inclusion cannot be used for the accurate determination of residual stresses in a polymer matrix composite using the X-ray diffraction methodology.

Another important observation made by analyzing the data presented in Table 10 is that the residual stresses in the composite obtained from the X-ray stresses in the Al particles and using the visco-elastic Eshelby model for multiple inclusions are triaxial with significant σ_{33} present. Contrary to the fundamental assumption of laminate theory the state of stress in the interlaminar regions is not plane. There are two potential factors that could contribute to the presence of the significant through-the-thickness stresses. The first factor could be caused by the presence of a significant number of intralaminar inclusions distributed around the intralaminar regions in the composite (see Figure 2c). The intralaminar inclusions could pick up some positive transverse stresses as shown in Table 10 for the intralaminar residual stress model. The other factor could be related to the non-uniform thickness of the matrix containing the particles between the plies, which was

frequently observed in the composite specimens tested. If the thickness of the matrix in the interlaminar model is constant (see Figure 14a) the residual stresses in the composite are biaxial and plane stress. However, if the thickness of the matrix between the plies is not constant (see Figure 14b) the residual interlaminar stresses are not biaxial but triaxial. This can also be shown by performing simple finite element computations of residual interlaminar thermal stresses in a composite structure with a non-uniform thickness distribution.

In this research, the effect of a non-uniform thickness distribution was examined by modeling the composite plies as homogenous orthotropic bodies on both sides of an isotropic resin and assuming different elastic properties and thermal expansion coefficients for the plies and the matrix. It was found that if thickness is not constant, following the conditions shown in Figure 14b, significant σ_{33} appeared with σ_{22} and σ_{11} slightly increasing in the middle of the model. It is stipulated that the second factor is the dominant with the first factor (intralaminar inclusion effect) being secondary since the overall distributions of the residual stresses in the unidirectional composite are closer to the interlaminar model than to the intralaminar assumption.

Considering all the experimental and numerical results presented in this study it is clear that only ellipsoidal inclusions can be successfully used to evaluate the residual stresses in the composite using the proposed methodology (for example the spherical Al inclusions used in this research). Since the Ag particles are not ellipsoidal in nature they concentrate much higher residual stresses than the spherical Al inclusions. The Ag inclusions are highly irregular therefore the Eshelby model cannot be used to evaluate the close range stresses and thus the stresses in the composite from the X-ray stresses. If irregular particles are used another approach is needed in the stress evaluation.

The proposed methodology for the determination of residual stresses based on the concept of embedded crystalline inclusions can be used not only for unidirectional but also for cross ply laminates. Inclusions with various shapes can also be used providing that they satisfy the Eshelby assumptions.

6. Conclusions

A new methodology of the evaluation of residual thermal stresses in unidirectional polymer matrix composites based on X-ray diffraction measurements of residual stresses in embedded crystalline inclusions in conjunction with the application of the visco-elastic Eshelby method for multiple inclusions was proposed. It was successfully applied to determine residual thermal stresses in a unidirectional graphite/PMR-15 composite. The best agreement between numerically predicted interlaminar thermal stresses and the stresses determined by X-ray and the Eshelby model was obtained when Al inclusions were used. A strong effect of particle shape on the measured X-ray stresses was found. In particular, the highly irregular Ag particles significantly overestimated the residual stresses in the composite if the shape of the particles was assumed to be spherical. Despite the fact that the distribution of the particles was not purely interlaminar the residual stresses in the composite determined from the analysis agreed quite well with the interlaminar assumptions. The accuracy of the method could be significantly increased if the distribution of either interlaminar or intralaminar particles was strictly controlled.

References

1. N. J. Rendler and I. Vigness, Hole-drilling Strain-gage Method of Measuring Residual Stresses, *Experimental Mechanics.*, p. 577-586, 1966
2. H. E. Gascoigne, Residual Surface Stresses in Laminated Cross-ply Fiber-epoxy Composite Materials, *Experimental Mechanics*, vol. 34, p. 27-36, 1994
3. R. Y. Kim, H. T. Hahn, Effect of Curing Stress on the First Ply-failure in Composite Laminates, *Journal of Composite Materials*, vol. 13, p. 2-16, 1979

4. H. Fukuda, K. Takahashi and S. Toda, Thermal deformation of Anti-symmetric Laminates at Cure, *Proc. ICCM-10*, vol. 3, p. 141-148, 1995
5. P. G. Ifju, X. Niu, B. C. Kilday, S. C. Liu and S. M. Ettinger, Residual Stress Measurement in Composite Using the Cure-referencing Method, *Experimental Mechanics*, vol. 40, p. 22-30, 2000
6. G. P. Carman and G. P. Sendeckyj, Review of the Mechanics of Embedded Optical Sensors, *Journal of Composite Technology and Research*, VOL. 17, P. 183-193, 1995
7. G. Jeronimidis and A. T. Parkyn, Residual Stress in Carbon Fiber-Thermoplastic Matrix Laminates, *Journal of Composite Materials*, vol. 22, p. 401- 415, 1988
8. J. N. Reddy, *Mechanics of Laminated Composite Plates. Theory and Analyses.*, CRC Press, 1997
9. T. M. Wang and M. Daniel, Thermoviscoelastic Analysis of Residual Stresses and Warpage in Composite Laminates, *Journal of Composite Materials*, vol. 26, p. 883-899, 1992
10. S. R. White and Y. K. Kim, Process-Induced Residual Stress Analysis of AS4/3501-6 Composite Material, *Mechanics of Composite Materials and Structures.*, vol. 5, p.153, 1998
11. P. Predecki and C. S. Barrett, Stress Measurement in Graphite/Epoxy Composites by X-ray Diffraction from Fillers, *J. Comp. Mat.*, vol. 13, p. 61, 1979
12. P. Predecki, C. S. Barrett, Residual Stresses in Resin Matrix Composites, In E. Kula, editor, *28th Sagamore Army Materials Research Conference*, p. 409-424, Lake Placid, July 13-17 1981

13. C. S. Barrett and P. Predecki, Stress Measurements in Graphite/Epoxy Uniaxial Composites by X-rays, *Polymer Composites*, vol. 1, p. 2-6, 1980
14. D. Dragoi, Residual Stress Analysis of Graphite/Polyimide Composites Using the Concept of Metallic Inclusions, Ph.D. thesis, Faculty of Natural Science, Mathematics and Engineering, University of Denver, USA, 1999
15. I. C. Noyan and J. B. Cohen, Residual Stress. Measurement by Diffraction and Interpretation. Springer-Verlag, New York, 1987
16. J. D. Eshelby, The Determination of the Elastic Field of an Ellipsoidal inclusion, and Related Problems, *Proc. R. Soc. London*, vol. A241, p. 376, 1957
17. T. Mura, *Micromechanics of Defects in Solids*, 2nd edition, Martinus Nijhoff Publishers, Dordrecht, 1987
18. T. Mori and K. Tanaka, Average Stress in Matrix and Average Elastic Energy of Materials with Misfitting Inclusions, *Acta Metall.*, vol. 21, p. 571, 1973
19. D. Hull and T. W. Clyne, *An Introduction to Composite Materials*, 2nd edition, Cambridge University Press, 1996
20. G. D. Roberts, D. C. Malarik and J. O. Robaidek Viscoelastic Properties of Addition-Cured Polyimides Used in High Temperature Polymer Matrix Composites, Composites Design, Manufacturing, and Applications; *Proceedings of the Eight International Conference on Composite Materials*, S. W. Tsai and G. S. Springer, Eds., Society for Advanced Materials and Process Engineering, Covina, CA 1991, p. 12-H-1 to 12-H-10
21. Z. Hashin, Analysis of Properties of Fiber Composites with Anisotropic Constituents, *Journal of Applied Mechanics*, vol. 46, p. 543, 1979

22. C. H. Hsueh and P. F. Becher, Residual Thermal Stresses in Ceramic Composites.
Part I: with Ellipsoidal Inclusions. *Materials Science and Engineering*, vol. A212, p.
22, 1996
23. S. A. Swan, Effects of Aging on High Temperature Fracture of Polyimide Polymers,
Ph.D. Thesis, University of Houston, December 1997

Captions

Tables

Table 1. Acid digestion results for plates A (with Al inclusions), B (with Ag inclusions) and C (without inclusions).

Table 2. Glass transition and decomposition temperatures for plates A, B and C.

Table 3. Distributions of Al particles in three specimens (volume fractions).

Table 4. Distributions of Ag particles in three specimens (volume fractions).

Table 5. Nominal particle concentrations.

Table 6. Diffraction conditions.

Table 7. Lattice spacing d_0 for different angles ψ for : (a) Ag powder and (b) Al powder.

Table 8. Strains and stresses inside Ag (a) and Al (b) inclusions and $\varepsilon_{\varphi\psi}$ vs. $\sin^2\psi$ slopes from the X-ray diffraction measurements.

Table 9. Visco-elastic properties of PMR-15.

Table 10. Residual stresses in the composite (in the polymer) from the interlaminar and intralaminar models, the total predicted (*) and close range (**) stresses in the Al particles and the stresses in the composite (***) from the X-ray stresses and the Eshelby model as a function of the number of time steps N (visco-elastic analysis).

Table 11. Residual stresses in the composite (in the polymer) from the interlaminar and intralaminar models, the total predicted (*) and close range (**) stresses in the Ag particles and the stresses in the composite (***) from the X-ray stresses and the Eshelby model for 24 time steps (visco-elastic analysis).

Table 12. Residual stresses in the composite from the interlaminar and intralaminar models, the total predicted (*) and close range (**) stresses in the Al (a) and Ag (b) particles and the stresses in the composite (***) from the X-ray stresses (linear elastic analysis).

Table 13. Residual stresses in the composite determined from the X-ray stresses in the Al inclusions and the Eshelby method for 24 time steps. The scatters in the X-ray data and the volume fraction of inclusions were considered.

Figures

Figure 1. A schematic of the composite models: (a) interlaminar model and (b) intralaminar model.

Figure 2. Al inclusions between the first and second ply: (a) predominantly interlaminar inclusions (along the fibers), (b) mixture of interlaminar and intralaminar inclusions (along the fibers), and (c) mixture of interlaminar and intralaminar inclusions (perpendicular to the fibers).

Figure 3. Ag inclusions between the first and second ply: (a) predominantly interlaminar inclusions (along the fibers), (b) mixture of interlaminar and intralaminar inclusions

(along the fibers), and (c) mixture of interlaminar and intralaminar inclusions (perpendicular to the fibers).

Figure 4. Examples of Al and Ag inclusions: (a) Al inclusion and (b) Ag cluster.

Figure 5. Distributions of inclusion sizes: (a) Al inclusions and (b) Ag inclusions.

Figure 6. The definition of angles φ and ψ , and the specimen coordinates x_1, x_2, x_3

Figure 7 Examples of plots of $\varepsilon_{\varphi\psi}$ as a function of $\sin^2\psi$: (a) and (b) for a specimen with Al inclusions and (c) and (d) for a specimen with Ag inclusions.

Figure 8 Composite model for the interlaminar analysis.

Figure 9. Model used for the determination of residual strains and stresses in the matrix from the X-ray strains and the close range strains.

Figure 10. Visco-elastic interlaminar (a) and intralaminar (b) residual stresses in the composite (in the matrix) and the close range stresses for the Al particles (c) as a function of the number of time steps. Linear elastic solutions are also shown for comparison.

Figure 11. Residual stresses in Al particles: (a) from the interlaminar model and (b) from the intralaminar model as a function of the volume fraction of inclusions. The ranges of the residual X-ray stresses in the particles are also indicated for comparison.

Figure 12. Residual stresses in Ag particles: (a) from the interlaminar model and (b) from the intralaminar model as a function of the volume fraction of inclusions. The ranges of the residual X-ray stresses in the particles are also indicated for comparison.

Figure 13. Finite element analysis of spherical and distorted Ag particles.

Figure 14. Interlaminar models with constant (a) and varying (b) thickness of the polymer layer.

Acknowledgments

This research has been supported by the Air Force Office of Scientific Research and NASA Glenn Research Center under grants F49620-97-1-0426 (AFOSR) and F49620-00-1-0159 (AFOSR and NASA).

Table 1.

	Resin, wt %	Fiber, vol. %	Void Content, vol. %
Plate A (Al)	39.53	53.81	-1.23*
Plate B (Ag)	40.82	53.04	-2.33*
Plate C (Ref)	39.77	52.56	0.64

Table 2.

	T _g (°C) by TMA	T _d (°C) by TGA in air
Plate A (Al)	344	461
Plate B (Ag)	340	489
Plate C (Ref)	338	497

Table 3.

Location	Specimen #1	Specimen #2	Specimen #3	Total	Std. Dev.
1	40.1	43.8	33.1		
2	38.0	48.9	33.2		
3	43.4	44.4	38.1		
4	23.0	52.1	30.6		
5	48.2	40.0	34.2		
6	52.3	40.6	35.0		
7	45.6	44.7	37.5		
8	36.7		34.1		
9	41.6				
Average	41.0	44.9	34.5	40.0	7.0

Table 4.

Location	Specimen #1	Specimen #2	Specimen #3	Total Average	Std. Dev.
1	25.0	26.0	22.6		
2	23.8	25.2	21.8		
3	30.2	25.0	23.6		
4	28.4	25.0			
5	30.8	25.9			
6	21.5	35.3			
7	22.3	36.5			
8		36.1			
Average	26.0	29.4	22.7	27.0	4.9

Table 5.

Specimen Name	Filler Type	Nominal Particle Concentration (mass/area) [mg/cm ²]
Al-U2	Aluminum	4.6
Ag-U2	Silver	5.6

Table 6.

Radiation	Cu K α_1 , $\lambda=1.5406$ Å
Reflection	422
2 θ Range (deg)	136-139.5 (Al), 133.5-137 (Ag)
Step Size (deg)	.02
Step Time (sec)*	10 (for $\psi < 34$), 5 (for $\psi > 34$)
Divergence Slit (deg)	0.1
Soller Slit (deg)	0.15
Detector Energy, Window	8.04 keV, 340 eV

* step times were chosen to give peak to background ratios greater than 3:1

Table 7a.

$\text{Sin}^2\psi$	d_0 [Å]	Temperature [C]
0	0.83418	31
0.1	0.834193	30.5
0.2	0.834193	30
0.3	0.834199	30
0.4	0.834205	29.5
0.5	0.834226	29

Table 7b.

$\sin^2 \psi$	d_0 [A]	Temperature [C]
0	0.826731	32
0.1	0.826742	32
-0.2	0.826723	32
0.3	0.826748	32
0.4	0.826725	32
0.5	0.826737	32

Table 8a.

Specimen's Type	Slope $\varphi=0$ [10^{-6}]	Slope $\varphi=90$ [10^{-6}]	ε_{11} (4 2 2) [10^{-6}]	ε_{22} (4 2 2) [10^{-6}]	ε_{33} (4 2 2) [10^{-6}]	σ_{11} [MPa]	σ_{22} [MPa]	σ_{33} [MPa]
Ag2U-a	869	493	582	206	-287	77	53	22
Ag2U-b	825	327	525	27	-300	53	22	1.3
Ag2U-c	800	283	512	-5	-288	50	17	-0.6
Ag2U-c	800	150	576	-74	-224	58	18	8
Ag2U-c	880	220	642	-18	-238	71	30	16
Average	835	295	567	27	-267	62	28	9
Standard deviation	38	129	52	106	34	12	15	10

Table 8b.

Specimen's Type	Slope $\varphi=0$ [10^{-6}]	Slope $\varphi=90$ [10^{-6}]	ε_{11} (4 2 2) [10^{-6}]	ε_{22} (4 2 2) [10^{-6}]	ε_{33} (4 2 2) [10^{-6}]	σ_{11} [MPa]	σ_{22} [MPa]	σ_{33} [MPa]
Al2U-a	830	272	565	7	-265	49	19	5
Al2U-b	956	438	634	116	-322	60	33	9.5
Al2U-c	640	480	367	207	-273	38	29	4
Al2U-c	780	490	514	224	-266	56	41	15
Al2U-c	730	340	483	93	-247	46	25	7
Average	787	404	513	129	-275	50	29	8
Standard deviation	118	95	99	89	28	9	8	4.4

Table 9.

G at reference temperature ($T_{ref}=288^{\circ} C$) [GPa]	$G = 10^{Exp(0.16(-Log(t)+6.5)^{0.5})+7.5}$
$a_v(T)$ vertical shift function	$a_v = 10^{Exp(0.012(-T+348)^{0.48})-1.076}$
$a_h(T)$ horizontal shift function	$a_h = 10^{Exp(0.41(-T+348)^{0.28})-4.3}$
$\alpha(T)$ thermal expansion coefficient	$\alpha = 3 \cdot 10^{-12} \cdot (104 + T) \\ (127160 - 548 \cdot T + T^2)$

Table 10.

Model	Residual stresses in composite [MPa]	Total stresses in Al inclusions* [MPa]	Close range stresses in Al inclusions** [MPa]	Residual stresses in composite*** [MPa]	N	T_step [sec]
Interlaminar	$\sigma(1,1) = 45.3$ $\sigma(2,2) = 29.9$ $\sigma(3,3) = 0$	$\sigma(1,1) = 46.4$ $\sigma(2,2) = 24$ $\sigma(3,3) = -20.3$	$\sigma(1,1) = -15.1$ $\sigma(2,2) = -15.1$ $\sigma(3,3) = -15.1$	$\sigma(1,1) = 51.5$ $\sigma(2,2) = 36.9$ $\sigma(3,3) = 22.3$	6	1800
Intralaminar	$\sigma(1,1) = 45$ $\sigma(2,2) = 13.7$ $\sigma(3,3) = 13.7$	$\sigma(1,1) = 44.3$ $\sigma(2,2) = -1.3$ $\sigma(3,3) = -1.3$	$\sigma(1,1) = -15.1$ $\sigma(2,2) = -15.1$ $\sigma(3,3) = -15.1$	$\sigma(1,1) = 51.5$ $\sigma(2,2) = 36.9$ $\sigma(3,3) = 22.3$	6	1800
Interlaminar	$\sigma(1,1) = 47$ $\sigma(2,2) = 31$ $\sigma(3,3) = 0$	$\sigma(1,1) = 48$ $\sigma(2,2) = 24.7$ $\sigma(3,3) = -21.2$	$\sigma(1,1) = -15.7$ $\sigma(2,2) = -15.7$ $\sigma(3,3) = -15.7$	$\sigma(1,1) = 52$ $\sigma(2,2) = 37.4$ $\sigma(3,3) = 22.8$	12	900
Intralaminar	$\sigma(1,1) = 46.7$ $\sigma(2,2) = 14.2$ $\sigma(3,3) = 14.2$	$\sigma(1,1) = 46$ $\sigma(2,2) = -1.4$ $\sigma(3,3) = -1.4$	$\sigma(1,1) = -15.7$ $\sigma(2,2) = -15.7$ $\sigma(3,3) = -15.7$	$\sigma(1,1) = 52$ $\sigma(2,2) = 37.4$ $\sigma(3,3) = 22.8$	12	900
Interlaminar	$\sigma(1,1) = 47.9$ $\sigma(2,2) = 31.6$ $\sigma(3,3) = 0$	$\sigma(1,1) = 48.5$ $\sigma(2,2) = 25.1$ $\sigma(3,3) = -21.6$	$\sigma(1,1) = -16$ $\sigma(2,2) = -16$ $\sigma(3,3) = -16$	$\sigma(1,1) = 52.2$ $\sigma(2,2) = 37.6$ $\sigma(3,3) = 23$	24	450
Intralaminar	$\sigma(1,1) = 47.6$ $\sigma(2,2) = 14.5$ $\sigma(3,3) = 14.5$	$\sigma(1,1) = 46.9$ $\sigma(2,2) = -1.4$ $\sigma(3,3) = -1.4$	$\sigma(1,1) = -16$ $\sigma(2,2) = -16$ $\sigma(3,3) = -16$	$\sigma(1,1) = 52.2$ $\sigma(2,2) = 37.6$ $\sigma(3,3) = 23$	24	450
Interlaminar	$\sigma(1,1) = 48.3$ $\sigma(2,2) = 31.9$ $\sigma(3,3) = 0$	$\sigma(1,1) = 49.4$ $\sigma(2,2) = 25.4$ $\sigma(3,3) = -21.8$	$\sigma(1,1) = -16.1$ $\sigma(2,2) = -16.1$ $\sigma(3,3) = -16.1$	$\sigma(1,1) = 52.3$ $\sigma(2,2) = 37.7$ $\sigma(3,3) = 23.1$	48	225
Intralaminar	$\sigma(1,1) = 48.1$ $\sigma(2,2) = 14.6$ $\sigma(3,3) = 14.6$	$\sigma(1,1) = 47.3$ $\sigma(2,2) = -1.4$ $\sigma(3,3) = -1.4$	$\sigma(1,1) = -16.1$ $\sigma(2,2) = -16.1$ $\sigma(3,3) = -16.1$	$\sigma(1,1) = 52.3$ $\sigma(2,2) = 37.7$ $\sigma(3,3) = 23.1$	48	225

Table 11.

Model	Residual stresses in composite	Total stresses in Ag inclusions *	Close range stresses in Ag inclusions**	Residual stresses in composite***	N	T_step [sec]
Interlaminar	$\sigma(1,1) = 47.9$ $\sigma(2,2) = 31.6$ $\sigma(3,3) = 0$	$\sigma(1,1) = 47.2$ $\sigma(2,2) = 21.2$ $\sigma(3,3) = -30$	$\sigma(1,1) = -22$ $\sigma(2,2) = -22$ $\sigma(3,3) = -22$	$\sigma(1,1) = 62.5$ $\sigma(2,2) = 41$ $\sigma(3,3) = 29$	24	450
					24	450
Intralaminar	$\sigma(1,1) = 47.6$ $\sigma(2,2) = 14.5$ $\sigma(3,3) = 14.5$	$\sigma(1,1) = 45.2$ $\sigma(2,2) = -7.7$ $\sigma(3,3) = -7.7$				

Table 12a.

Model	Residual stresses in composite [MPa]	Total stresses in Al inclusions* [MPa]	Close range stresses in Al inclusions** [MPa]	Residual stresses in composite*** [MPa]
Interlaminar	$\sigma(1,1) = 70.4$ $\sigma(2,2) = 44.4$ $\sigma(3,3) = 0$	$\sigma(1,1) = 73.9$ $\sigma(2,2) = 36.5$ $\sigma(3,3) = -28.2$	$\sigma(1,1) = -20.7$ $\sigma(2,2) = -20.7$ $\sigma(3,3) = -20.7$	$\sigma(1,1) = 57$ $\sigma(2,2) = 42$ $\sigma(3,3) = 28$
Intralaminar	$\sigma(1,1) = 70$ $\sigma(2,2) = 20.6$ $\sigma(3,3) = 20.6$	$\sigma(1,1) = 71$ $\sigma(2,2) = -0.1$ $\sigma(3,3) = -0.1$		

Table 12b.

Model	Residual stresses in composite [MPa]	Total stresses in Ag inclusions* [MPa]	Close range stresses in Ag inclusions** [MPa]	Residual stresses in composite*** [MPa]
Interlaminar	$\sigma(1,1) = 70.4$ $\sigma(2,2) = 44.4$ $\sigma(3,3) = 0$	$\sigma(1,1) = 71.5$ $\sigma(2,2) = 30.6$ $\sigma(3,3) = -40.3$	$\sigma(1,1) = -29.5$ $\sigma(2,2) = -29.5$ $\sigma(3,3) = -29.5$	$\sigma(1,1) = 69$ $\sigma(2,2) = 47$ $\sigma(3,3) = 35$
Intralaminar	$\sigma(1,1) = 70$ $\sigma(2,2) = 20.6$ $\sigma(3,3) = 20.6$	$\sigma(1,1) = 68.5$ $\sigma(2,2) = -9.3$ $\sigma(3,3) = -9.3$		

Table 13.

	X-ray av. and V_I frac. av. [MPa]	X-ray min. and V_I frac. min. [MPa]	X-ray max. and V_I frac. max. [MPa]	X-ray min. and V_I frac. max. [MPa]	X-ray max. and V_I frac. min. [MPa]
$\sigma(1,1)$ [MPa]	52.2	45.4	59.4	44.5	59.6
$\sigma(2,2)$ [MPa]	37.6	32.3	43.4	29.9	45.1
$\sigma(3,3)$ [MPa]	23	20.7	25.4	17.2	28.8

Interlaminar Model

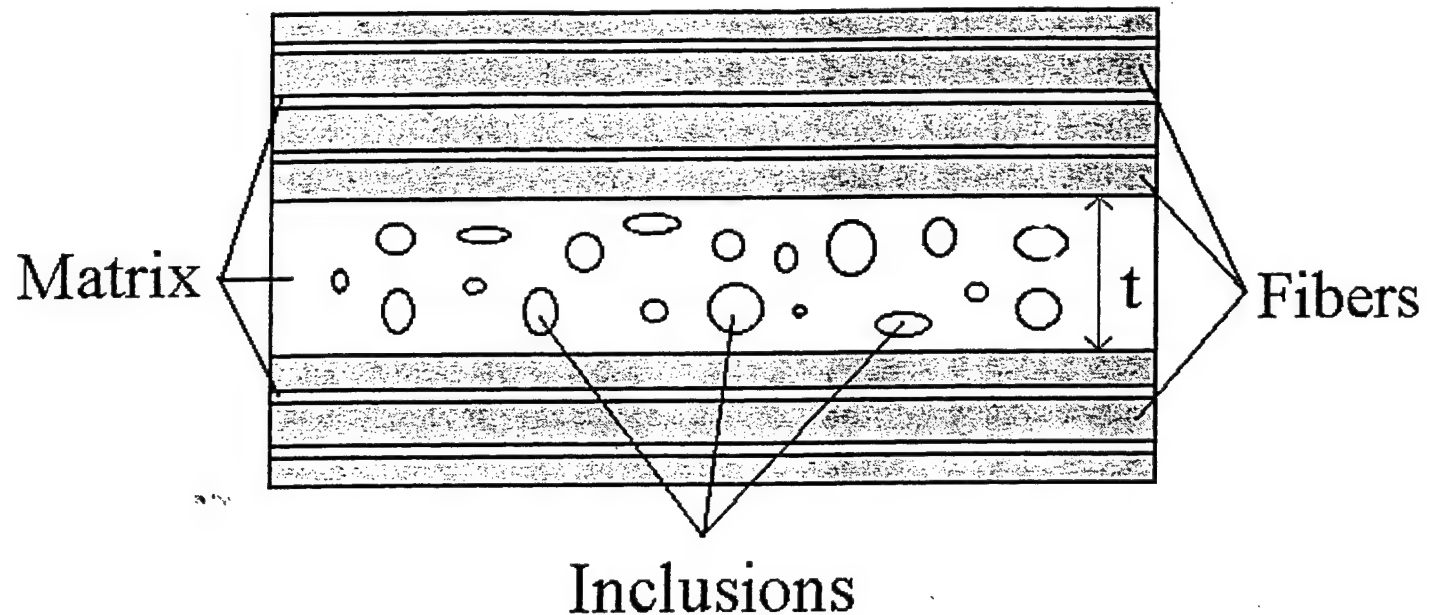


Figure 1a

Intralaminar Model

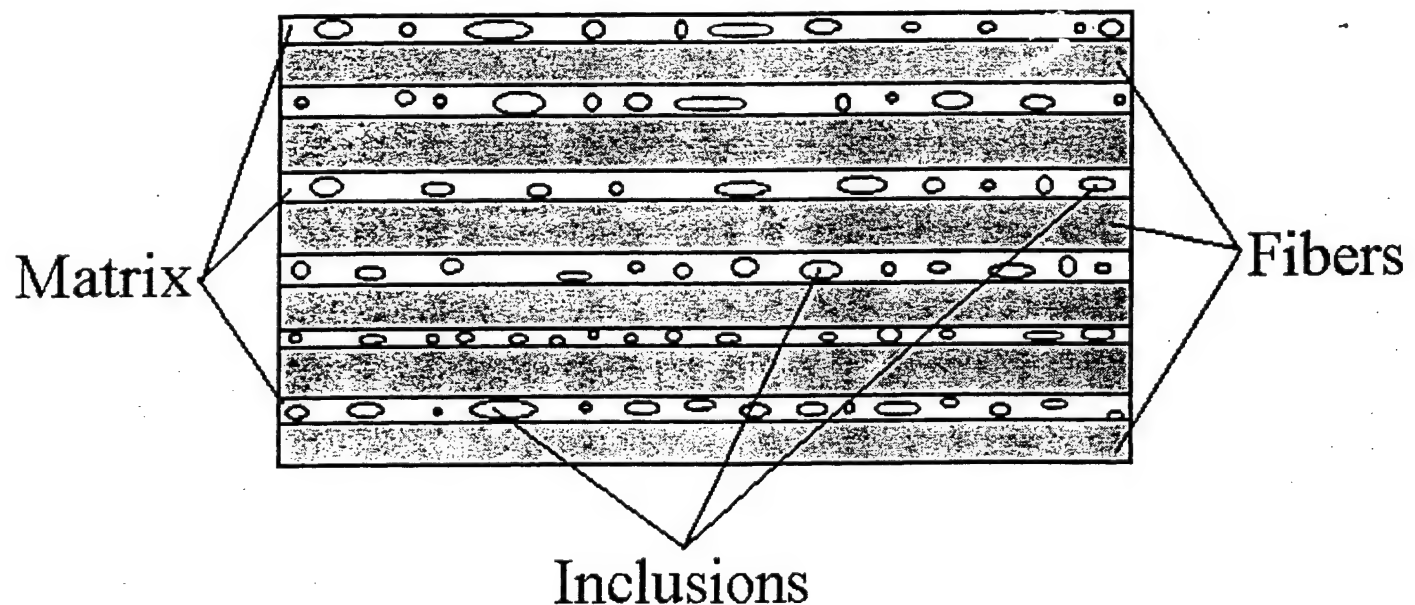


Figure 1b

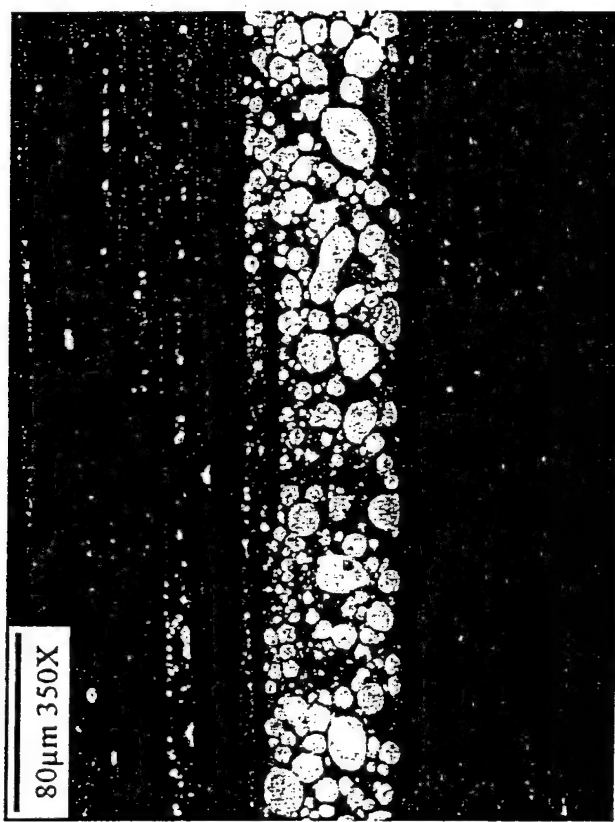


Figure 2a

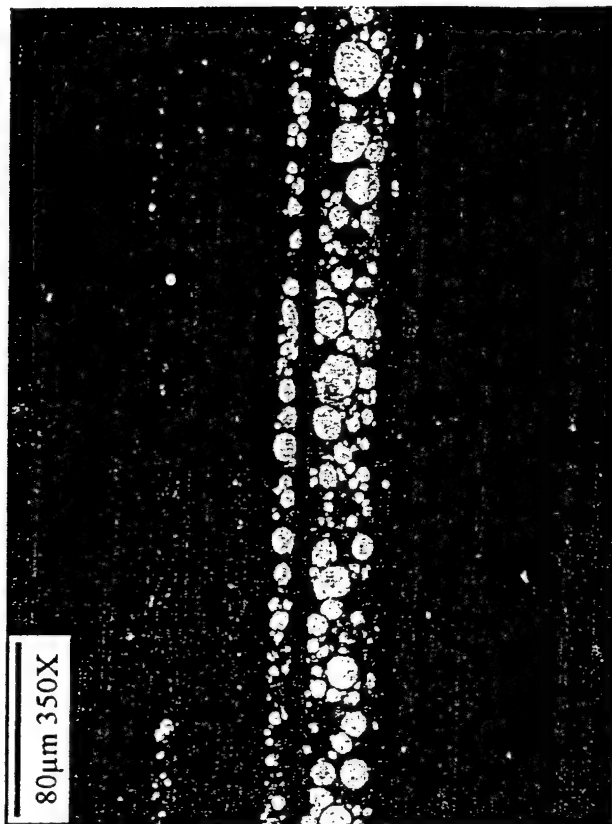


Figure 2b

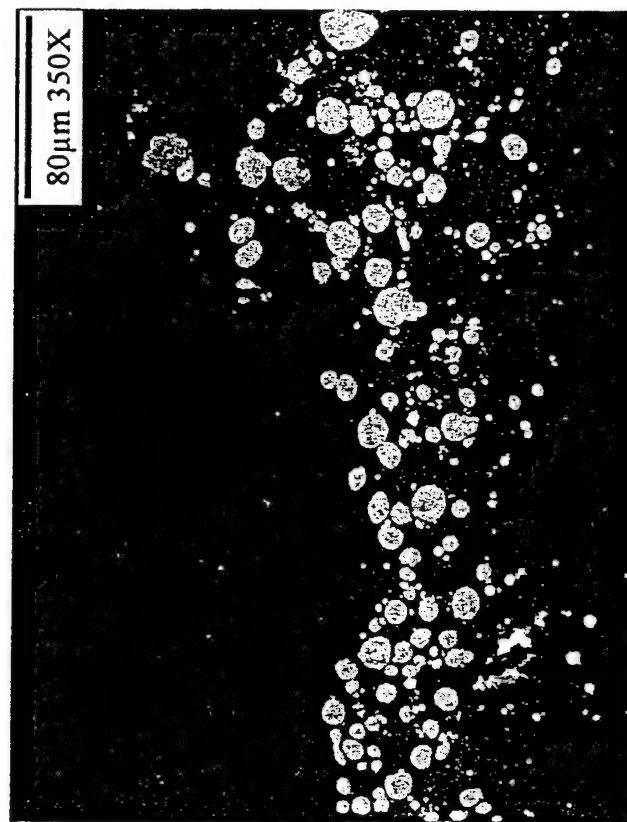


Figure 2c

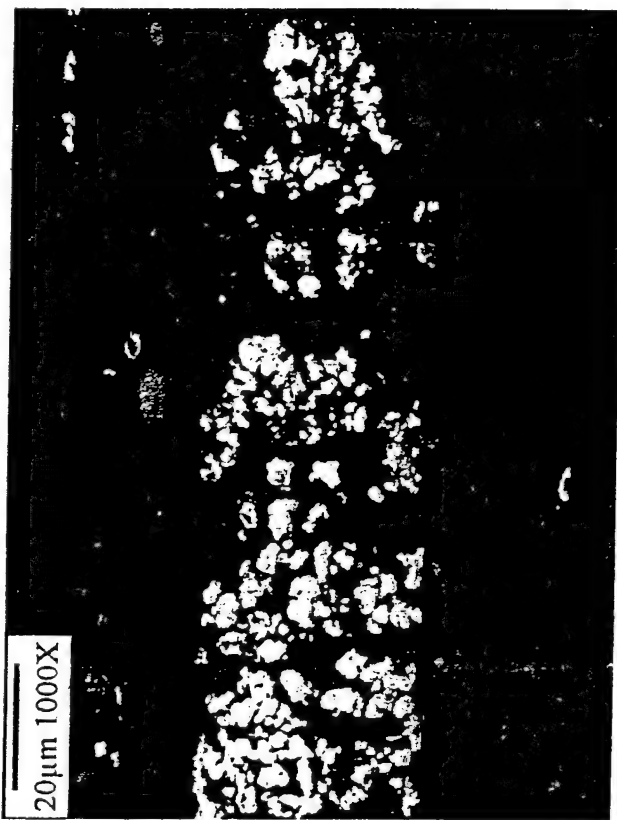


Figure 3a

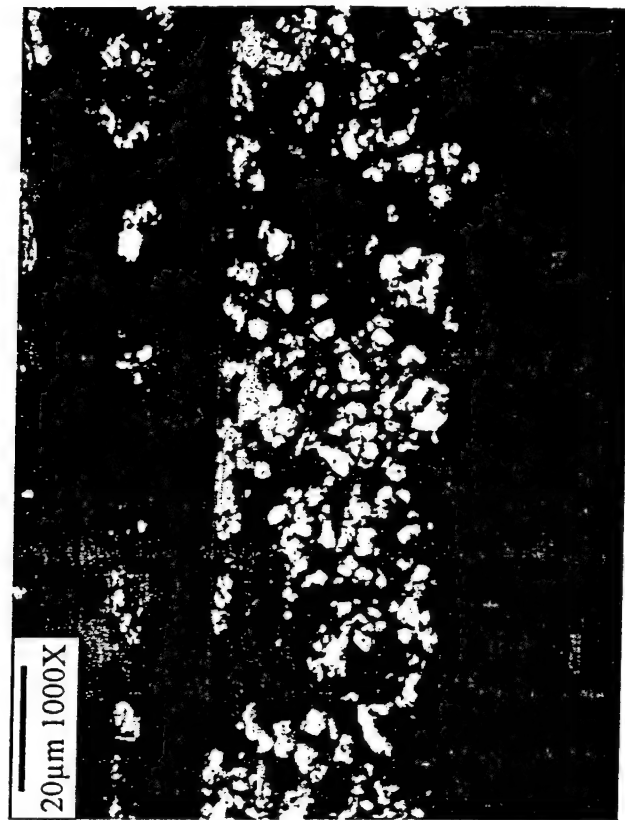


Figure 3b

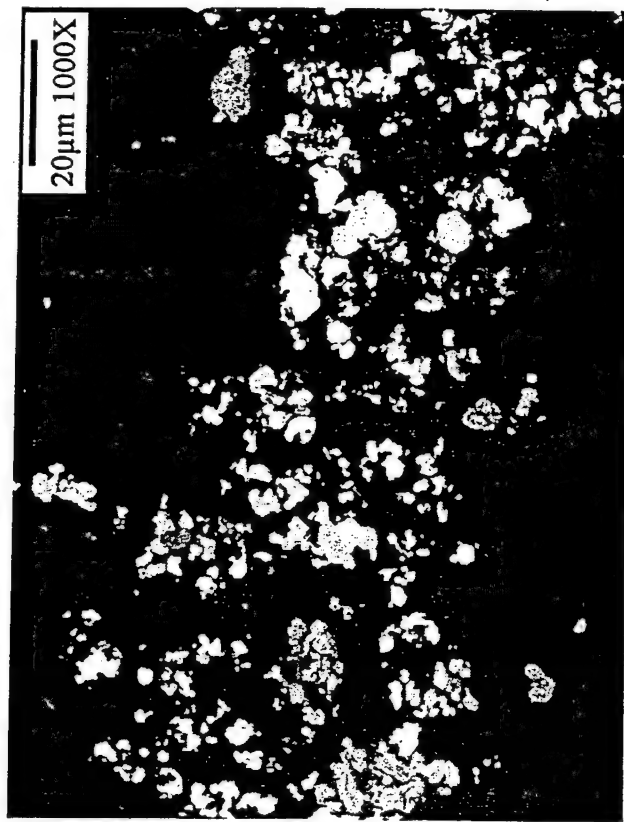


Figure 3c

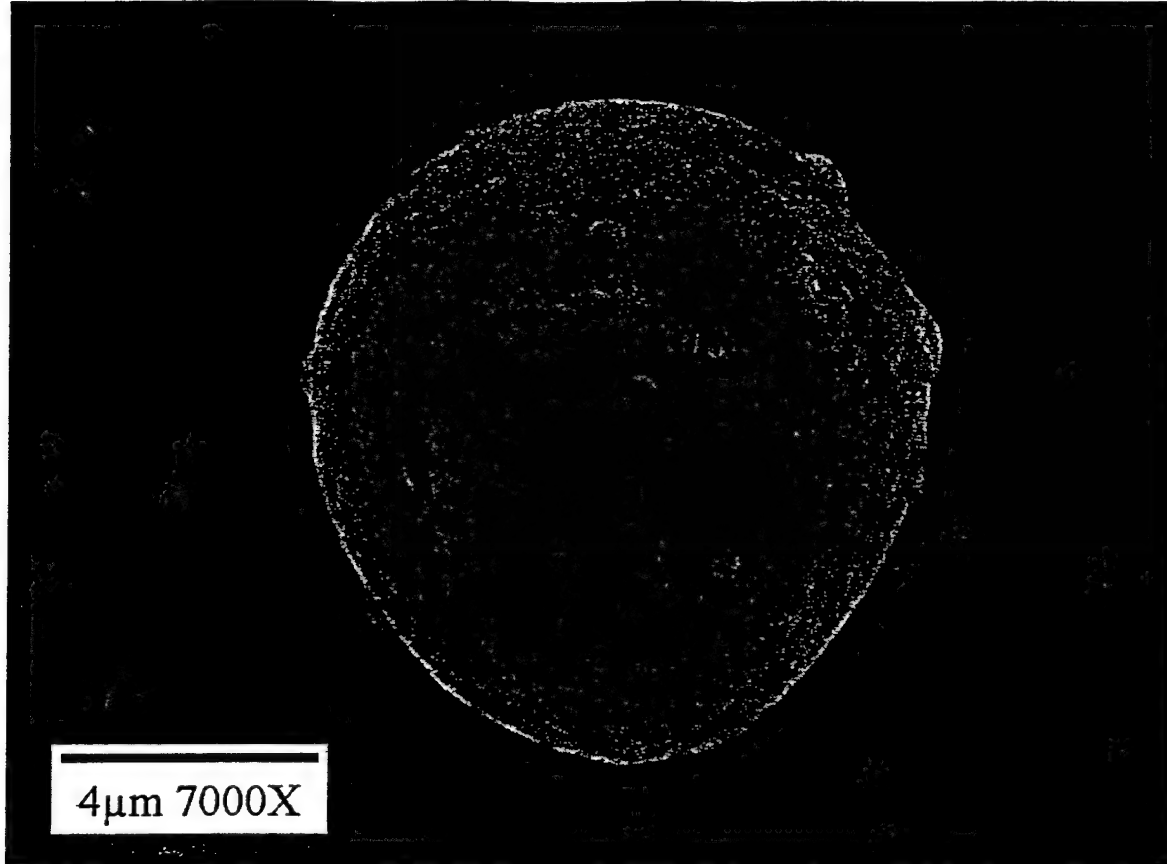


Figure 4a

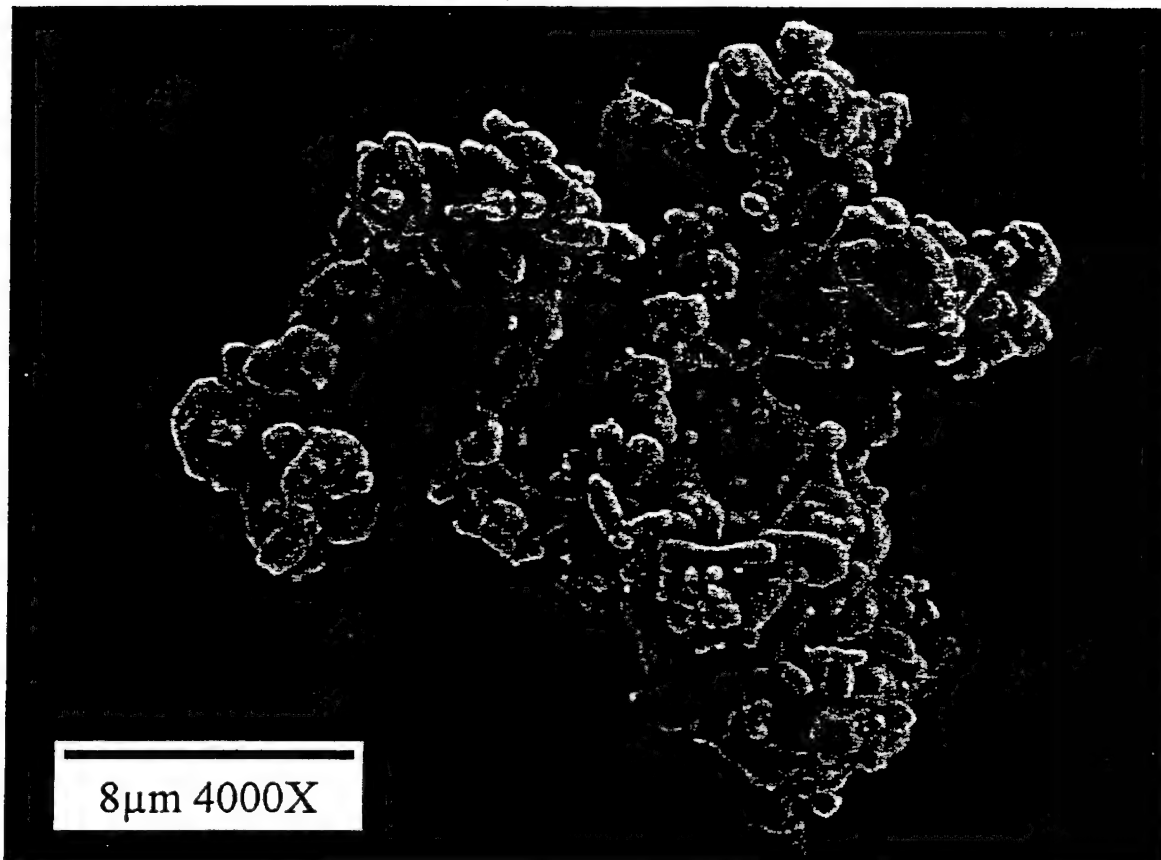


Figure 4b

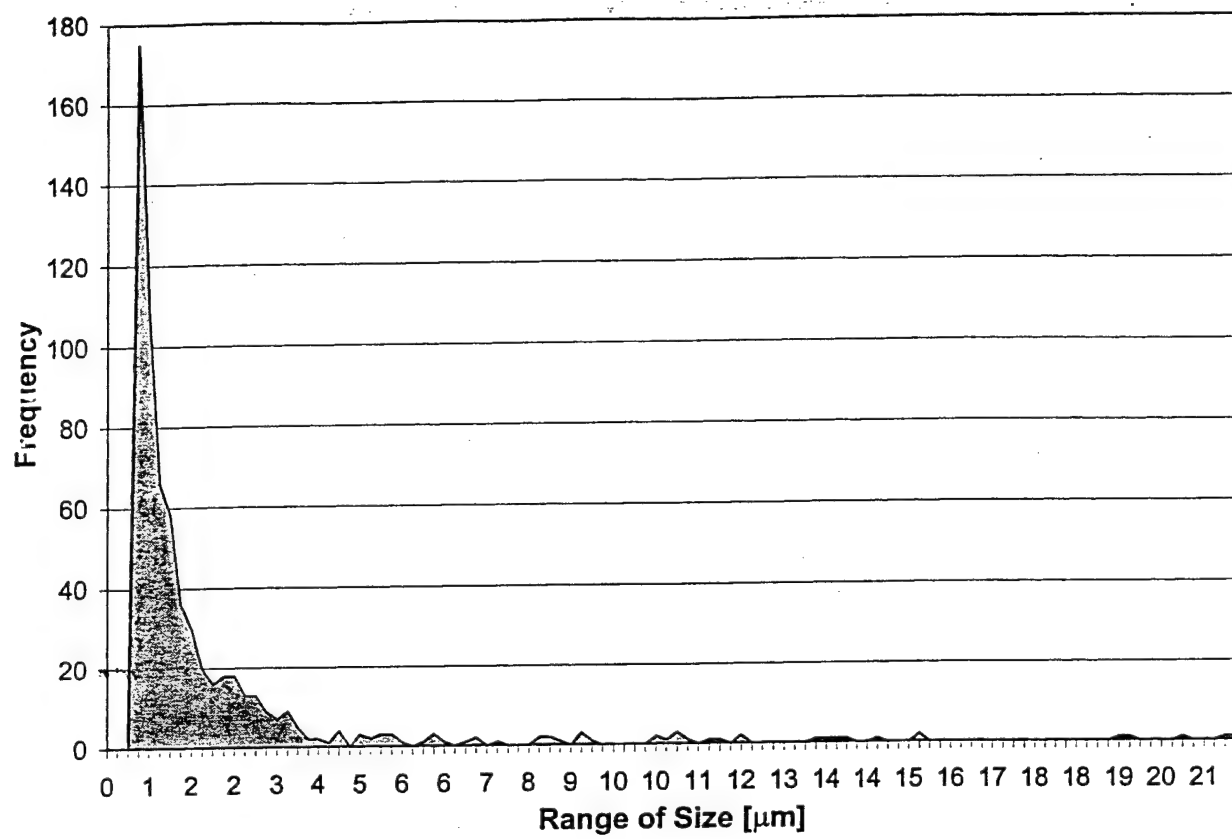


Figure 5a

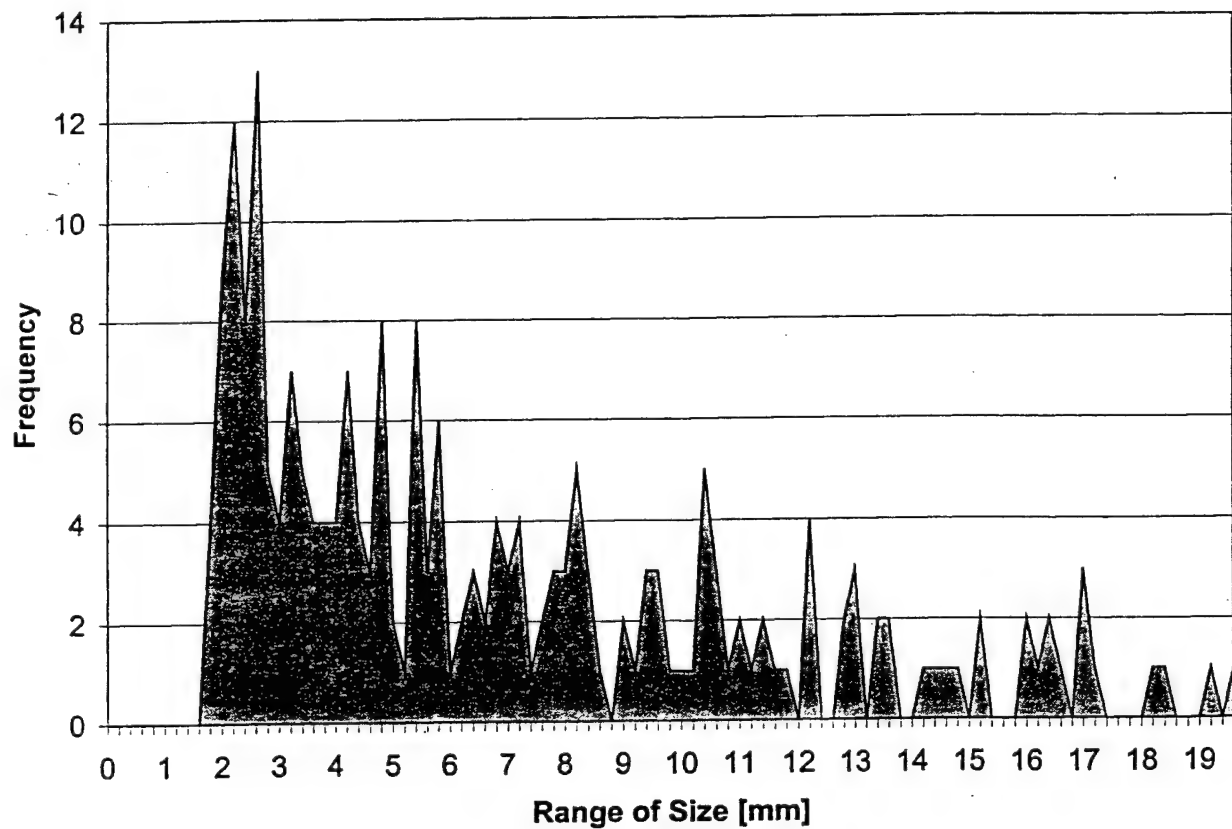


Figure 5b

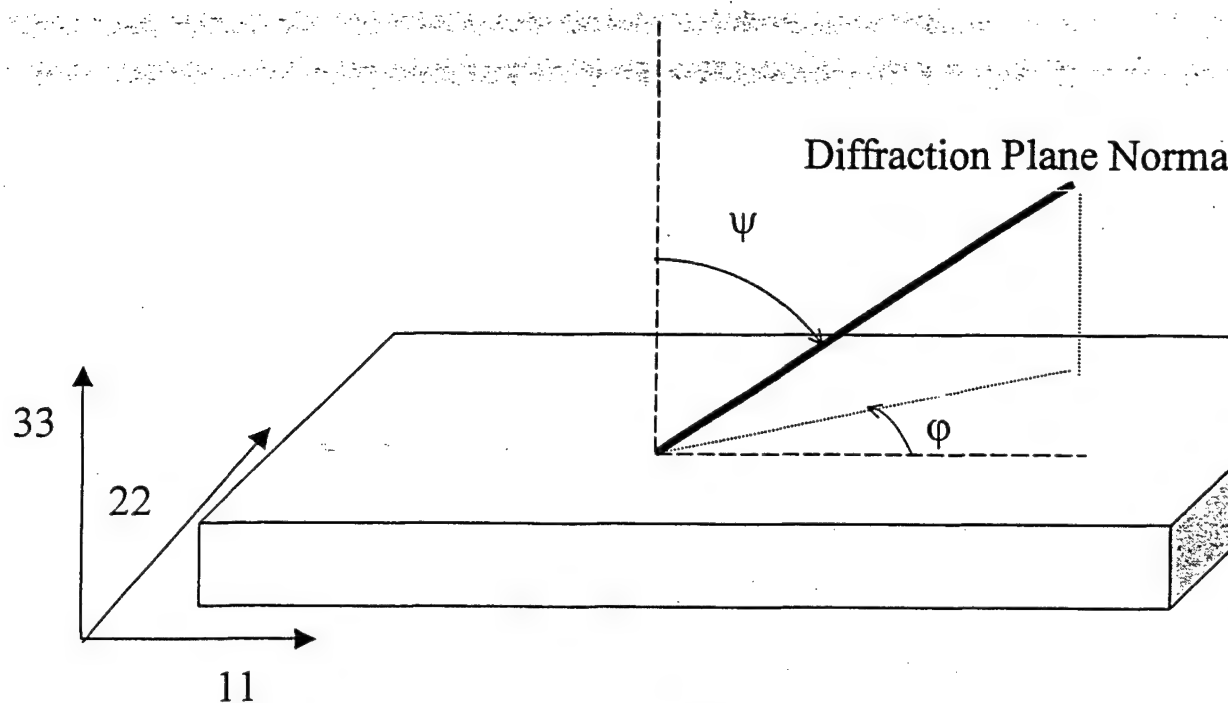


Figure 6

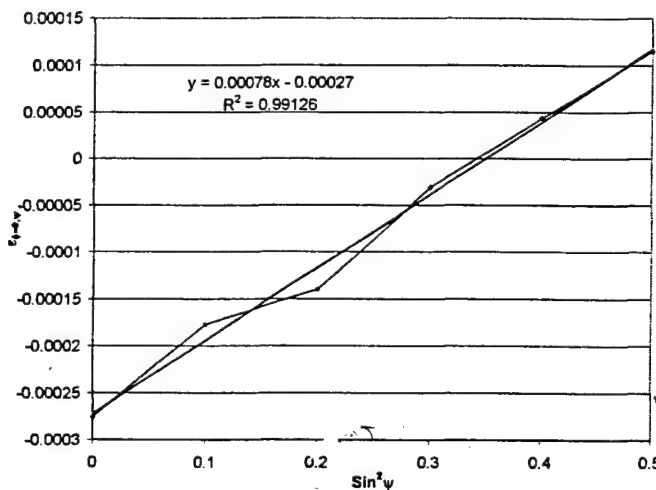


Figure 7a

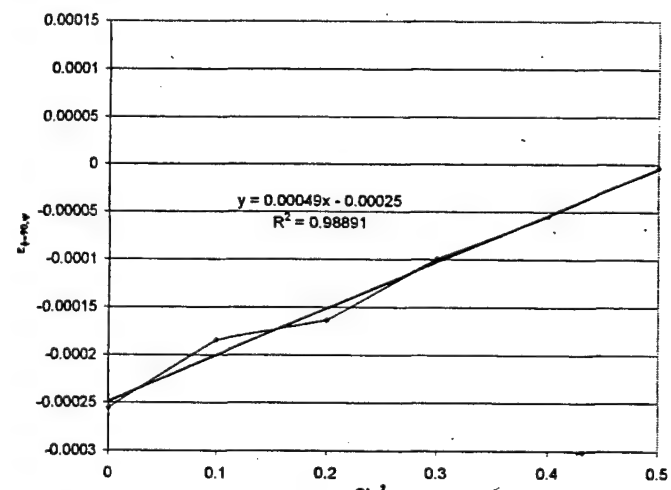


Figure 7b

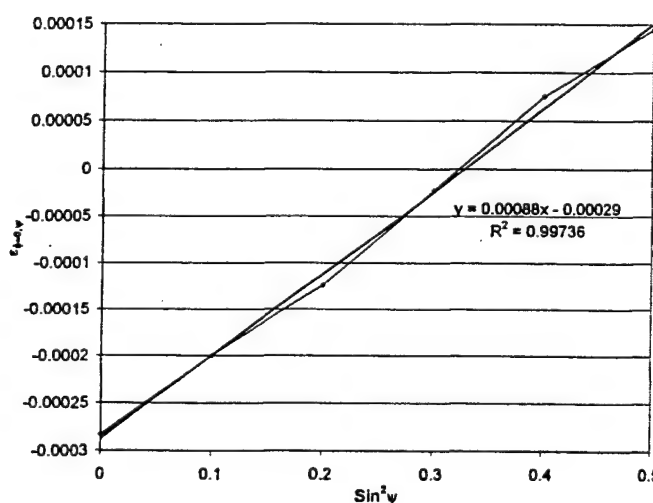


Figure 7c

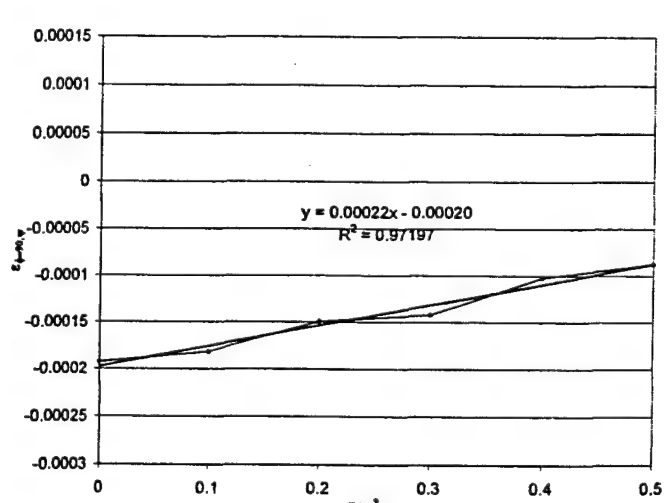


Figure 7d

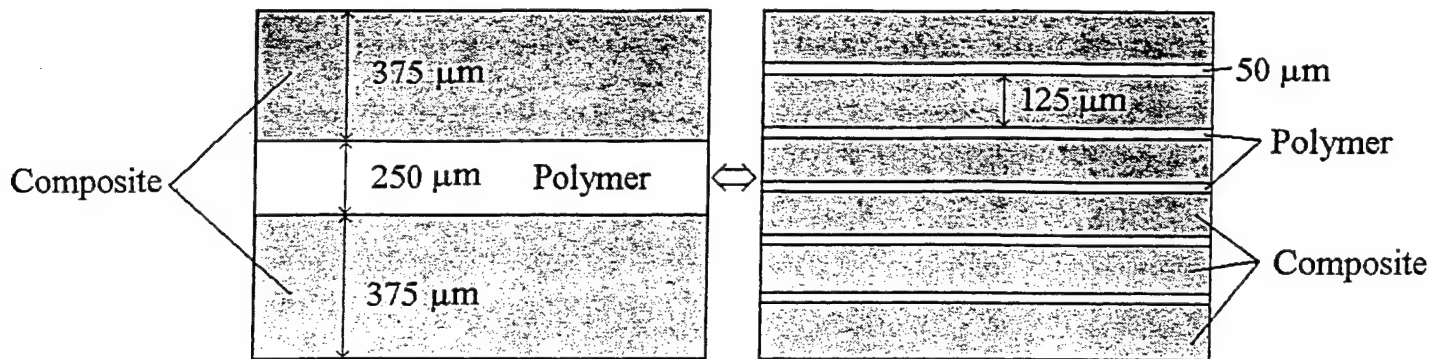


Figure 8

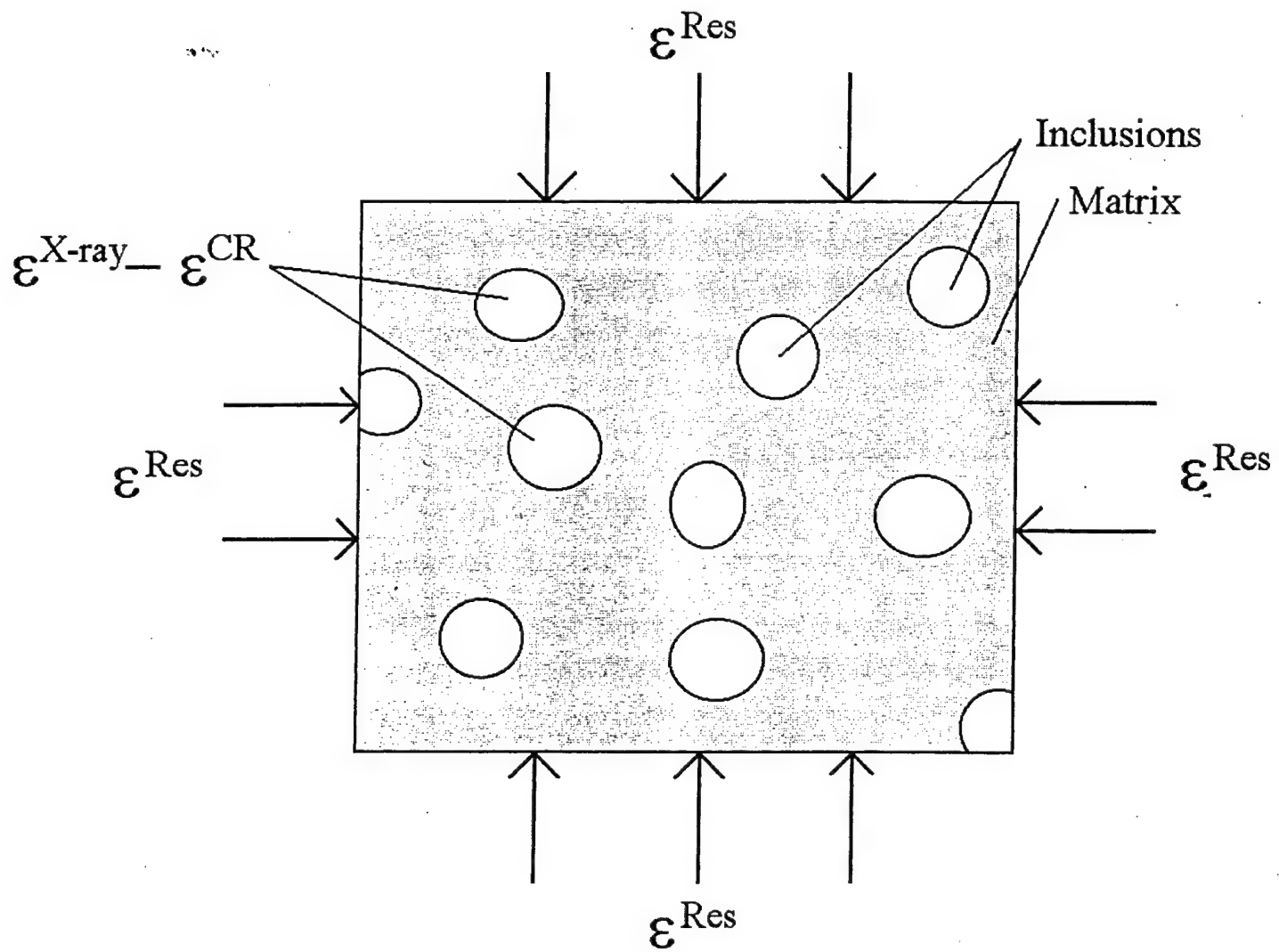


Figure 9

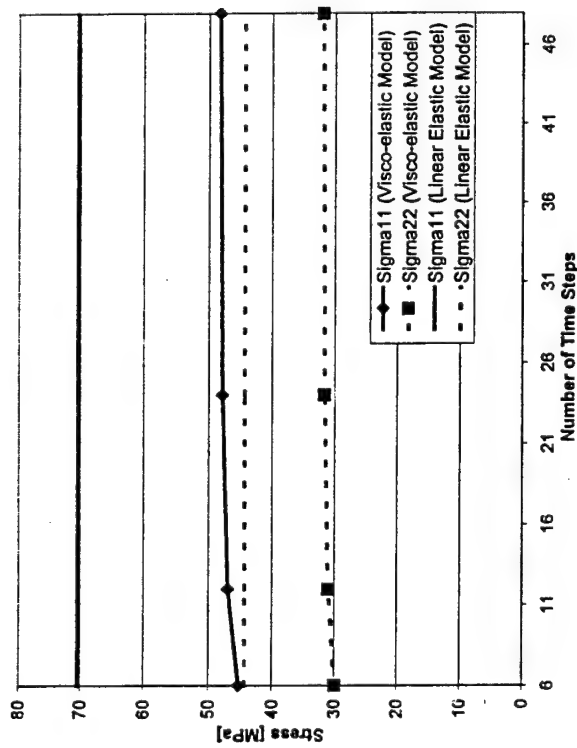


Figure 10a

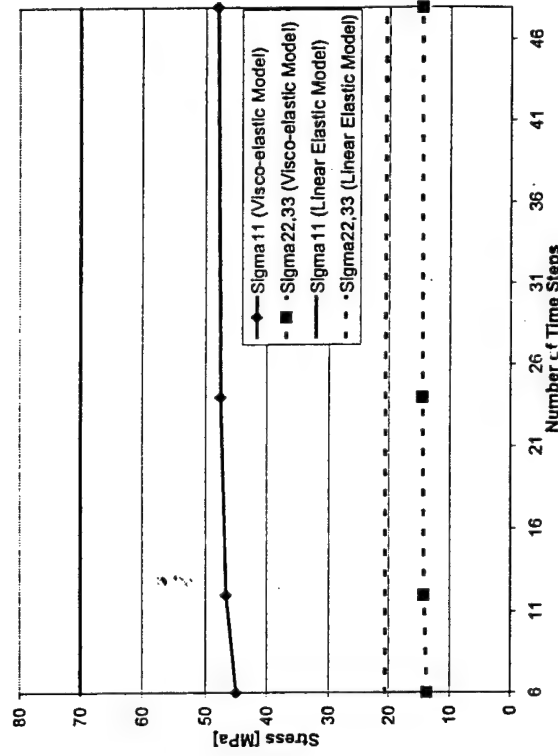


Figure 10b

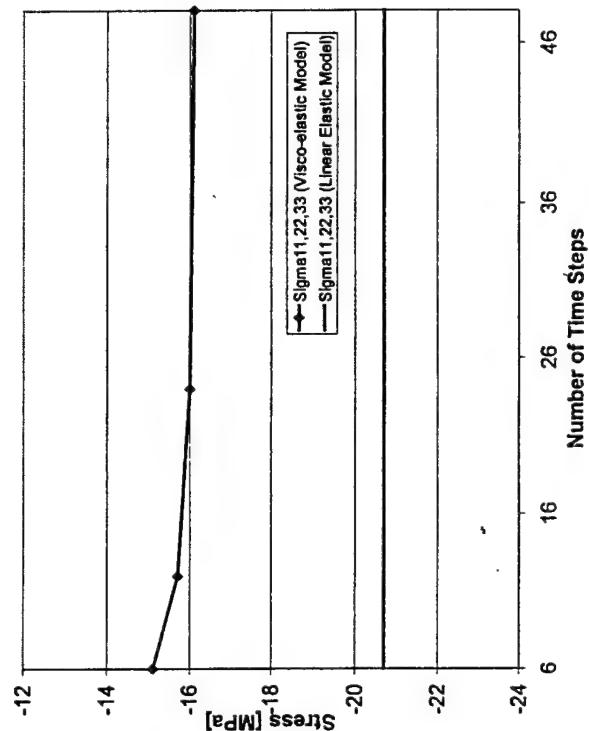


Figure 10c

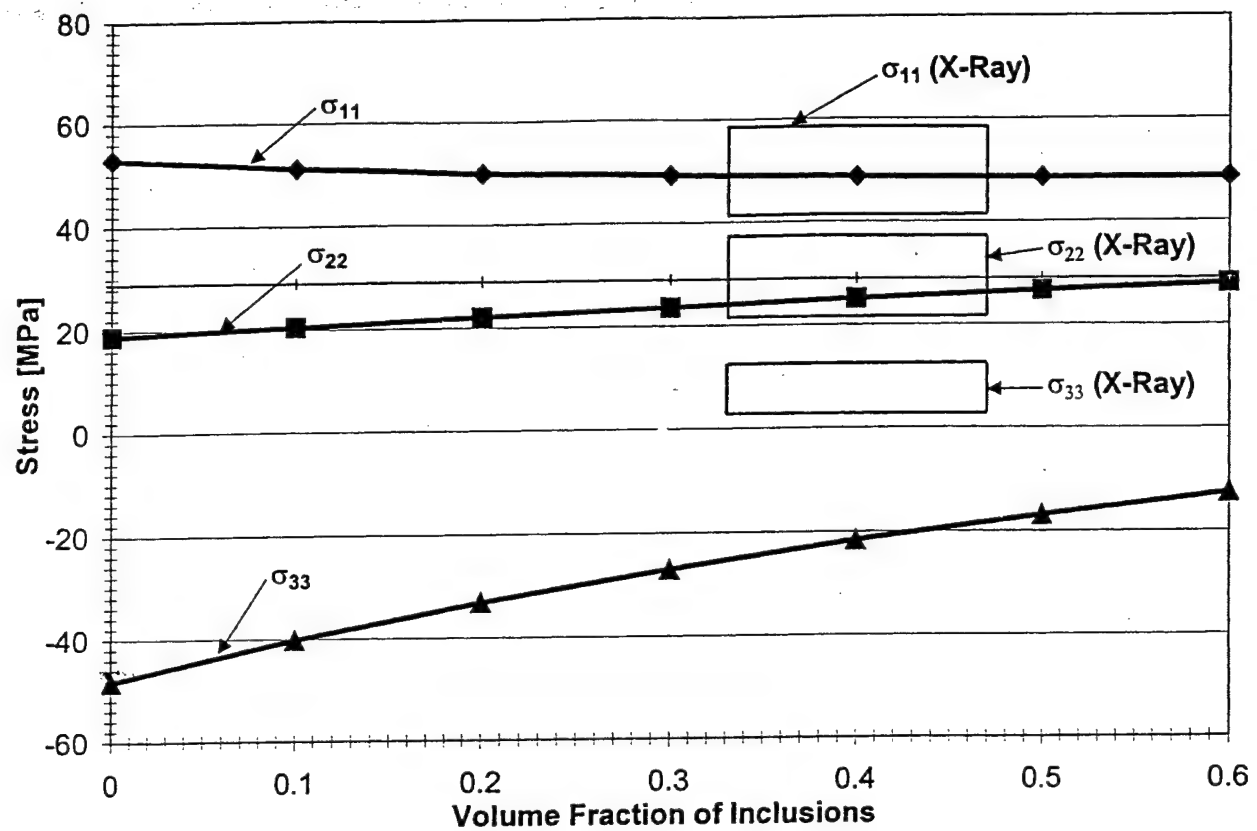


Figure 11a

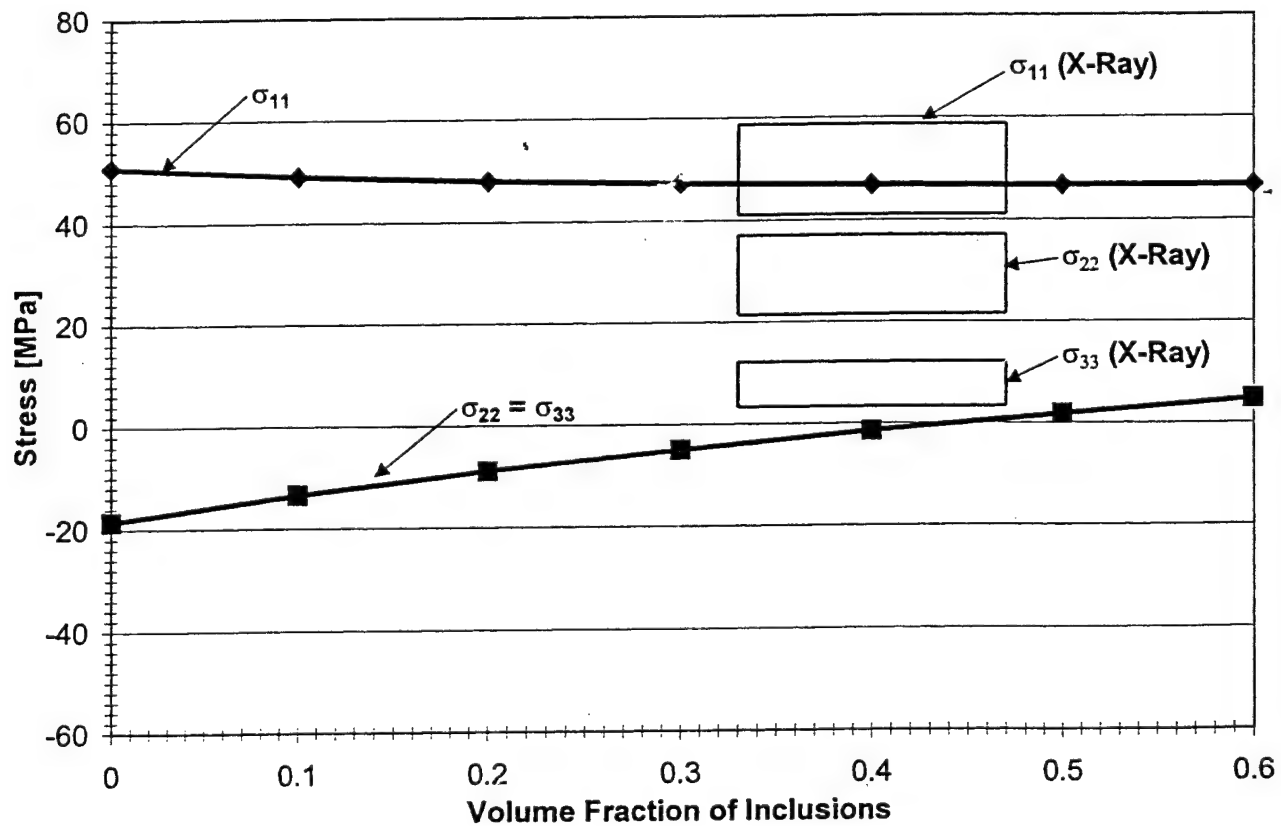


Figure 11b

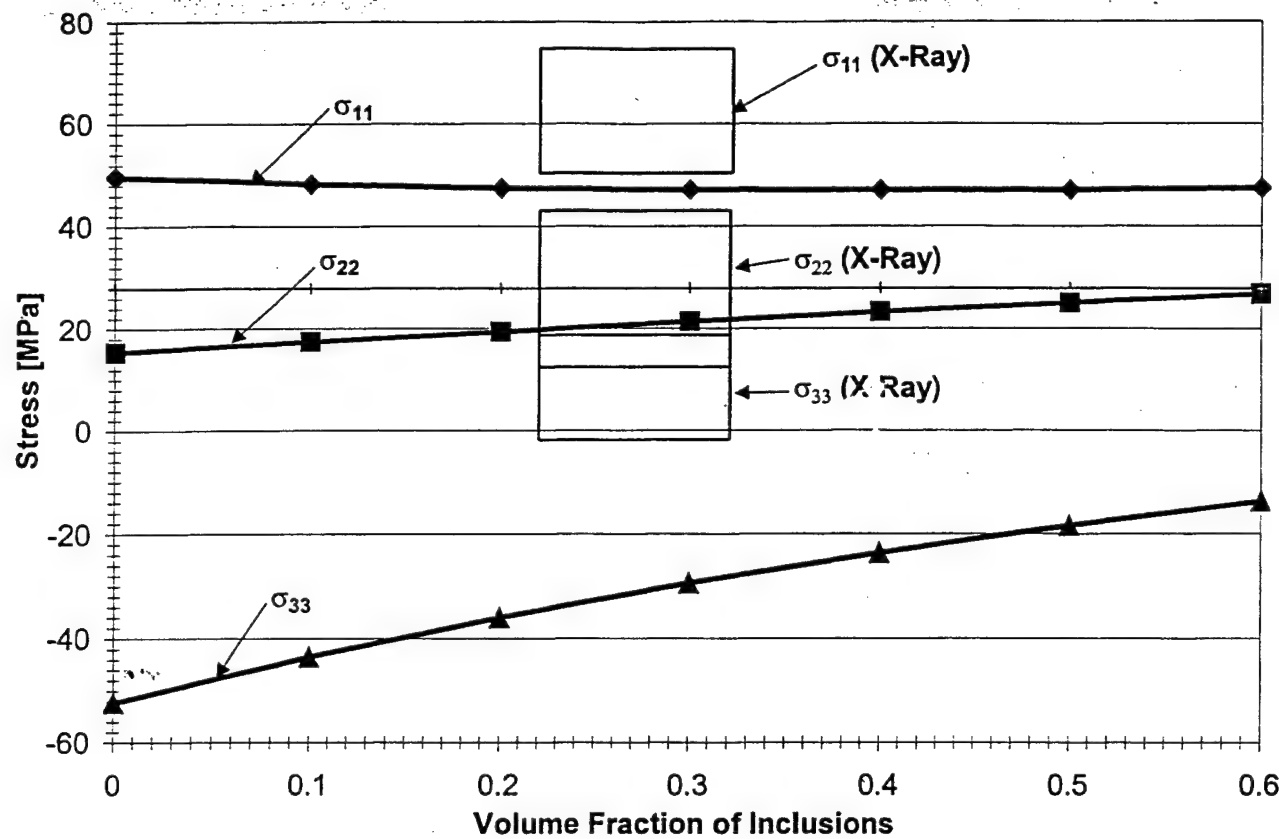


Figure 12a

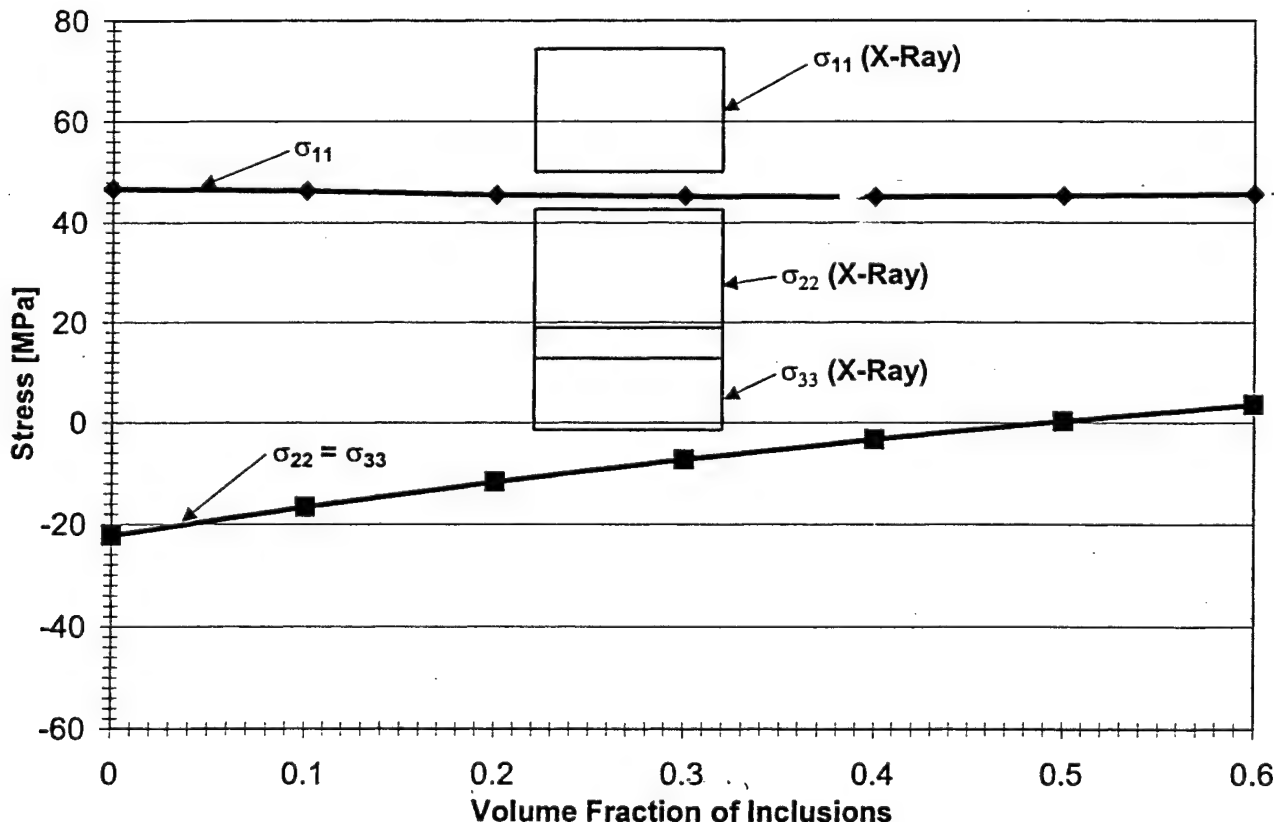


Figure 12b

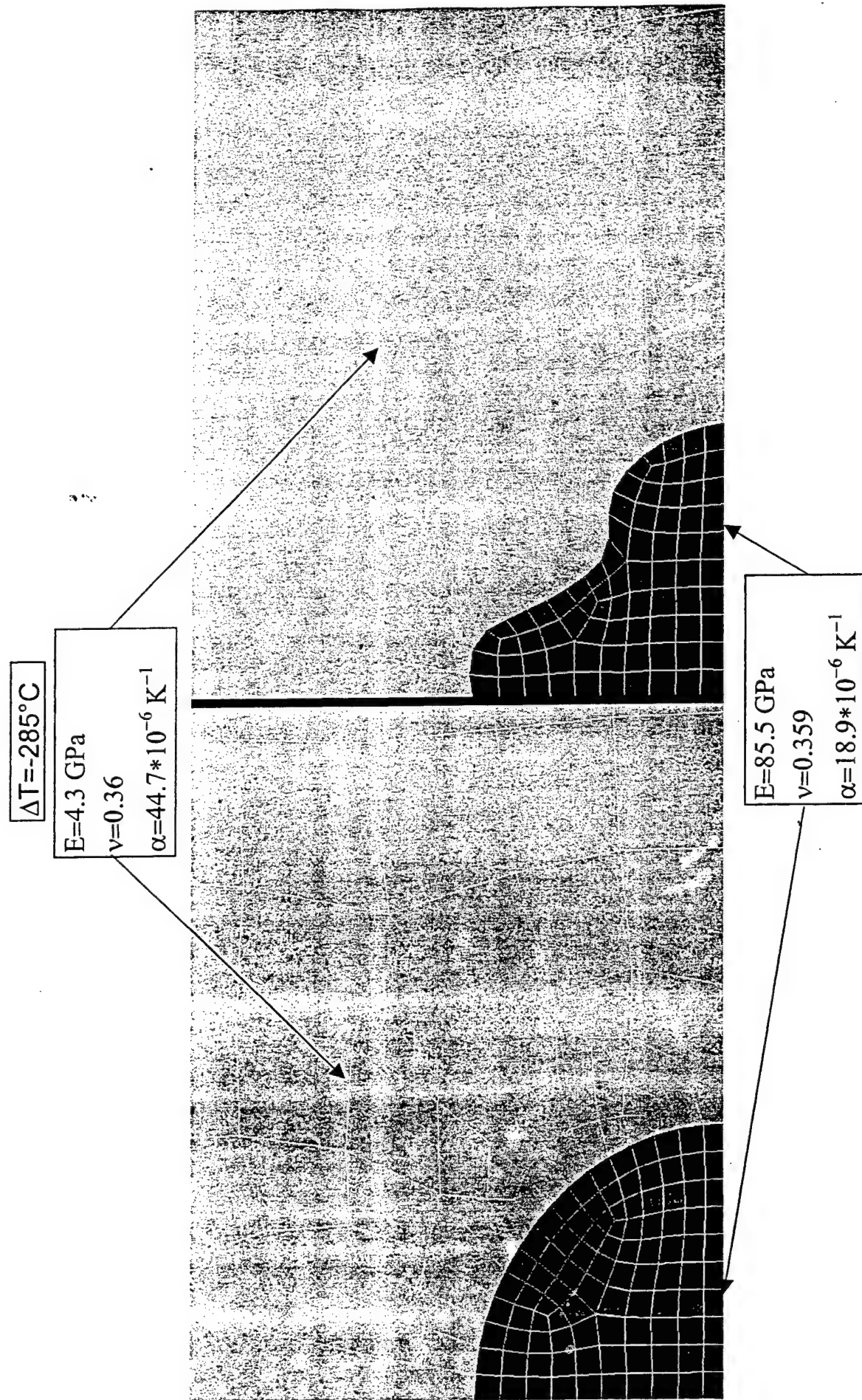


Figure 13

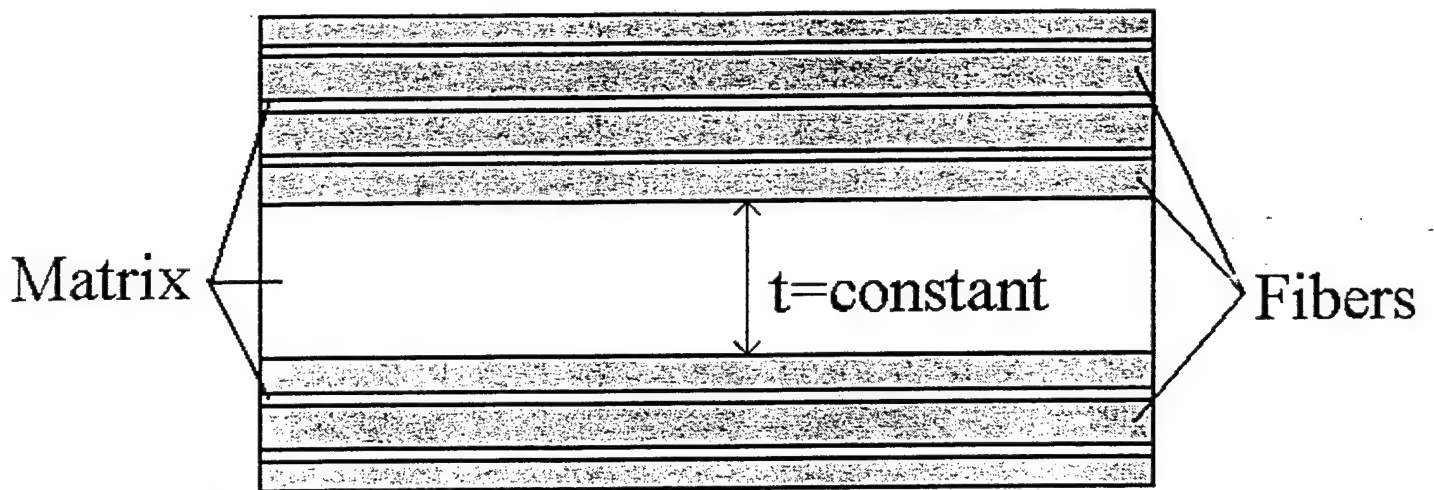


Figure 14a

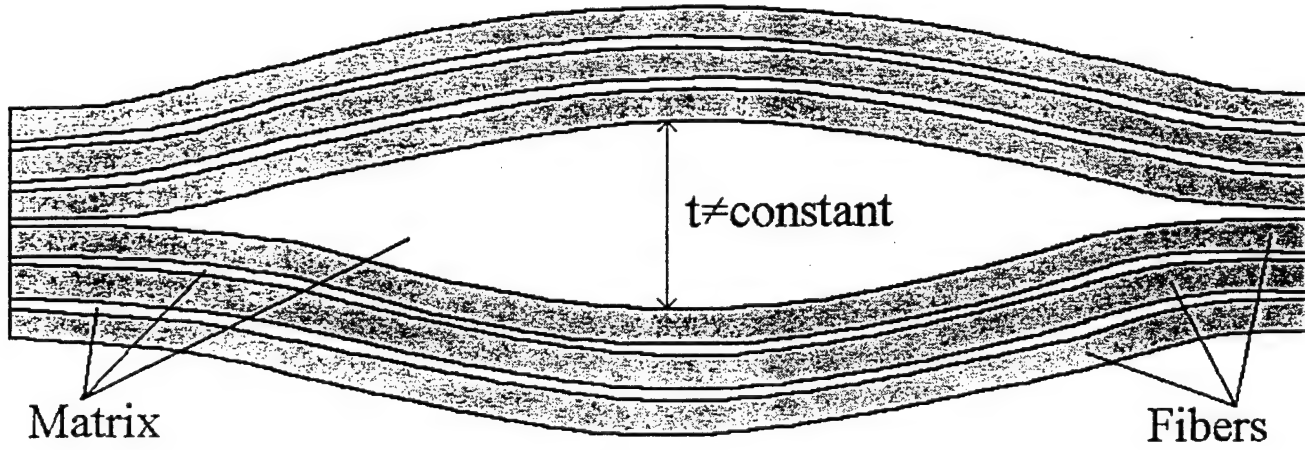


Figure 14b

Composites Science & Technology, in press.

**The Use of X-Ray Diffraction Measurements to Determine the Effect Of
Bending Loads on Internal Stresses in Aluminum Inclusions Embedded
in a Unidirectional Graphite-Fiber/PMR-15 Composite**

B. Benedikt, P. K. Predecki, L. Kumosa, D. Armentrout, J. K. Sutter*
and M. Kumosa

**Center for Advanced Materials and Structures
Department of Engineering
University of Denver
2390 South York St., Denver, Colorado 80208**

***NASA Glenn Research Center at Lewis Field
21000 Brookpark Rd.
Cleveland, OH 44135**

Abstract

A testing methodology for the determination of residual thermal stresses in the polymer matrix of unidirectional polymer matrix composites has been proposed in Ref. 1. The methodology is based on X-ray diffraction (XRD) measurements of residual strains in embedded metallic particles. The residual stresses in the polymer matrix can be extracted from the X-ray strains in the particles using the visco-elastic Eshelby method of multiple inclusions. The purpose of this work has been to show that the newly developed experimental/analytical methodology can also be applied to composites subjected to external loads, in this case: spherical Al particles embedded in a unidirectional graphite/PMR-15 composite subjected to four point bending loads. The total stresses and strains in the Al particles caused by residual thermal stresses in the composite and the applied stresses generated by four point bending have been determined by XRD measurements under low bending displacements. Subsequently, the total strains and stresses in the Al particles have been numerically predicted by applying elastic and visco-elastic laminate theories and the Eshelby method. It has been shown in this research that

not only the residual thermal strains and stresses in the Al particles and the matrix can be determined using the proposed technique but also the effect of external loads on the stresses and strains in the particles can be monitored. This research has provided another verification of the newly proposed methodology presented in Ref. 1.

1. Introduction

There are several analytical/numerical and experimental techniques that can be used to evaluate residual thermal stresses in polymer matrix composites [1-14]. One of them is based on the determination of residual strains inside embedded crystalline particles in a polymer matrix composite by performing X-ray diffraction (XRD) measurements [1, 10-14]. It was shown by Predecki and Barrett [10-12] that residual and applied strains transferred to various crystalline particles were high enough to be detected by XRD. However, knowing the state of strain in the particles from XRD measurements, they were unable to determine the actual residual stresses in the surrounding polymer matrix. A new experimental/numerical methodology for the evaluation of residual stresses in the polymer matrix of unidirectional polymer matrix composites based on XRD measurements of residual stresses in embedded crystalline particles has been recently developed by Benedikt et al. [1]. First, the residual thermal stresses in a unidirectional graphite/PMR-15 polyimide composite were determined by performing visco-elastic computations assuming interlaminar and intralaminar composite architectures. Secondly, the residual stresses in Al and Ag particles were obtained through XRD measurements and from the application of the visco-elastic Eshelby method for multiple ellipsoidal inclusions. Finally, the residual stresses in the polymer matrix were extracted from the X-ray strains and stresses in the particles and subsequently compared with the stresses obtained from the interlaminar and intralaminar analyses. The newly developed methodology has also been applied to the determination of the residual thermal stresses in an 8 harness satin woven graphite/PMR-15 composite [14].

In this study, residual and applied strains and stresses in Al particles embedded in a unidirectional graphite/PMR-15 unidirectional composite subjected to four point bending

were determined through X-ray diffraction measurements. The total residual and applied strains and stresses in the particles were subsequently determined numerically by performing elastic and visco-elastic laminate analyses and by using the elastic and visco-elastic Eshelby method for multiple inclusions.

2. X-ray Diffraction Measurements

2.1 Measurements of strains in Al particles under four point bending conditions

Strains inside Al particles embedded in the polymer matrix of unidirectional graphite/PMR-15 composite specimens were measured using XRD as a function of axial strain under four point bending conditions. The particles were placed between the first and second plies of 6-ply unidirectional graphite/PMR-15 laminates during lay-up (see Figures 1a and 1b). The specimens used in the XRD experiments were manufactured at NASA Glenn Research Center. The physical properties of the composite specimens, the particle distributions and a description of the manufacturing procedure have already been presented in Ref. 1. The Al particles were nearly spherical in nature and their average volume concentration in particle rich regions was approximately $40 \pm 7\%$. The specimens were 50 mm long, 16 mm wide and their thickness was 0.9 mm.

To measure the state of strain inside the particles the $\sin^2\psi$ procedure was used [15]. The specimens were mounted in a four point bending fixture and subsequently put into a Siemens D-500 diffractometer (Figures 2a,b) fitted with pseudo parallel-beam optics. The location of the specimen surface was checked with a dial gage and micro flat and was adjusted so that the plane of particles in the specimen coincided with the θ -axis of the goniometer to ± 0.125 mm. The direction of the diffraction vector (diffracting plane normal) with respect to the specimen's coordinates was determined by two angles: ψ and φ (see Figure 3). Measurements of the Al (422) lattice spacing, $d_{\varphi\psi}$ were made at $\varphi=0^\circ$ and 90° and at six ψ angles from 0° to 45° for each φ angle. The direction $\varphi=0$ was chosen parallel to the fibers.

The strain components ε_{ij} ($i,j=1, 2, 3$) inside the Al inclusions in the specimen coordinate system were obtained from:

$$\begin{aligned}\varepsilon_{\varphi\psi} = \frac{d_{\varphi\psi} - d_0}{d_0} &= \varepsilon_{11} \cos^2 \varphi \sin^2 \psi + \varepsilon_{12} \sin 2\varphi \sin^2 \psi + \\ &\quad \varepsilon_{22} \sin^2 \varphi \sin^2 \psi + \varepsilon_{33} \cos^2 \psi + \varepsilon_{13} \cos \varphi \sin 2\psi + \varepsilon_{23} \sin \varphi \sin 2\psi\end{aligned}\quad (2)$$

where the value of the 422 strain-free lattice spacing d_0 measured on the starting Al powder was corrected to the same temperature as that at which the corresponding $d_{\varphi\psi}$ measurements were made using the thermal expansion coefficient of pure Al. Details of the measurement conditions are given elsewhere [1].

Assuming the specimen axis (Figure 3) were the principal axes, and taking the angle $\varphi = 0$ and 90° , equation 2 gives respectively:

$$\varepsilon_{\varphi=0,\psi} = \frac{d_{\varphi=0,\psi} - d_0}{d_0} = (\varepsilon_{11} - \varepsilon_{33}) \sin^2 \psi + \varepsilon_{33} \quad (3a)$$

$$\varepsilon_{\varphi=90,\psi} = \frac{d_{\varphi=90,\psi} - d_0}{d_0} = (\varepsilon_{22} - \varepsilon_{33}) \sin^2 \psi + \varepsilon_{33} \quad (3b)$$

The normal strain ε_{33} was taken to be the average of $\varepsilon_{\varphi=0,\psi=0}$ and $\varepsilon_{\varphi=90,\psi=0}$. In order to determine the slope of the $\varepsilon_{\varphi\psi}$ vs. $\sin^2 \psi$ plots the least squares method was used. The strain components ε_{11} and ε_{22} in the inclusions were obtained from the slopes of the $\sin^2 \psi$ plots at $\varphi=0^\circ$ and 90° , respectively. To determine residual stresses in the particles, X-ray elastic constants for the 422 reflection were calculated by taking the mean of the Reuss and Voigt models [15, p.70], using literature values of the single crystal elastic compliances. This procedure yielded Young's modulus E and Poisson ratio ν values of $E=71$ GPa, $\nu=0.351$ for aluminum. The stresses in the particles were subsequently calculated from the strains assuming isotropic Hooke's law.

2.2 Measurements of strains inside Al particles with externally applied loads

The bending moment applied to the specimen was generated by a four point bending fixture mounted on the goniometer. The positions of the pins are shown in Figure 2b, where arrows denote the pins that push the specimen down. The magnitude of axial strain on the upper surface of the specimen was monitored by a strain gage. After the desired value of the strain was applied, the position of the specimen was once again checked by a dial gage and adjusted so that the plane of the particles again coincided with the θ -axis to ± 0.125 mm. The specimen was subsequently subjected to X-ray radiation and the strains inside the Al particles corresponding to a given applied axial strain were obtained. The $\sin^2\psi$ plots, with and without externally applied loads, all showed regular (linear) behavior as shown later in Figure 6 and also in reference [1].

3. Determinations of global strains in the four point bend specimens as a function of applied displacement.

3.1 Mechanical four point bend tests

The four point bend VRD tests were performed with the outer pins subjected to externally applied displacements (see Figure 2b). The load was not monitored during testing. Therefore, it was important to determine the actual strains and loads in the composite specimens as a function of applied displacement. The fixture was placed on an MTS loading rig and the load/displacement and load/axial strain curves were obtained.

3.2 Analytical and numerical determination of strains.

First order laminated plate theory was used to predict the loads necessary to displace the outer pins by a certain distance [16]. The resulting fourth order partial differential equation was solved by expanding both the unknown loads and displacements on a neutral plane of the composite specimen in a Fourier series. By employing the Fourier

series approach, it was possible to reduce the partial differential equation to an ordinary differential equation, which could then be solved explicitly. Knowing the displacements, the corresponding strains were obtained by simple differentiation. To verify the analytical predictions of the strains in the composite specimens, a three-dimensional non-linear finite element model of the four-point bend test was constructed (see Figure 4). Due to the symmetry conditions, one quarter of the specimen, with the corresponding pins were modeled. The friction coefficients between the specimen and pins were assumed to be in the range from 0.05 to 0.35. Since the pins did not rotate in the actual XRD tests, no pin rotation was allowed in the FEM model. From the FEM analysis, strain distributions and loads were determined as a function of applied displacements and compared with the analytical predictions from laminate theory and the experimental data.

The analytical and numerical calculations of loads and strains in the composite specimens subjected to bending were performed taking the elastic properties from Odegard and Kumosa [17] measured for the same unidirectional graphite/PMR-15 composite. The following properties were used in the calculations: $E_{11} = 136$ GPa, $E_{22} = E_{33} = 9$ GPa, $G_{12} = 6.5$ GPa, $v_{12} = 0.45$ [17].

4. Calculations of Stresses and Strains inside Al Particles

4.1 Material properties

The PMR-15 matrix in the unidirectional composite was modeled as a visco-elastic material with its thermal expansion coefficient α depending upon temperature and its shear modulus G depending on both time and temperature. The Poisson's ratio of the resin was assumed to be constant. The experimental values of the shear modulus G as a function of time and temperature were taken from Ref. [18] and the thermal expansion coefficient of the polyimide post cured in air were provided by the NASA Glenn Research Center. The values of G and α were subsequently curve fitted to obtain $G(t, T)$ and $\alpha(T)$ functions. These relations are shown below.

$$G = 10^{(\text{Exp}(0.16(-\text{Log}(t)+6.5)^{0.5})+7.5)} \quad (4a)$$

$$a_v = 10^{\text{Exp}(0.012(-T+348)^{0.48})-1.076} \quad (4b)$$

$$a_h = 10^{\text{Exp}(0.41(-T+348)^{0.28})-4.3} \quad (4c)$$

$$\alpha = 3 \cdot 10^{-12} \cdot (104 + T) \cdot (127160 - 548 \cdot T + T^2) \quad (4d)$$

The shear modulus is given in equation 4a as a function of time at $T_{\text{ref}}=288^\circ\text{C}$ (the master curve). The vertical, $a_v(T)$, and horizontal, $a_h(T)$, shift functions were estimated from the data presented in Ref. [18]. The horizontal shift function is used in the definition of reduced time $\xi(t)$ (see equation 5).

$$\xi(t) = \int_0^t \frac{dt'}{a_h[T(t')]} \quad (5)$$

The application of the horizontal and vertical shift functions (equations 4b and 4c) allows the determination of the $G(t,T)$ function from the master curve. However, this is only valid for a temperature range from room temperature to 348°C and a range of time from 0 to $10^{6.5}$ seconds.

The thermal expansion coefficients of the fibers were taken as $\alpha_{Lf} = -0.5 \times 10^{-6} \text{ K}^{-1}$ (longitudinal), $\alpha_{Tf} = 10 \times 10^{-6} \text{ K}^{-1}$ (transverse). The elastic properties of the graphite fibers were assumed to be $E_{Lf} = 241 \text{ GPa}$ (longitudinal Young's modulus), $E_{Tf} = 20 \text{ GPa}$ (transverse Young's modulus), $K_f = 20 \text{ GPa}$ (bulk modulus), $\nu_{Lf} = 0.2$ (longitudinal Poisson ratio), $\nu_{Tf} = 0.4$ (transverse Poisson ratio), $G_{Lf} = 27 \text{ GPa}$ (longitudinal shear modulus), $G_{Tf} = 11 \text{ GPa}$ (transverse shear modulus).

4.2. Calculations of stresses and strains inside Al particles

The total states of stress and strain in the embedded Al particles are caused by both residual thermal stresses in the polymer matrix and by the externally applied load. Since the specimens were subjected to small displacements it was assumed that the superposition principle could be applied to this problem with the stresses and strains in the Al inclusions from residual stresses and from bending being treated separately. The problem of determining residual stresses in metallic spherical particles has already been addressed in Ref. [1]. Using the methodology already developed, the residual stresses and strains in the Al inclusions, without bending, due to differences in thermal expansion coefficients of all constituents (polymer matrix, graphite fibers and Al inclusions) can be calculated. The contribution coming from the applied external bending was calculated using a very similar approach, namely the Eshelby method modified by Tanaka and Mori to account for multiple inclusions effect [19-21]. The equations used in the present analysis are:

$$\sum_{i=0}^{f-1} C_I \left(S(\varepsilon^T(i) + \varepsilon^R(i) + \varepsilon^{Res}(i+1) - \varepsilon^{Res}(i) - \varepsilon^{T*}(i) + \varepsilon^{Bend}(i)) \right) = \\ \sum_{i=0}^{f-1} C_M (\xi(f) - \xi(i)) \left(S\varepsilon^T(i) + \varepsilon^R(i) + \varepsilon^{Res}(i+1) - \varepsilon^{Res}(i) - \varepsilon^T(i) + \varepsilon^{Bend}(i) \right) \quad (6a)$$

$$\varepsilon^R(j) + V_f (S\varepsilon^T(j) - \varepsilon^T(j)) = 0, \text{ for } j=0, 1, 2, \dots, f \quad (6b)$$

$$\sigma_{particle}(f) = \sum_{i=0}^{f-1} C_I \left(S(\varepsilon^T(i) + \varepsilon^R(i) + \varepsilon^{Res}(i+1) - \varepsilon^{Res}(i) - \varepsilon^{T*}(i) + \varepsilon^{Bend}(i)) \right) \quad (6c)$$

where S is the Eshelby tensor for spherical inclusions, C_I is the tensor of the elastic properties of the Al inclusions, C_M is the tensor of the elastic properties of the matrix, ε^T is the stress free transformation strain, ε^{Res} is the average residual thermal strain in the matrix, ε^{T*} is the stress free transformation strain of the inhomogeneous inclusion, ε^R is

the average strain caused by the presence of many Al inclusions, f is the number of steps used in the visco-elastic analysis, and V_f is the volume fraction of the Al inclusions.

The strains and stresses in the inclusions were calculated at 30° C, which was the temperature at which the XRD tests were conducted. The effect of externally applied bending strain was accounted for by the term $\epsilon^{\text{Bend}}(i)$, which is equal to zero for all values of i except for $i=f-1$. The tensor $\epsilon^{\text{Bend}}(f-1)$ represents the strains in the polymer layer between the first and second unidirectional ply due to four point bending. Its magnitude was calculated using laminated plate theory [16].

5. Results and Discussion

5.1 Strains and loads in the four point bend specimens

Axial strain vs. applied displacement and load vs. displacement curves from the mechanical four point bend tests and the numerical (FEM) and analytical (plate theory) calculations are shown in Figure 5. It can be seen in this diagram that the experimental curves are very close to the analytical and numerical curves.

There is a very small difference between the curves obtained from plate theory and from the FEM model. This observation is quite important. The FEM analysis assumed the presence of specimen sliding with respect to the pins. However, this effect was not considered in the analytical calculations. Since the difference in the data from these two approaches is very small this indicates that the effect of specimen sliding on the strain and load values is essentially insignificant for the assumed applied displacements (less than 1mm). It was also found that the effect of the friction coefficient between the pins and the specimen did not affect the numerical strain and load results. Therefore, it can be concluded from the above observations that the calculations of axial strains and loads for the four point bend specimens can be performed analytically, using plate theory, without considering the specimen/pins interaction and provided that the applied displacements are

small. Under larger applied displacements this effect might be significant with the specimen exhibiting large geometrical and material non-linearities.

5.2. Results from the XRD measurements

Examples of the $\sin^2(\psi)$ plots for three different values of axial strain are shown in Figures 6 (a - f). The instant conclusion one can draw after examining these figures is that not all experimental points, for a given axial strain ϵ and the angle ϕ , lie exactly on straight lines. For $\epsilon = 3100 \times 10^{-6}$ (Figures 6.e and 6.f) the deviation from linearity is quite small as indicated by the value of the correlation coefficient R^2 , that is in this case equal to 0.999, but for other values of ϵ the scatter is significantly higher. For $\epsilon = 1500 \times 10^{-6}$, $\phi = 90^\circ$ (Figure 6.d) the scatter is quite large with the correlation coefficient R^2 equal to 0.845. The amount of scatter was not related to the magnitude of the applied strain. If curvature in the $\sin^2(\psi)$ plots is present it may be caused by the existence of non-diagonal components of the strain and stress tensors. It was assumed that the specimen's coordinate system was the same as the principal coordinate system for all inclusions, however the distribution of the inclusions is not uniform and not all inclusions are exactly spherical, so this might generate the non-diagonal components of both the strain and stress tensors. In other words, the principal coordinate system might change from one inclusion to another, due to the changing shape and distribution of inclusions.

The strain components ϵ_{11} , ϵ_{22} and ϵ_{33} inside the Al inclusions determined by the XRD measurements as a function of axial strain measured by a strain gage placed on the top surface of the specimen are shown in Figures 7a. The data presented in Figure 7a represent the average values from several measurements conducted for different axial applied strains for two X-ray conditions ($\phi = 0^\circ$ and $\phi = 90^\circ$). All the strain data obtained from the XRD measurements are presented in Table 1. The stress components inside the Al inclusions determined from the average strains in Figure 7a are shown in Figure 7b as a function of axial strains. Both the strain and stress data in Figures 7a and 7b are approximated by linear least-square fits. The X-ray strains and stresses in the Al

inclusions as a function of axial strain presented in Table 1 are compared with the previously published data in Ref. 1 from several other specimens tested without bending (denoted by * in Table 1). It is apparent that there is a significant amount of scatter in the results for the applied strain equal to zero (no bending). The stress components σ_{11} vary from 38 MPa to 60 MPa, whereas the ϵ_{11} components inside the inclusions vary from $367 \cdot 10^{-6}$ to $634 \cdot 10^{-6}$. Similar scatter can also be noticed in the case of the other strain and stress components. Despite the noticeable scatter there is an apparent trend in the data; the magnitudes of the stress and strain components increase linearly as a function of axial strain, with the strain ϵ_{22} and the stress σ_{33} being essentially unaffected by the applied strain.

5.3 Numerical strains and stresses inside Al inclusions as a function of bending

The numerically determined strains and stresses inside the Al particles as a function of applied axial strain (from bending) measured by the strain gage are shown in Figures 8a and 8b, respectively. The numerical values in these two figures are compared with the experimental data from the XRD measurements already shown in Figures 7a,b. Only the linear fits for the strains and stress values in Figures 7a and 7b are presented in Figures 8a and 8b for comparison with the calculated data. The calculations of the residual stresses and strains in the particles (without bending) were performed using the procedure described in Ref. [1]. The interlaminar model of the inclusions was used and the analysis was visco-elastic. The stresses and strains in the inclusions as a function of bending were also determined from the interlaminar model however the composite was assumed to be linear elastic.

It can be observed that the interlaminar model predicts quite well the ϵ_{11} and ϵ_{22} strain components. Most importantly, the slopes of the experimental and numerical strain curves are almost the same for the ϵ_{11} , ϵ_{22} and ϵ_{33} strain components. However, the magnitudes of the experimental values of ϵ_{33} inside the Al particles differ significantly from the numerical predictions despite the fact that the slopes of the ϵ_{33} vs. axial strain (from bending) curves are similar. Similar observations can be made when analyzing the

stress data presented in Figure 8b. In this case the experimental and numerical σ_{11} , σ_{22} and σ_{33} stress components exhibit very similar slopes as a function of axial applied strain. However, the actual values of σ_{11} and σ_{22} from the XRD measurements are slightly different from the model for various applied strains (Figure 8a). For σ_{33} the difference is especially high.

To explain the differences between the strain and stress components inside the Al particles determined by the XRD measurements and from the numerical predictions the assumptions made in the calculations must be discussed. The numerical models of both the residual thermal strains and the strains caused by bending inside the Al inclusions assume that:

- (i) The distribution of the Al inclusions between the first and second ply is constant (see Figure 9a) and is the same in each specimen subjected to the XRD tests.
- (ii) All inclusions are interlaminar in nature without any inclusion penetrating into the unidirectional plies on both sides of the interlaminar region (Figure 9a).
- (iii) All particles are spherical with perfect bonding between the particles and the polymer matrix.
- (iv) The interfaces between the unidirectional plies are parallel with a constant thickness of polymer resin between the plies (Figure 9a).

It has been shown in Ref. 1 that the actual particle distributions and the composite architecture differ significantly from the assumptions made in the numerical analyses. In particular, in the numerical model the volume fraction of Al inclusions was assumed to be 40%. However, it has been shown in Ref. [1] that the actual distributions of Al particles in several composite specimens can not only noticeably vary from one specimen to another, but also inside each specimen. The particles were found to be concentrated in disc-shaped clusters positioned between the first and second ply (see Figure 9b).

Moreover, the average particle concentration in a cluster can significantly vary from cluster to cluster. After analyzing the particle distributions by SEM in several specimens, the average volume fraction of Al inclusions was found to be $40\pm7\%$ [1]. The scatter in the distribution of the particles was not considered in the numerical analysis presented in this work. All calculations, with and without bending, were performed assuming 40% volume fraction of Al inclusions.

Despite the fact that a vast majority of the Al inclusions were interlaminar in nature a considerable number of inclusions were found to be intralaminar [1]. This effect has been considered in Ref. 1 by modeling Al inclusions distributed either between the plies (interlaminar inclusions) or in the polymer matrix between the graphite fibers in the first and second ply (intralaminar inclusions). However, it was concluded in Ref. 1 that the interlaminar model of the inclusions is a much better representation of the actual conditions. Furthermore, the thickness of the interlaminar region in the tested specimens is not constant and can vary significantly not only from specimen to specimen but also within each specimen. In the computation, the thickness of the polymer resin between the plies was assumed to be 50 μm .

The significant differences between the assumed and actual conditions regarding the particle distributions and composite architecture are responsible for the differences in the magnitudes of stresses and strains in the Al particles obtained from the model and from the XRD tests. If the interlaminar model is considered with the particles embedded between the unidirectional plies, the residual stresses in the Al inclusions in the absence of bending are: $\sigma_{11} = 49.4 \text{ MPa}$, $\sigma_{22} = 25.4 \text{ MPa}$ and $\sigma_{33} = -21.8 \text{ MPa}$ for the volume fraction of inclusions equal to 40% and the polymer layer thickness equal to 50 μm . These stress values are shown in Figure 8b for zero axial strain.

The interlaminar model of the embedded inclusions based on laminated plate theory and the Eshelby model for multiple inclusions assumed that the inclusions were subjected to plane stress conditions in the polymer layer between the two unidirectional plies. This will be true if the thickness of the polymer layer with the embedded inclusions is

constant. However, if the thickness of the layer changes in a composite specimen then the state of stress in the polymer layer is modified from plane stress to a three-dimensional state of stress [1]. This is the reason why such large differences between the stresses and strains in the particles from the model and from the X-ray tests were observed, in particular, with respect to the stress and strain component through the thickness. It is clear that laminated plate theory cannot be used to predict the actual stresses and strains in the inclusions, especially through the specimen thickness. This effect can be clearly seen in Figures 8a and 8b not only in the specimens subjected to residual stresses (for axial strain equal to zero) but also to the combined effect of residual stresses and bending.

The slopes of the strains and stresses inside the inclusions versus axial strains were almost constant where the specimens were subjected to small bending moments. The same was observed in the experimentally determined load/strain and load/displacement data. Under larger applied displacements the slopes will change since the specimens will undergo large geometrical deformations and the inclusions can change their mechanical properties [22].

5. Conclusions

The recently suggested methodology in Ref. 1 for the evaluation of residual strains and stresses inside crystalline particles embedded in unidirectional polymer matrix composites has been further verified by performing additional X-ray diffraction measurements of internal strains and stresses inside Al inclusions embedded in unidirectional graphite/PMR-15 composite specimens subjected to four point bending conditions. The X-ray strains in the particles have been found to be linearly dependent on the applied axial strain in the specimens caused by four-point bending. The magnitudes of the total strains ϵ_{11} and ϵ_{33} in the particles increase linearly with increasing applied strain, however, the effect of bending on the ϵ_{22} strain component inside the inclusions has been found to be negligible. The change in the strain components ϵ_{11} and ϵ_{22} inside the Al inclusions as a function of bending can be quite accurately predicted using laminate theory with the interlaminar distribution of the particles in conjunction with the

application of the Eshelby method of multiple inclusions. The ε_{33} strain component inside the inclusions differs significantly however from the numerical predictions. Very similar observations have been made with respect to the stress components inside the inclusions.

References

1. B. Benedikt, M Kumosa, P.K. Predecki, L. Kumosa, M. G. Castelli and J. K. Sutter, An Analysis of Residual Thermal Stresses in a Unidirectional Graphite/PMR-15 Composite Based on the X-ray Diffraction Measurements, *Composites Science and Technology* (2001) in press.
2. N. J. Rendler and I. Vigness, Hole-drilling Strain-gage Method of Measuring Residual Stresses, *Experimental Mechanics*, p. 577-586, 1966
3. H. E. Gascoigne, Residual Surface Stresses in Laminated Cross-ply Fiber-epoxy Composite Materials, *Experimental Mechanics*, vol. 34, p. 27-36, 1994
4. R. Y. Kim, H. T. Hahn, Effect of Curing Stress on the First Ply-failure in Composite Laminates, *Journal of Composite Materials*, vol. 13, p. 2-16, 1979
5. H. Fukuda, K. Takahashi and S. Toda, Thermal deformation of Anti-symmetric Laminates at Cure, *Proc. ICCM-10*, vol. 3, p. 141-148, 1995
6. P. G. Ifju, X. Niu, B. C. Kilday, S. C. Liu and S. M. Ettinger, Residual Stress Measurement in Composite Using the Cure-referencing Method, *Experimental Mechanics*, vol. 40, p. 22-30, 2000
7. G. Jeronimidis and A. T. Parkyn, Residual Stress in Carbon Fiber-Thermoplastic Matrix Laminates, *Journal of Composite Materials*, vol. 22, p. 401- 415, 1988

8. T. M. Wang and M. Daniel, Thermoviscoelastic Analysis of Residual Stresses and Warpage in Composite Laminates, *Journal of Composite Materials*, vol. 26, p. 883-899, 1992
9. S. R. White and Y. K. Kim, Process-Induced Residual Stress Analysis of AS4/3501-6 Composite Material, *Mechanics of Composite Materials and Structures.*, vol. 5, p.153-186, 1998
10. P. Predecki and C. S. Barrett, Stress Measurement in Graphite/Epoxy Composites by X-ray Diffraction from Fillers, *J. Comp. Mat.*, vol. 13, p. 61-71, 1979
11. P. Predecki, C. S. Barrett, Residual Stresses in Resin Matrix Composites, In E. Kula, editor, *28th Sagamore Army Materials Research Conference*, p. 409-424, Lake Placid, July 13-17 1981
12. C. S. Barrett and P. Predecki, Stress Measurements in Graphite/Epoxy Uniaxial Composites by X-rays, *Polymer Composites*, vol. 1, p. 2-6, 1980
13. D. Dragoi, Residual Stress Analysis of Graphite/Polyimide Composites Using the Concept of Metallic Inclusions, Ph.D. thesis, Faculty of Natural Science, Mathematics and Engineering, University of Denver, USA, 1999
14. M. Kumosa, P. K. Predecki, G. Odegard, K. Searles, B. Benedikt, D. Armentrout, L. Kumosa and M. Gentz, Analyses of Failure Mechanisms and Residual Stresses in Unidirectional and Woven Graphite/PMr-15 Composites Subjected to Shear Dominated Biaxial Loads, in the Proc. of the High Temple Workshop XXI, 12-15 February 2001, Clearwater Beach, Florida, pp. Z1- Z15.
15. I. C. Noyan and J. B. Cohen, Residual Stress. Measurement by Diffraction and Interpretation. Springer-Verlag, New York, 1987, p. 119.

16. J. N. Reddy, Mechanics of Laminated Composite Plates. Theory and Analyses, CRC Press, 1997
17. G. Odegard and M. Kumosa, Elastic-Plastic and Failure Properties of a Unidirectional Carbon/PMR-15 Composite at Room and Elevated Temperatures, *Composites Science and Technology*, vol. 60, p. 2979-2988, 2000.
18. G. D. Roberts, D. C. Malarik and J. O. Robaidek Viscoelastic Properties of Addition-Cured Polyimides Used in High Temperature Polymer Matrix Composites, Composites Design, Manufacturing, and Applications; *Proceedings of the Eight International Conference on Composite Materials*, S. W. Tsai and G. S. Springer, Eds., Society for Advanced Materials and Process Engineering, Covina, CA 1991, p. 12-H-1 to 12-H-10
19. J. D. Eshelby, The Determination of the Elastic Field of an Ellipsoidal inclusion, and Related Problems, *Proc. R. Soc. London*, vol. A241, p. 376-396, 1957
20. T. Mura, *Micromechanics of Defects in Solids*, 2nd edition, Martinus Nijhoff Publishers, Dordrecht, 1987
21. T. Mori and K. Tanaka, Average Stress in Matrix and Average Elastic Energy of Materials with Misfitting Inclusions, *Acta Metall.*, vol. 21, p. 571-574, 1973
22. B. Benedikt, M. Kumosa, P. Predecki, L. Kumosa, D. Armentrout and J. K. Sutter, The Effect of Large Bending Deformations on the Strains and Stresses in Metallic Inclusions Embedded in Graphite/PMR-15 Composites, to be published.

Acknowledgments

This research has been supported by the Air Force Office of Scientific Research and NASA Glenn Research Center under grants F49620-1-0426 (AFOSR) and F49620-00-1-0159 (AFOSR and NASA).

Figure Captions

Table 1. X-ray diffraction data as a function of applied strain.

Figure 1 Embedded Al inclusions: (a) single Al inclusion and (b) distribution of Al inclusions between the first and second plies.

Figure 2. X-ray four point bend tests; (a) four point bent fixture mounted on the Simens D-500 goniometer (b) specimen configuration inside the fixture.

Figure 3. Definition of the angles φ and ψ and the specimen coordinates.

Figure 4. Three -dimensional finite element model of the four point bend test.

Figure 5. Axial strains and forces as a function of applied displacement from the mechanical four point bend test as well as analytical and numerical (FEM) predictions.

Figure 6. Examples of plots of $\epsilon_{\varphi\psi}$ as a function of $\sin^2\psi$ for three different values of axial strain; (a) $\epsilon = 900 \mu e$, $\varphi = 0^\circ$, (b) $\epsilon = 900 \mu e$, $\varphi = 90^\circ$, (c) $\epsilon = 1500 \mu e$, $\varphi = 0^\circ$, (d) $\epsilon = 1500 \mu e$, $\varphi = 90^\circ$, (e) $\epsilon = 3100 \mu e$, $\varphi = 0^\circ$, (f) $\epsilon = 3100 \mu e$, $\varphi = 90^\circ$.

Figure 7. X-ray strains and stresses inside Al inclusions as a function of axial strain ϵ_{11} ; (a) strains and (b) stresses.

Figure 8. Numerical and X-ray strains (a) and stresses (b) inside Al inclusions as a function of applied strain ϵ_{11} .

Figure 9. Assumed (a) and actual (b) composite architectures and particle distributions.

Applied strain [10 ⁻⁶]	Slope $\varphi=0$ [10 ⁻⁶]	Slope $\varphi=90$ [10 ⁻⁶]	ε_{11} (4 2 2) [10 ⁻⁶]	ε_{22} (4 2 2) [10 ⁻⁶]	ε_{33} (4 2 2) [10 ⁻⁶]	σ_{11} [MPa]	σ_{22} [MPa]	σ_{33} [MPa]
*0	830	272	565	7	-265	49	19	5
*0	956	438	634	116	-322	60	33	9.5
*0	640	480	367	207	-273	38	29	4
*0	780	490	514	224	-266	56	41	15
*0	730	340	483	93	-247	46	25	7
0	729	359	527	157	-202	57	38	19
600	925	334	678	87	-247	68	37	19
900	898	352	659	113	-239	68	39	20
900	866	352	607	93	-259	59	32	14
900	790	352	558	120	-232	57	34	15
1200	985	360	745	120	-240	78	45	26
1500	943	367	671	95	-272	66	36	16
2000	1012	412	717	117	-295	71	39	18
2500	1122	404	776	58	-346	71	33	12
2500	1171	404	827	60	-344	77	37	16
2500	1167	404	893	130	-274	93	53	32
2800	1160	555	800	195	-360	81	50	20 -
3100	1059	410	748	99	-311	72	38	17

* Reference [1]

Table 1

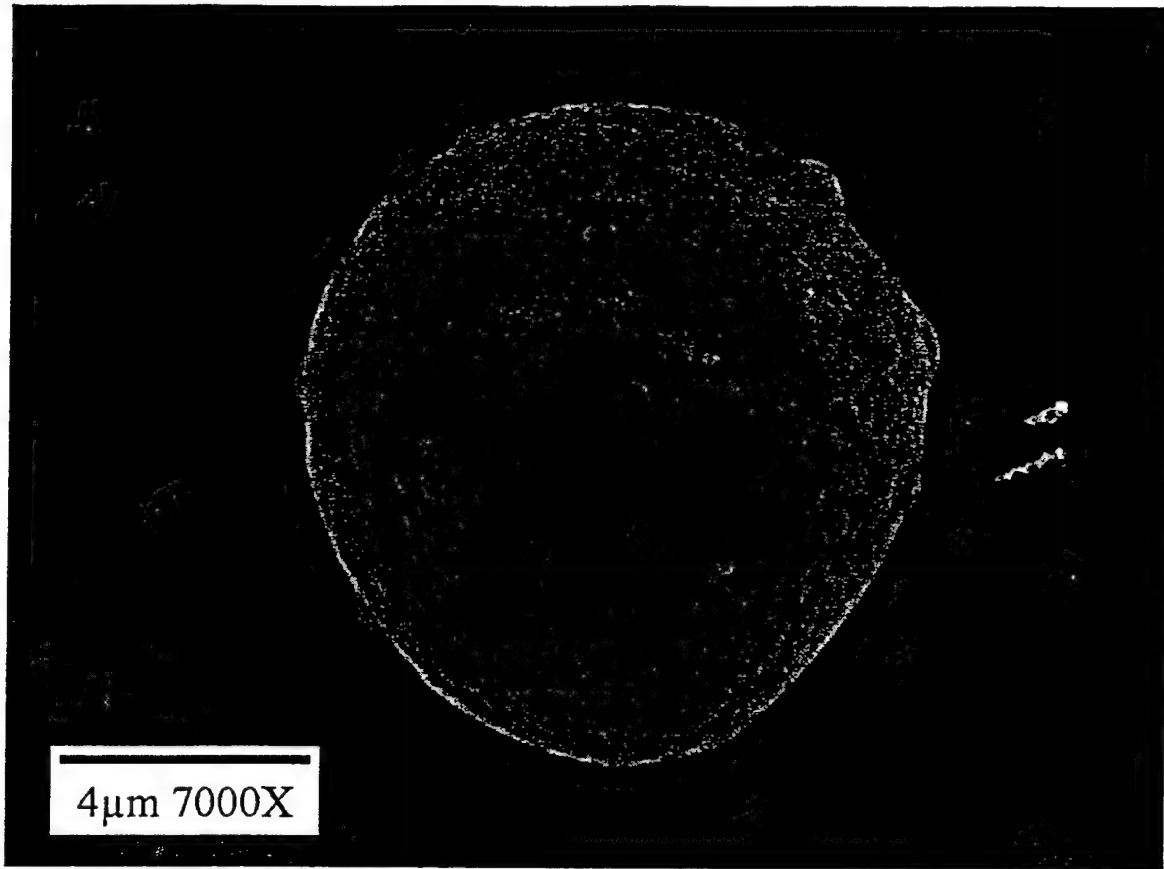


Figure 1a

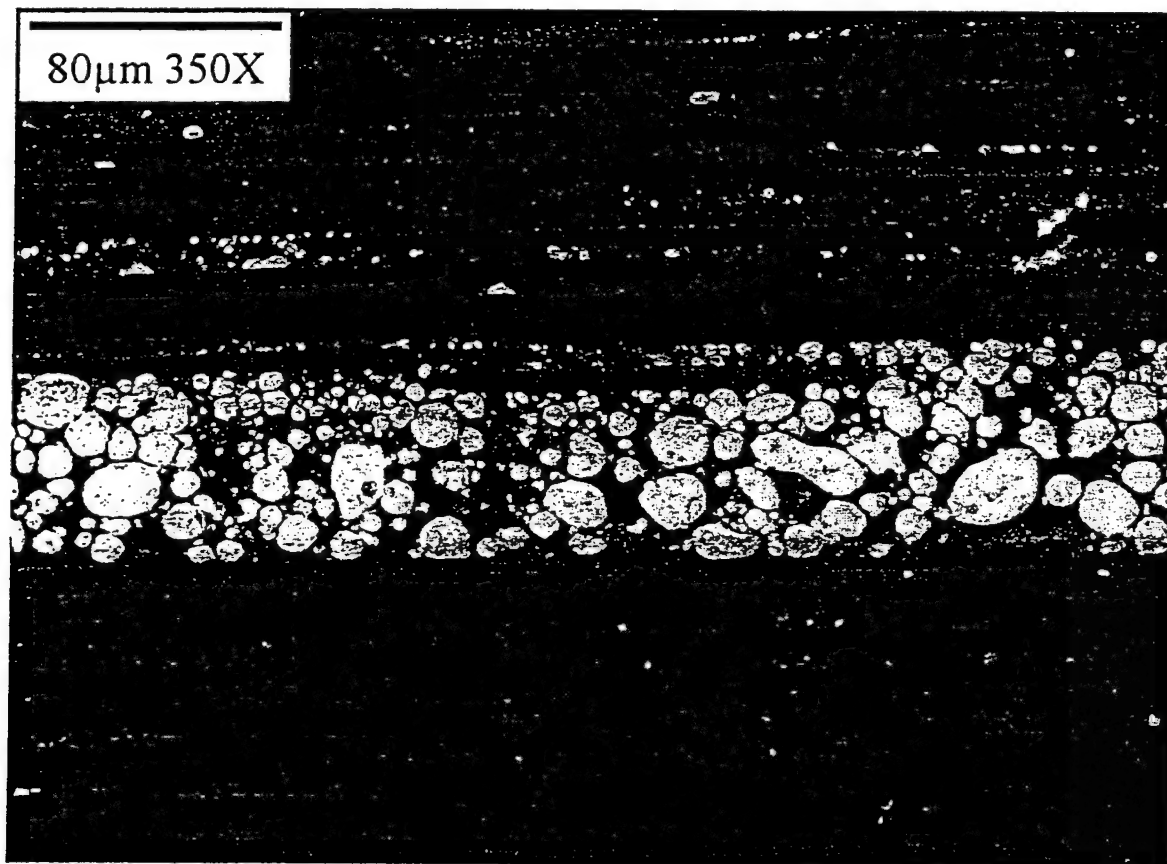


Figure 1b

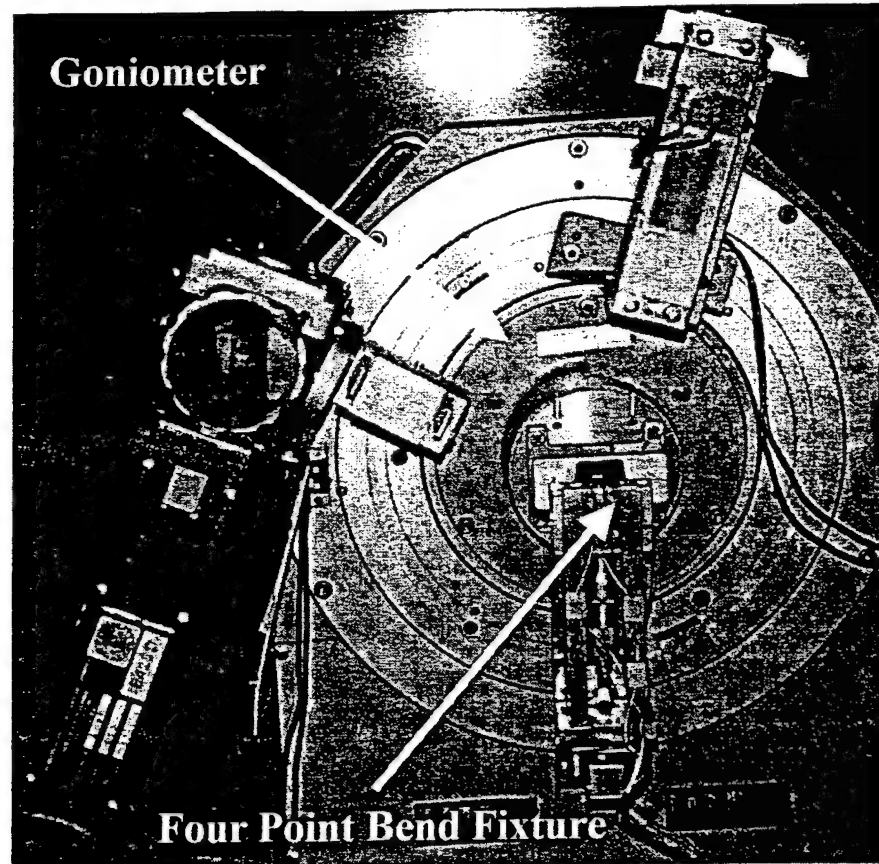


Figure 2a

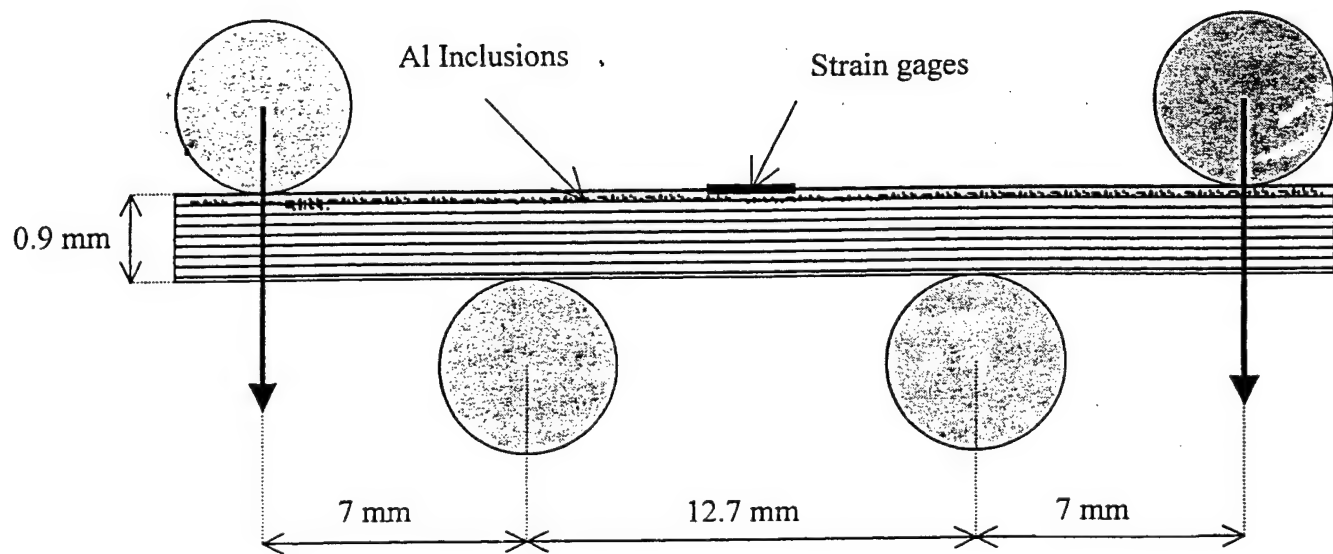


Figure 2b

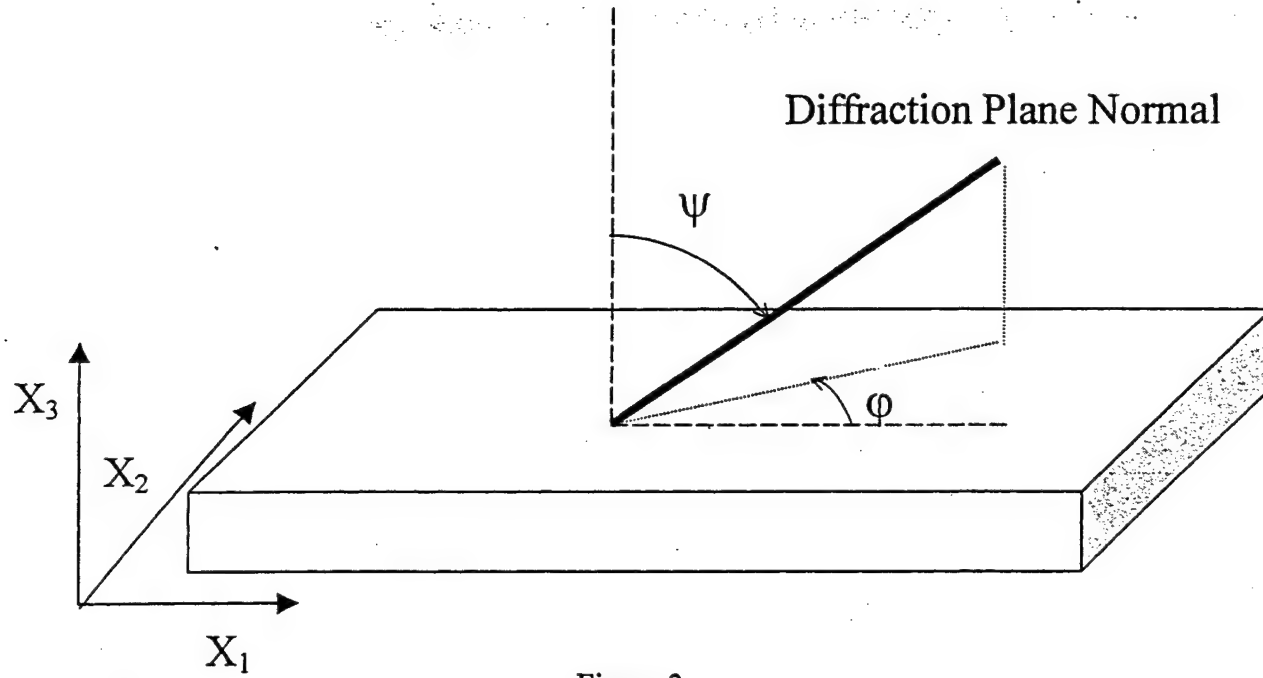


Figure 3

Applied Displacement

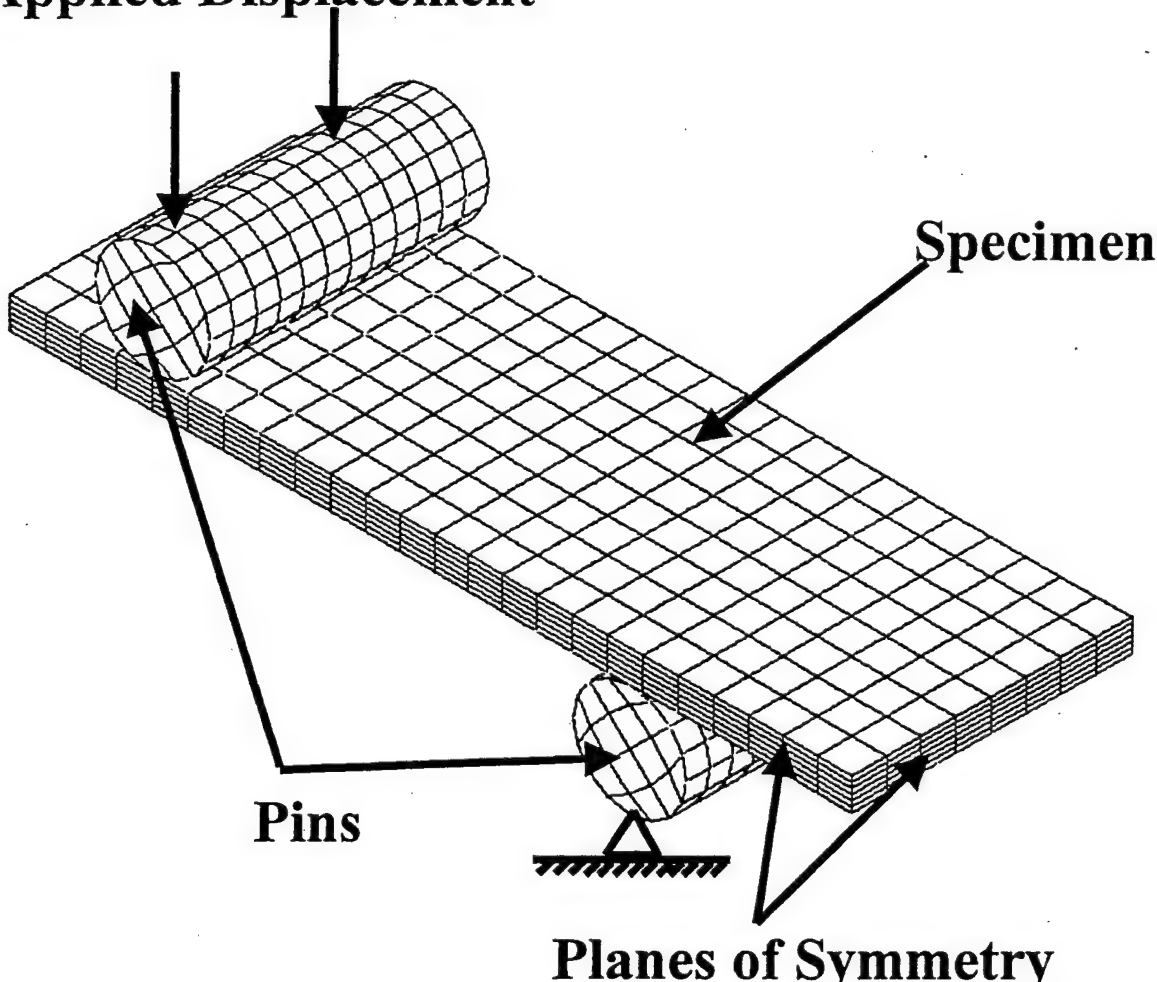


Figure 4

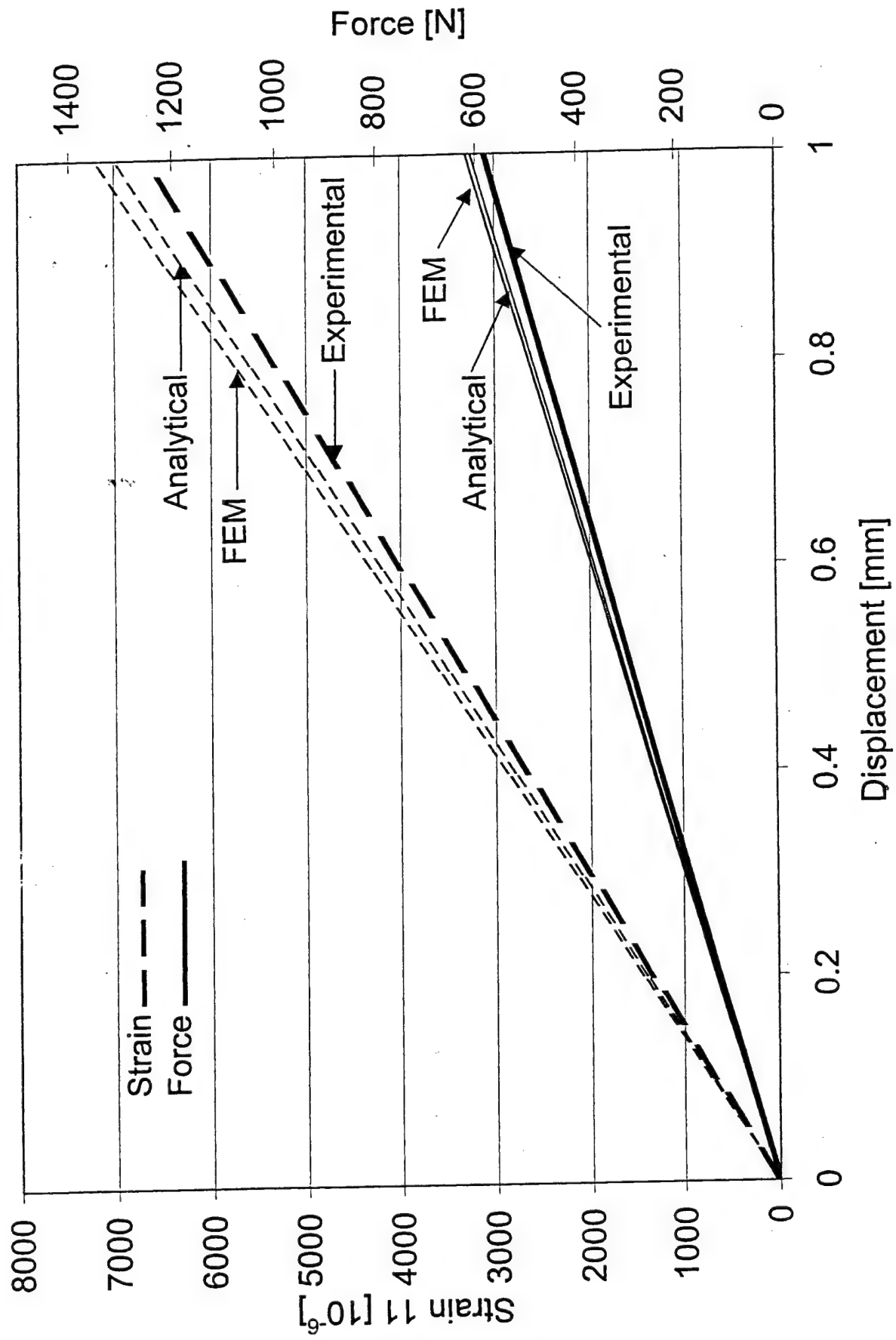


Figure 5

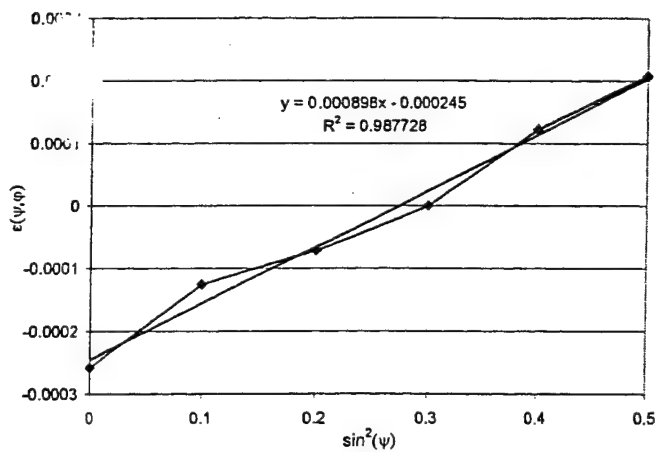


Figure 6a

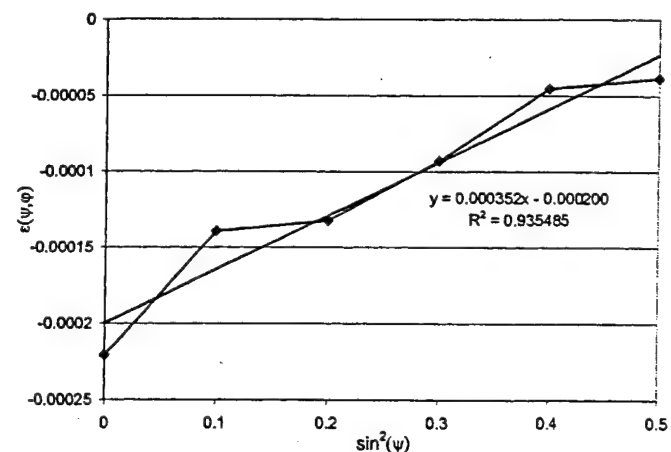


Figure 6b

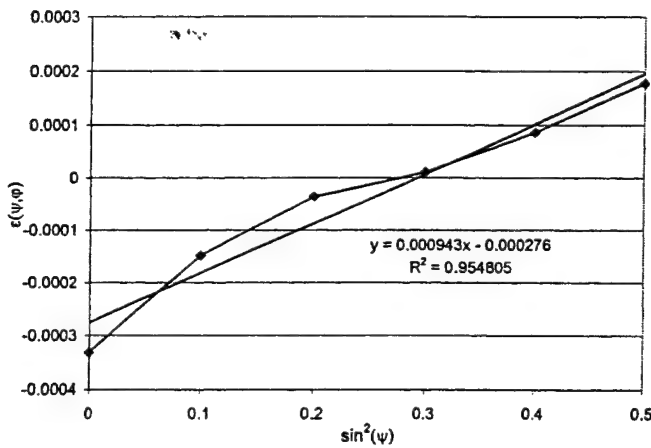


Figure 6c

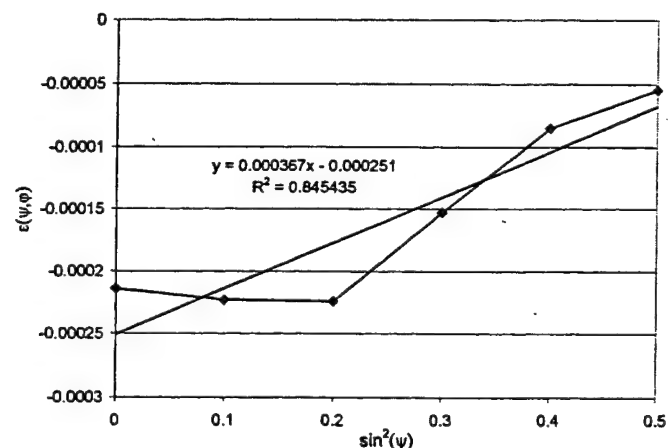


Figure 6d

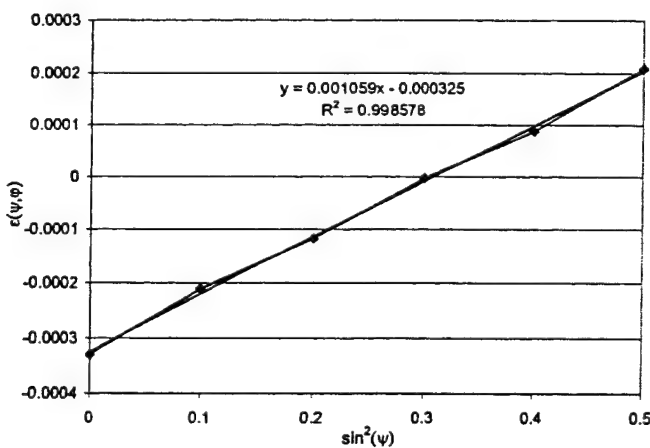


Figure 6e

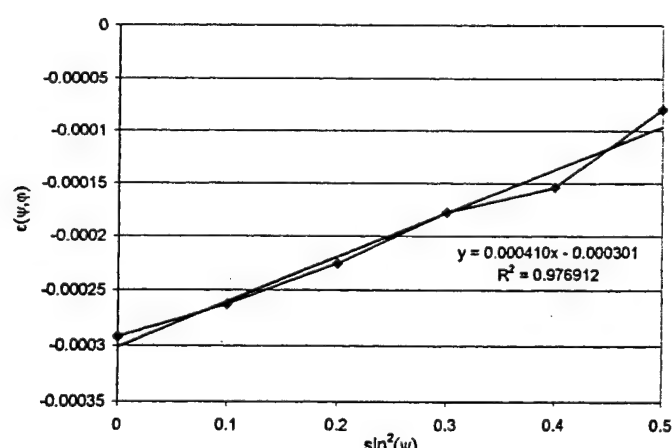


Figure 6f

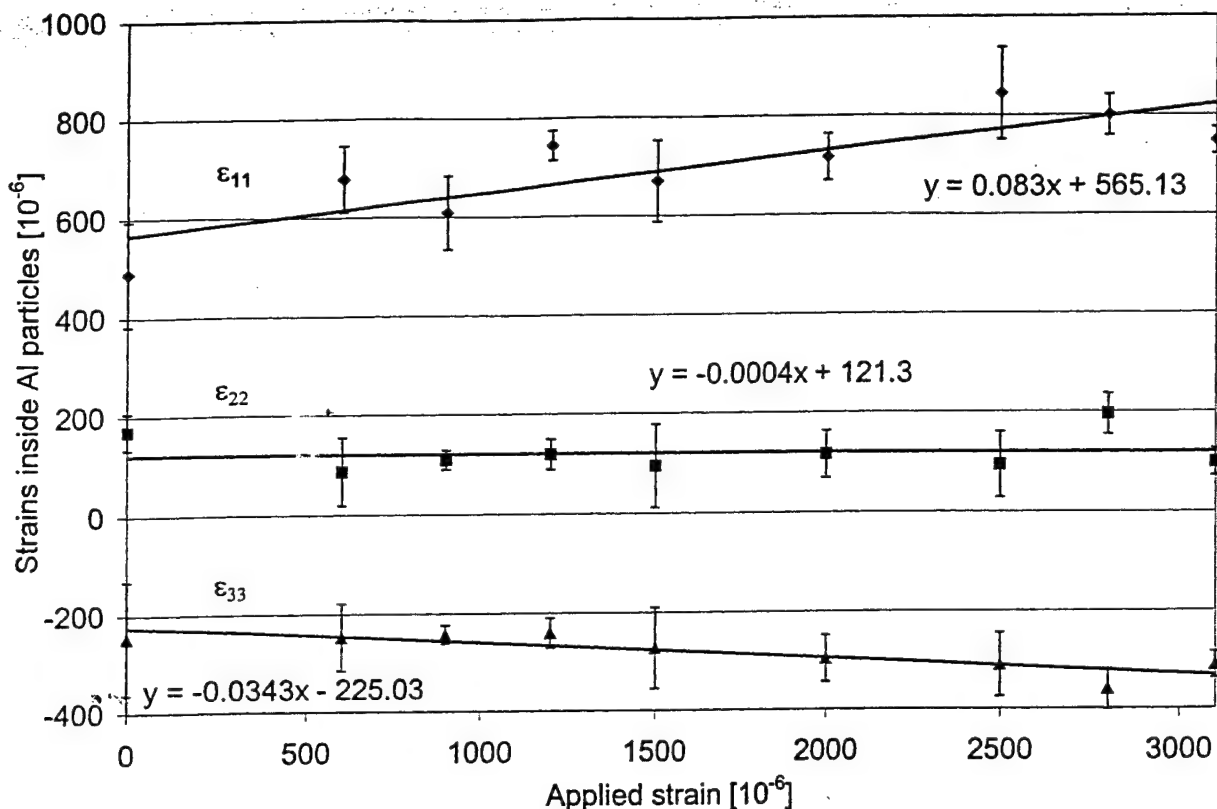


Figure 7a

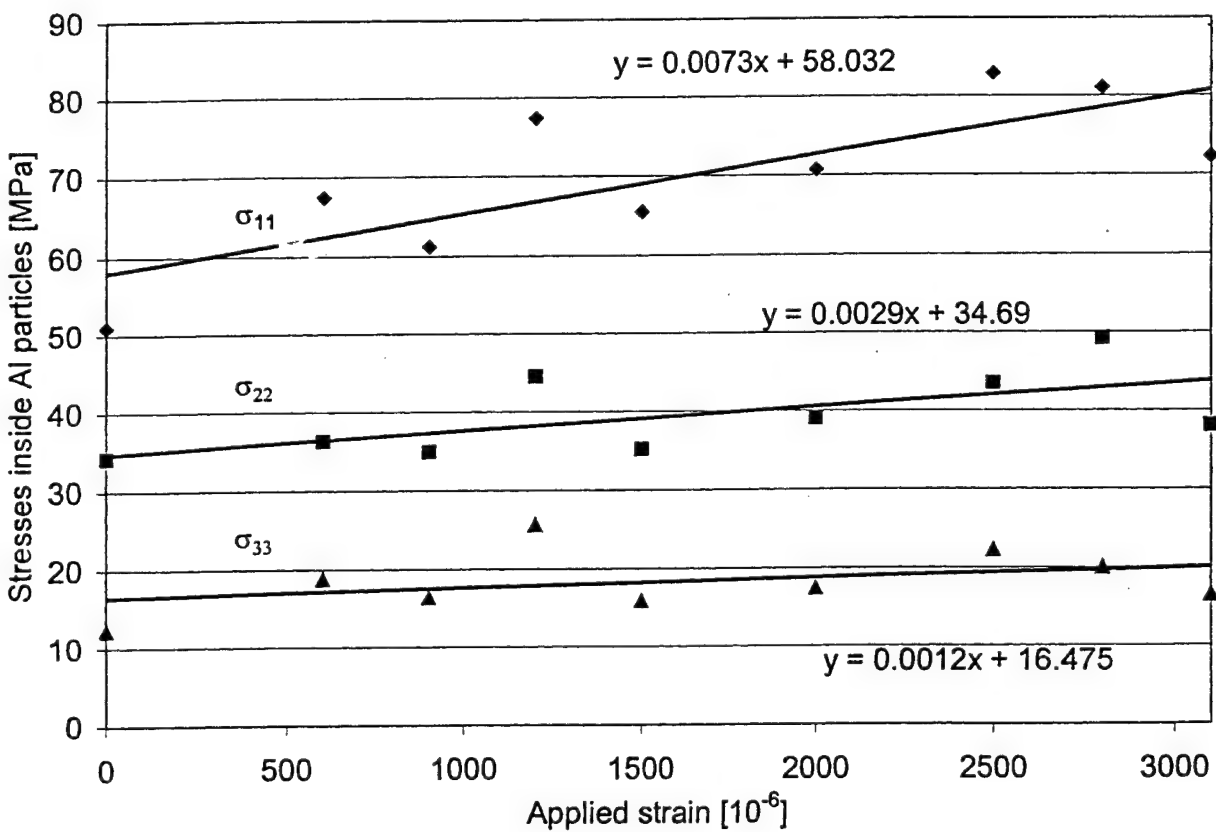


Figure 7b

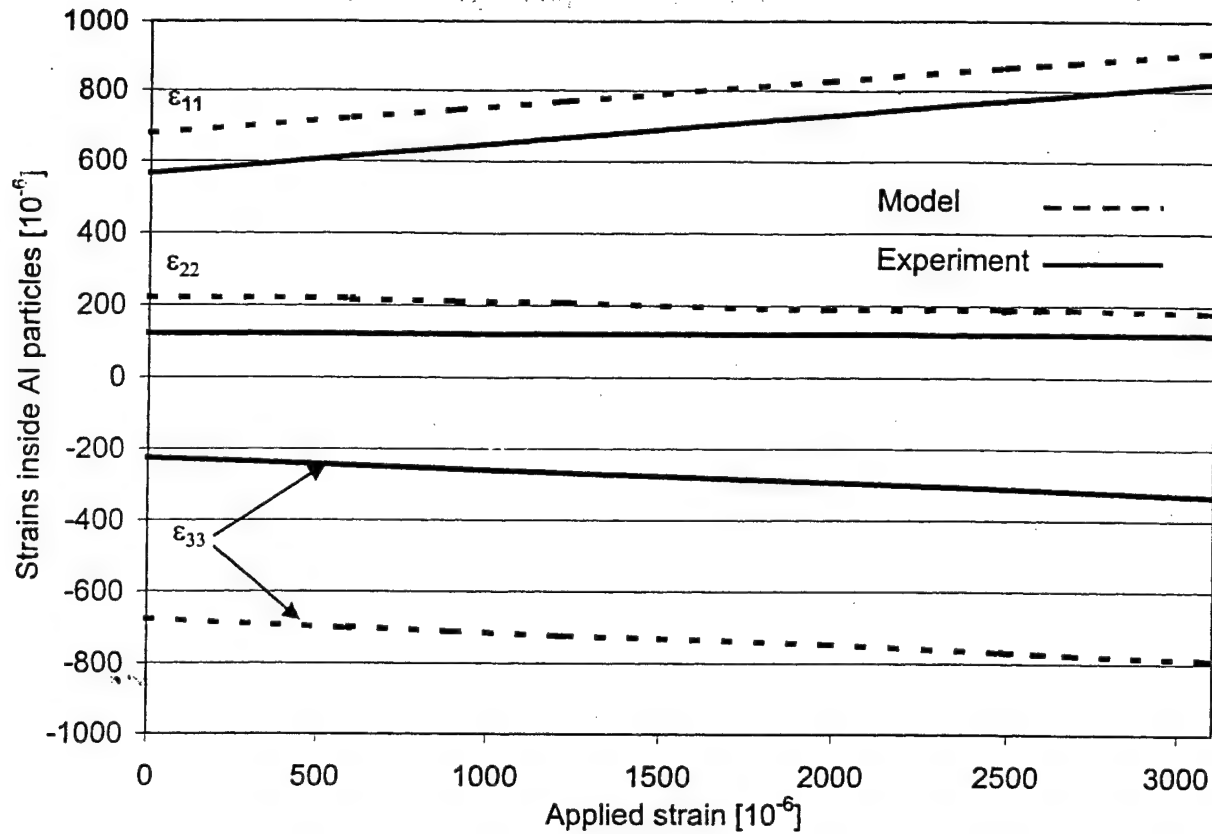


Figure 8a

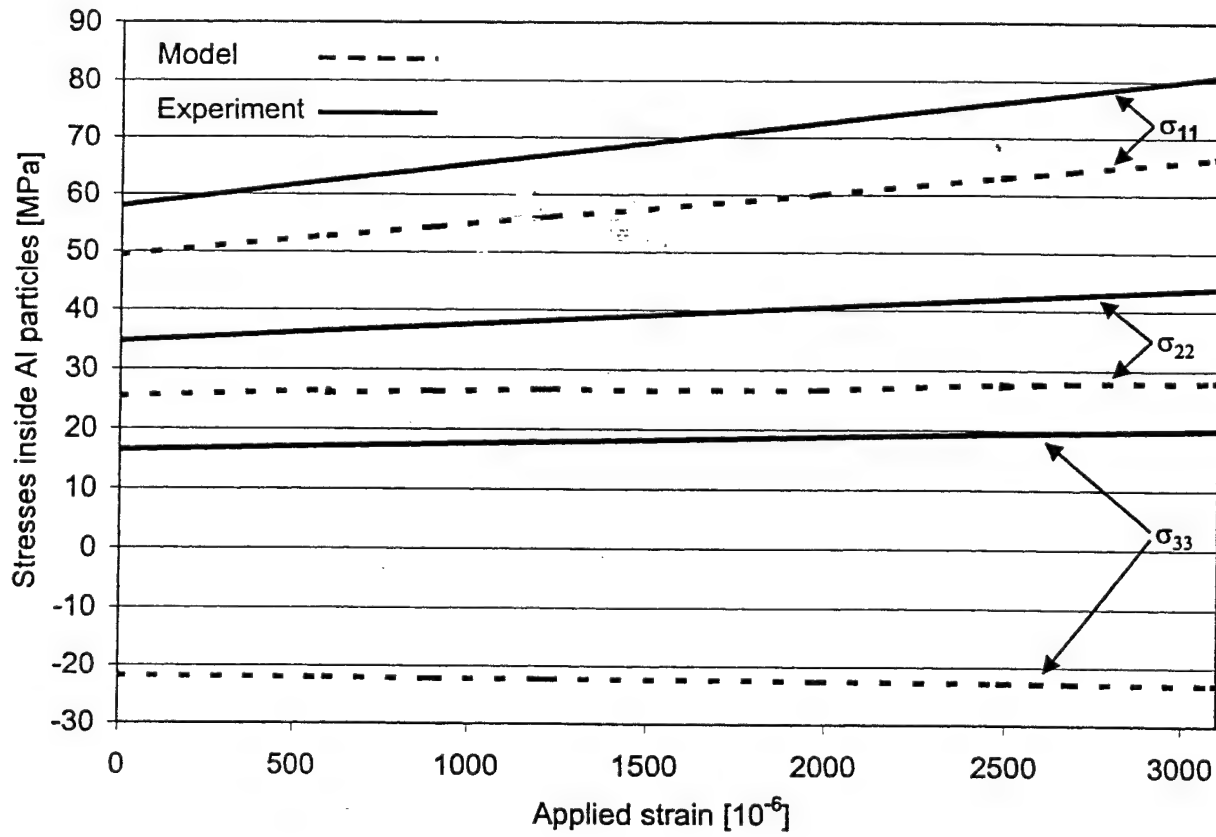


Figure 8b

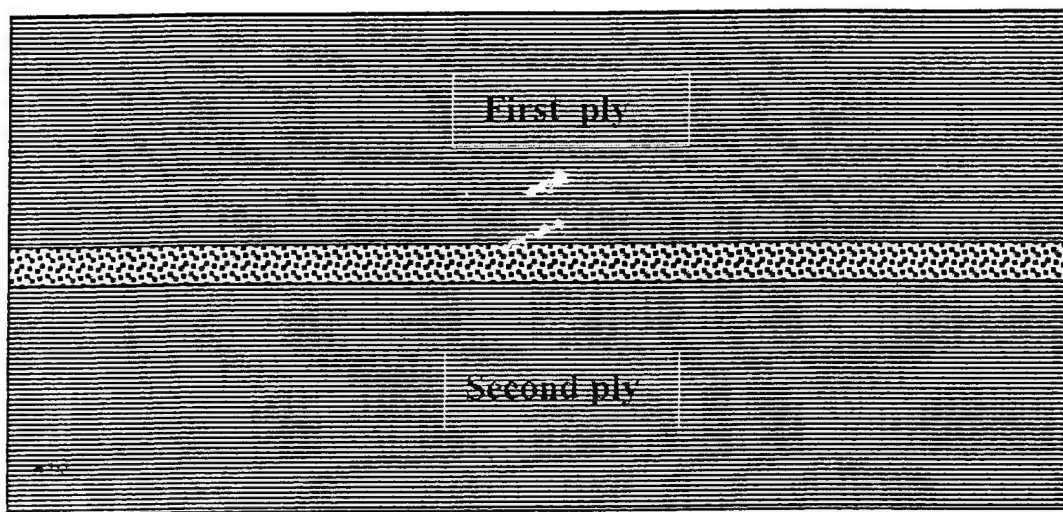


Figure 9a

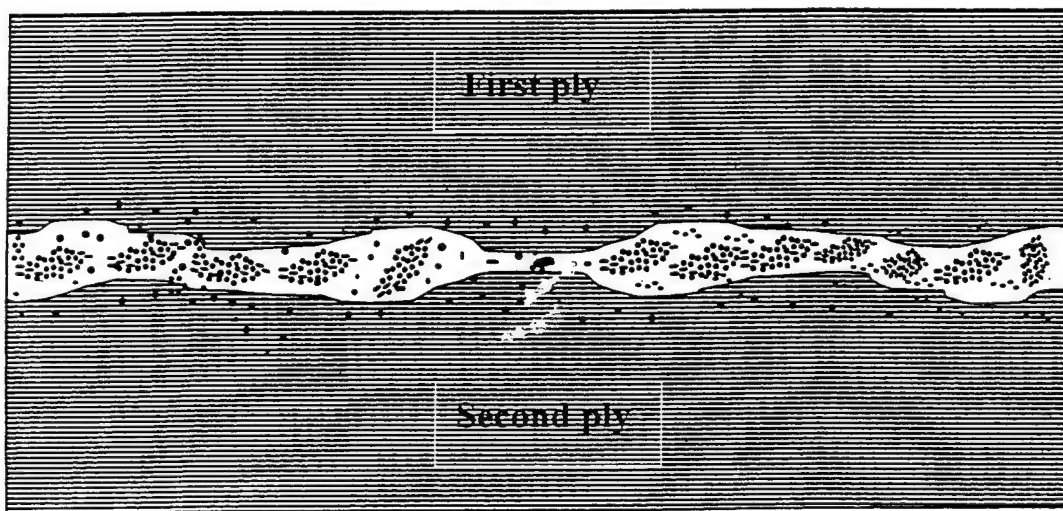


Figure 9b

Submitted for publication in Mechanics of Composite Materials and Structures

Determination of Interlaminar Residual Thermal Stresses in a Woven 8HS Graphite/PMR-15 Composite Using X-ray Diffraction Measurements

B. Benedikt, P. Rupnowski, L. Kumosa, J. K. Sutter* P.K. Predecki
and M. Kumosa

Center for Advanced Materials and Structures
Department of Engineering
University of Denver
2390 South York St., Denver, Colorado 80208

*NASA Glenn Research Center at Lewis Field
21000 Brookpark Rd.
Cleveland, OH 44135

Abstract

This work is a continuation of the research recently presented in Refs. 1 and 2 on the determination of residual thermal stresses in graphite/polyimide composites with and without externally applied bending loads. In the previous work [1,2] a combined experimental and numerical methodology for the determination of the residual stresses in unidirectional graphite/PMR-15 composites based on X-ray diffraction (XRD) measurements of residual strains in embedded aluminum (Al) and silver (Ag) inclusions has been presented. In this research, the previously developed approach has been applied to evaluate the residual thermal interlaminar stresses in an 8 harness satin (8HS) woven graphite/PMR-15 composite. First, residual thermal stresses have been measured by XRD in aluminum inclusions embedded between the first and second plies of a four ply 8HS woven graphite/PMR-15 composite. The measurements have been conducted with the composite specimens subjected to four point bending deformations. Secondly, visco-elastic computations of interlaminar residual stresses in the composite have been performed using classical laminated plate theory (CLPT) following the manufacturing procedure. Thirdly, the residual strains and stresses in the inclusions have been numerically predicted using the visco-elastic Eshelby model for multiple spherical inclusions. Finally, the interlaminar residual stresses in the composite have been

extracted from the XRD strains in the Al inclusions, again using the visco-elastic Eshelby model and subsequently compared with the residual stresses from the CLPT. It has been shown in this study that the residual interlaminar thermal stresses can be accurately determined not only in unidirectional graphite/polyimide systems as presented in Refs. 1 and 2 but also in woven graphite polymer matrix composites.

1. Introduction

Thermal residual stresses are generated in composite materials because of the mismatch of the coefficients of thermal expansion (CTE) between the reinforcements and the matrix. Because of its practical importance, the problem of developing, measuring and minimizing residual stresses has been addressed by many authors [1-11]. Predecki and Barrett [9-11] showed that it was possible to use the X-ray diffraction (XRD) method to measure the state of strain in aluminum, silver and niobium inclusions embedded in the polymer matrix of a graphite/epoxy composite system. However, they could not extract the actual residual stresses in the composite from the XRD strains and stresses in the embedded metallic inclusions. The problem of properly extracting the residual thermal stresses in unidirectional graphite/polymer composites from XRD strains in embedded silver and aluminum inclusions has been recently addressed and thoroughly discussed in Ref. 1. The methodology developed in Ref. 1 has been further verified by performing XRD measurements of residual strains in Al inclusions embedded in the polyimide matrix of a unidirectional graphite/PMR-15 composite subjected to four point bending conditions [2]. It was shown that the residual strains in the inclusions increased linearly with applied strain generated by a four point bend fixture used during the XRD tests. The experimentally determined strains in the inclusions agreed quite well with the numerical predictions based on the CLPT and the Eshelby model for multiple spherical inclusions.

In this research, the recently developed combined experimental and computational methodology for the determination of residual stresses in unidirectional polymer matrix composites was used to evaluate interlaminar residual stresses in an 8HS graphite/PMR-15 composite.

2. Materials Tested

2.1 Manufacturing process

A woven 8HS four ply graphite/polyimide composite plate (152x152 mm) with embedded aluminum inclusions between the first and second ply was manufactured at the NASA Glenn Research Center per the following specifications:

Graphite Fibers: T650-35, 3K 8HS cloth, UC309 size

Polyimide Matrix: PMR-15

Ply arrangement: warp aligned, four-ply with floating undulation

Cure: panels were vacuumed bagged in a press at 315 °C/1.38MPa

The plate was post cured in air in the following five steps:

Step 1. From room temperature to 246⁰ C in 100 min (no hold).

Step 2. From 246⁰ C to 288⁰ C in 150 min and hold at 288⁰ C for 300 min.

Step 3. Ramp to 315⁰ C in 100 min and hold at 315⁰ C for 600 min.

Step 4. Cool to 204⁰ C in 50 min (no hold).

Step 5. Cool to room temperature over 180 min.

After manufacturing, the plate was C-scanned at NASA GRC to evaluate its quality using through-transmission techniques with a Physical Acoustic Corp. Model UPKI-T equipped with a 5MHz transducer. Based on the C-scan analysis it was estimated that the volume fraction of voids in the plate was less than 2%.

The thickness of the plate was measured in twelve randomly selected locations. The average thickness of the plate was found to be 1.26 mm, ranging from 1.21 mm to 1.3 mm.

2.2 Acid digestion, thermal mechanical and gravimetric analyses

Acid digestion tests were performed at NASA to determine void and fiber contents in the composite following ASTM D2734-70 and ASTM D3171-76 standards, respectively. Three samples were taken from three different locations on the plate for the acid digestion tests. The samples were taken approximately 10 mm from the edges. The average resin content by weight, fiber volume and void content were 30.01%, 63.4% and less than 2%, respectively. Thermal mechanical and gravimetric analyses (TMA and TGA) were also performed using TA Instruments Models 2940 and 2950, respectively. The glass transition T_g and decomposition T_d temperatures of the composite were found to be 343 °C and 503 °C, respectively.

2.3 SEM analyses of inclusion distributions

Before the XRD measurements were performed, the distributions of the Al inclusions in the composite were determined using scanning electron microscopy in the following fashion. First, three small samples were taken from different locations in the as supplied composite plate. Then, the samples were mounted in a Buehler "Ultra-Mount" mounting kit and their cross sections were polished. The cross sections with well visible Al inclusions were imaged at 350x magnification. The images were acquired from the microscope using LPi hardware and the LPi software plug-in for NIH Image v1.62. Subsequently, the images were analyzed for inclusion distributions using the image software. This was accomplished by first cutting out a inclusion rich region regardless of individual inclusion location and small pockets of inclusion deficiency within these regions. The size of the cutout in pixels was then determined. This cutout was then subjected to the "Analyze Particles" function within the NIH Image software. This function provided the size in pixels of each individual inclusion within the cutout. To obtain a inclusion density, the total area of inclusions within a cutout was divided by the total area of the cutout and multiplied by 100%. The results from the inclusion area fraction analysis are presented in Table 1. It can be seen that the average area fraction of the inclusions determined from twenty regions in three samples is $46 \pm 7.4\%$.

Through the SEM observations, the area fraction of the Al inclusions was obtained and the distribution of the inclusions across the composite was evaluated. It was found that the inclusions were predominantly distributed in the interlaminar region between the first and second fabric plies of the composite (see Figure 1a,b). Some inclusions however migrated into the woven plies outside the polyimide layer during the manufacturing process. The shape of the inclusions was also investigated. It was found that the shape of the inclusions was almost spherical with an aspect ratio of 1.4 [1]. The average diameter of the inclusions was approximately 1.9 μm ranging from 0.4 to 33.4 μm [1].

Table 1. Area fraction of Al inclusions in %.

Location	Sample 1	Sample 2	Sample 3
1	42	52	52
2	54	41	56
3	38	41	45
4	40	57	38
5	42	54	50
6	43	57	48
7	-	36	35
Average	43 ± 6	48 ± 9	46 ± 8
Total average =	46	Standard deviation =	7.4

3. X-Ray Diffraction Measurements

The XRD measurements were performed on 50 \times 16 mm specimens cut using a Buehler diamond saw. Before testing, the specimens were lightly polished with 400-grit paper to obtain flat surfaces. Two types of XRD experiments were performed. In the first case, three specimens were tested without external loads. Each specimen was first placed on a quartz plate before it was put into a Siemens D-500 diffractometer with pseudo-parallel beam optics and a solid-state detector. In the second case, one specimen was mounted into a four-point bend fixture and subsequently placed into the diffractometer. In both cases, the specimen location was checked with a dial gage and micro flat accurate to 0.025 mm.

The definition of ϕ and ψ angles with respect to the specimen's coordinate system is shown in Figure 2. The XRD measurements were performed at $\phi = 0^\circ$ and 90° and ψ changing from 0° to 45° for each ϕ angle. As described in [1], in the specimen's coordinate system only the diagonal components of the strain tensor ε_{ij} were assumed to be different than zero, so the fundamental equation of x-ray strain determination [12] could be simplified to yield:

$$\varepsilon_{\phi=0,\psi} = \frac{d_{\phi=0,\psi} - d_0}{d_0} = (\varepsilon_{11} - \varepsilon_{33}) \sin^2 \psi + \varepsilon_{33} \quad (1a)$$

$$\varepsilon_{\phi=90,\psi} = \frac{d_{\phi=90,\psi} - d_0}{d_0} = (\varepsilon_{22} - \varepsilon_{33}) \sin^2 \psi + \varepsilon_{33} \quad (1b)$$

where d_0 denotes the lattice spacing of the aluminum (422) planes for stress free inclusions, and $d_{\phi,\psi}$ is the lattice spacing for the same set of crystallographic planes for embedded Al inclusions. The lattice spacing d_0 was measured on the Al powder used and was corrected to the same temperature as that at which the corresponding $d_{\phi,\psi}$ was measured using the literature value for the CTE for aluminum. Four examples of the $\varepsilon_{\phi\psi}$ vs. $\sin^2 \psi$ plots along with straight least-squares lines approximating the experimental data are presented in Figures 4(a-d). After the experiments had been carried out, it turned out that all $\varepsilon_{\phi\psi}$ vs. $\sin^2(\psi)$ plots were linear within experimental error. From the $\varepsilon_{\phi\psi}$ vs. $\sin^2 \psi$ plots all components of the strain tensor were determined: ε_{33} was taken to be the average between $\varepsilon_{\phi=0,\psi=0}$ and $\varepsilon_{\phi=90,\psi=0}$ measurements and both ε_{11} and ε_{22} were calculated by adding the obtained value of ε_{33} to the corresponding slope of a straight line as indicated by equations 1a-1b. In order to obtain the stress tensor, the so-called X-ray elastic constants for the 422 reflection were calculated by taking the mean of the Reuss and Voigt models [12], using the literature values for a single crystal of aluminum. These calculations yielded Young's modulus E and Poisson ratio ν values of 71 GPa, and 0.351, respectively. The stress tensor was subsequently calculated using Hooke's law.

Table 2. X-ray diffraction data as a function of axial strain.

Applied strain [10 ⁻⁶]	Slope $\phi = 0^\circ$ [10 ⁻⁶]	Slope $\phi = 90^\circ$ [10 ⁻⁶]	ϵ_{11} [10 ⁻⁶]	ϵ_{22} [10 ⁻⁶]	ϵ_{33} [10 ⁻⁶]	σ_{11} [MPa]	σ_{22} [MPa]	σ_{33} [MPa]
*0	1093	920	527	354	-566	47.2	38.1	-10.3
*0	785	986	391	592	-394	57	67.6	15.8
*0	741	831	473	563	-268	72.4	77.14	33
*0	941	874	652	585	-289	92.9	89.4	43.5
*0	791	937	401	547	-390	55.6	63.3	14
0	961	811	612	462	-349	77	69.2	26.5
600	1219	960	689	430	-530	72.8	59.2	8.7
600	877	960	407	490	-470	47.8	52.2	1.7
600	1034	960	484	410	-550	46.7	42.8	-7.6
900	1143	1021	557	435	-586	54.5	48.1	-5.5
1200	1210	935	628	353	-582	57.7	43.2	-5.9
1500	1223	1159	643	579	-580	73.5	70.2	9.3
2000	1337	1150	752	565	-585	84.8	75	14.6
2500	1455	1351	778	674	-677	88.6	83.4	12.4

*) data obtained without bending with the specimen placed on a quartz plate

All the data (slopes of $\epsilon_{\phi\psi}$ vs. $\sin^2(\psi)$ plots as well as residual strains and stresses inside the Al inclusions) from the XRD measurements performed on the specimens with and without four point bending are shown in Table 2. The experimentally determined residual strains and stresses in the inclusions shown in Table 2 will be subsequently compared with their numerical predictions in the sections below.

4. Calculations of Residual Strains and Stresses in the Composite and Al Inclusions

4.1 Material properties

In order to compute thermal residual stresses in the composite and the residual strains and stresses in the Al inclusions, certain physical properties of the composite and inclusions must be known a priori. In particular, the composite architecture (type of fabric, lay-up, volume fraction of graphite fibers, etc.), the stiffness properties of the fibers and the polyimide matrix as well as the CTEs of the fibers and matrix must be either experimentally determined or assumed. In the calculation of the residual stresses performed in this research the PMR-15 matrix of the composite was modeled as a viscoelastic material with its thermal expansion coefficient α depending upon temperature and its shear modulus G depending on both time and temperature following the experimental data presented in Ref.13 for the shear modulus and provided by NASA Glenn for the CTE. The Poisson's ratio of the resin was assumed to be constant. Both the G and CTE data were taken for the polyimide post cured in air with the post curing cycle exactly the same as the post curing cycle of the tested composite. The values of G and α were subsequently curve fitted to obtain $G(t)$ at a reference temperature ($T_{ref}=288^{\circ}\text{C}$) and the $\alpha(T)$ function. These functions are shown below.

$$G(t) = 10^{(\text{Exp}(0.16(-\text{Log}(t)+6.5)^{0.5})+7.5)} \quad (2a)$$

$$\alpha_v(T) = 10^{\text{Exp}(0.012(-T+348)^{0.48})-1.076} \quad (2b)$$

$$\alpha_h(T) = 10^{\text{Exp}(0.41(-T+348)^{0.28})-4.3} \quad (2c)$$

$$\alpha(T) = 3 \cdot 10^{-12} \cdot (104 + T) \cdot (127160 - 548 \cdot T + T^2) \quad (3)$$

The vertical, $a_v(T)$, and horizontal, $a_h(T)$, shift functions were estimated from the data presented in Ref. 13. The horizontal shift function was used in the definition of reduced time $\xi(t)$:

$$\xi(t) = \int_0^t \frac{dt'}{a_h[T(t')]} \quad (4)$$

From the horizontal and vertical shift functions given by equations 2b and 2c, the shear modulus G of the polyimide can be determined at any given time (ranging from 0 to $10^{6.5}$ seconds) and temperature (ranging from room temperature to 348°C).

The thermal expansion coefficients of the fibers were taken as $\alpha_{Lf} = -0.5 \times 10^{-6} \text{ K}^{-1}$ (longitudinal), $\alpha_{Tf} = 10 \times 10^{-6} \text{ K}^{-1}$ (transverse). The elastic properties of the graphite fibers were assumed to be $E_{Lf} = 241 \text{ GPa}$ (longitudinal Young's modulus), $E_{Tf} = 20 \text{ GPa}$ (transverse Young's modulus), $K_f = 20 \text{ GPa}$ (bulk modulus), $v_{Lf} = 0.2$ (longitudinal Poisson ratio), $v_{Tf} = 0.4$ (transverse Poisson ratio), $G_{Lf} = 27 \text{ GPa}$ (longitudinal shear modulus), $G_{Tf} = 11 \text{ GPa}$ (transverse shear modulus). The physical properties of the graphite fibers and the polyimide resin used in this research were also used in the computations shown in Refs. 1 and 2. Only the composite architectures differed between the two studies.

4.2 Interlaminar Residual Stresses in the 8HS composite

For the calculation of the interlaminar residual stresses in a woven laminate using visco-elastic CLPT the stiffness properties and CTEs of woven plies must be determined as a function of time and temperature. Having the properties of the fibers and resin, models based on a repeating unit cell may be employed to evaluate the in-plane stiffness properties and the CTE's of a woven fabric layer.

The models proposed by Ishikawa and Chou [14-16], namely the crimp and bridging models were considered to evaluate the thermal and the visco-elastic properties of a

woven ply. The crimp model assumes a continuous shape of warp yarns and constant stress in the load direction. Despite the fact that the crimp model is essentially one-dimensional, it is well suited for plain-woven structures [16]. However, for 4 and 8 harness satin composite structures, Ishikawa and Chou [14-16] recommend the bridging model, which is a two-dimensional extension of the crimp model. A more accurate non-uniform stress/strain distribution is achieved in the bridging model and for this reason this model was used in the present analysis.

Before any computations can be performed, the geometrical parameters of a woven composite must be determined. The thickness of the composite plates used in the XRD measurements, consisting of four layers of woven fabric and three layers of neat resin was measured to be 1.26 mm. Therefore, the thickness ht of one fabric layer was calculated to be 0.2775 [mm], since the average thickness of the polymer layers between the woven plies was approximately 0.05 mm, as determined by SEM. The other geometrical data were taken from Ref. 17. Searles et al. [17], after performing SEM examinations of the same fabric composite, determined that the width of yarns a and the volume fraction v_f of fibers in the yarns was 1.39 mm and 72%, respectively. The average volume fraction of the fibers in this model very closely agrees with the volume fraction of the fibers in the actual composite determined from the acid digestion tests (see section 2.2).

The concept of the bridging model is based on the assumption that undulation regions in 8HS woven composites are separated by regions of a cross-ply laminate. First, the geometry of the repeating unit cell is simplified to obtain the square idealized unit cell. Next, the simplified unit cell is divided into five regions as shown in Figure 5. Four of these regions (B-E) may be considered as cross-ply laminates and their properties can be calculated from CLPT. The central (A) region contains the so-called undulation piece of the unit cell and its stiffness and thermal behavior can be accurately described by the crimp model. Having the properties of every region, the behavior of the entire unit cell can be determined in the following two steps. In the first step, the average properties of the three middle-bridging regions (A+B+C) are determined, assuming uniform strain and

curvature distributions. In the second step, the remaining two cross-ply regions (D, E) are joined together using the constant stress condition. In this manner, the properties of the entire 8HS unit cell can be evaluated, provided that the geometrical parameters as well as the stiffness and thermal expansion coefficient of the matrix and the yarns are known.

For the application of the bridging model, the properties of the tows must also be determined. It was assumed that each tow could be regarded as a unidirectional composite that was made from a visco-elastic polymer matrix reinforced by transversely isotropic graphite fibers with their properties independent of time and temperature. The properties of a unidirectional composite (stiffness properties Q_{tow} and CTEs) as a function of time and temperature were subsequently estimated using the Hashin equations [18].

The stiffness of the unit-cell $Q_{unit\ cell}$ at any given time and temperature is a function of both the polymer stiffness $Q_{polymer}$ and the tow stiffness Q_{tow} according to the equation below.

$$Q_{unit\ cell}(t, T) = f_Q(Q_{tow}(t, T), Q_{polymer}(t, T)) \quad (5)$$

Likewise, the thermal expansion coefficients of the unit-cell $\alpha_{unit\ cell}$ are dependent upon the stiffness and the CTE of both the polymer matrix and the tows according to equation (6):

$$\alpha_{unit\ cell}(t, T) = f_\alpha(\alpha_{tow}(t, T), \alpha_{polymer}(T), Q_{tow}(t, T), Q_{polymer}(T, t)) \quad (6)$$

It was found that the changes of $\alpha_{unit\ cell}$ with time are negligible and therefore equation (6) could be simplified to the following form:

$$\alpha_{unit\ cell}(T) = f'_\alpha(\overline{\alpha_{tow}}(T), \alpha_{polymer}(T), \overline{Q_{tow}}(T), \overline{Q_{polymer}}(T)) \quad (7)$$

where the bar denotes a time average. It should be understood that the functions f_Q and f'_α depend upon the assumed model of a woven material (the bridging model in the presented analysis). However, these functions cannot be derived explicitly due to the fact that the numerical integration was performed in order to obtain the stiffness properties of the crimp region (A). For this reason, both the stiffness matrix Q and the CTEs of the unit cell can be evaluated only for discrete values of time and temperature. The stiffness properties of the tows and the unit cell at room temperature and at 315°C as a function of time are shown in Figures 6a and 6b, respectively where Q_{ij} are the reduced stiffness constants of the tows and the unit cell. In addition, the CTEs for the PMR-15 resin, unidirectional tows (using the Hashin model) and the woven plies (from the bridging model) are presented in Figure 7 versus temperature.

Once the CTEs and the stiffness matrix $Q_{\text{unit cell}}$ of the woven plies at any given time during the post curing process are calculated, the CLPT [19] can be used to predict the interlaminar thermal residual stresses inside the polymer plies of the investigated 8HS laminate. The incremental approach, described in Refs. 1 and 7, was employed to solve the resulting integral equations. The convergence of the solution was checked by performing the calculations for a various number of time steps (from 6 up to 48 time steps covering the final stage of the post curing process). It was assumed that the residual stresses at 315°C of the post curing cycle were zero. The cooling rate was taken following the post curing process described in section 2.1. The $\epsilon_{11} = \sigma_{22}$ residual stress components as a function of the number of time steps are presented in Figure 8.

4.3 Numerical Residual Strains and Stresses in Al Inclusions

To account for the effect of multiple inclusion, the Eshelby method [20-21] along with the Tanaka-Mori theorem [22] were used to calculate the average thermal residual stresses and strains in the embedded Al inclusions. In order to simplify the calculations the following assumptions were made:

- perfect bonding exists between the aluminum inclusions and the surrounding polymer matrix,
- elastic constants and the CTE of aluminum do not depend on either time or temperature during the post curing process,
- all aluminum inclusions are spherical.

The average volume fraction of aluminum inclusion was taken to be $46 \pm 7.4\%$, as determined by SEM analysis (see Table 1). The following set of linear equations was used:

$$\sum_{i=0}^{f-1} C_I (S\varepsilon^T(i) + \varepsilon^R(i) + \varepsilon^{Res}(i+1) - \varepsilon^{Res}(i) - \varepsilon^{T*}(i)) = \sum_{i=0}^{f-1} C_M (\xi(f) - \xi(i)) (S\varepsilon^T(i) + \varepsilon^R(i) + \varepsilon^{Res}(i+1) - \varepsilon^{Res}(i) - \varepsilon^T(i)) \quad (8a)$$

$$\varepsilon^R(j) + V_f (S\varepsilon^T(j) - \varepsilon^T(j)) = 0, \text{ for } j=0, 1, 2, \dots, f \quad (8b)$$

$$\sigma_{inclusion}(f) = \sum_{i=0}^{f-1} C_I (S\varepsilon^T(i) + \varepsilon^R(i) + \varepsilon^{Res}(i+1) - \varepsilon^{Res}(i) - \varepsilon^{T*}(i)) \quad (8c)$$

where S is the Eshelby tensor for spherical Al inclusions, C_I is the tensor of the elastic constants of the Al inclusions, C_M is the time and temperature dependent tensor of the elastic properties of the matrix, ε^T is the stress free transformation strain, ε^{T*} is the stress free transformation strain of the inhomogeneous inclusion given by the product of the difference between CTE for an aluminum inclusion ($\alpha = 22.4 \cdot 10^{-6} \text{ } ^\circ\text{K}^{-1}$) and the polyimide matrix multiplied by the temperature change relative to the assumed stress free temperature (315°C), ε^R is the average strain caused by the presence of multiple Al inclusions, f is the number of time steps used in the numerical visco-elastic analysis, $\sigma_{inclusion}$ is the stress inside the aluminum inclusions, V_f is the average volume fraction of the Al inclusions, ξ is a so-called reduced time [7], and ε^{Res} is the average residual thermal strain in the matrix, which can be obtained using CLPT in conjunction with the

bridging model for the woven plies. In order to solve equations (8a-b), the numerical procedure similar to the one used in Refs. 1 and 7 was employed.

It is important to realize that the modified Eshelby model [20, 21] neglects the interactions between Al inclusions alone and Al inclusions and graphite fibers. One can visualize the model used as consisting of an infinite polymer matrix with embedded non-interacting spherical Al inclusions. The effect of woven plies on thermal residual stresses in Al inclusions was modeled by applying the constant strain ϵ^{Res} , which was assumed to be equal to the thermal residual strains in the polymer ply. The numerical value of the strain ϵ^{Res} was calculated in section 4.2. The Eshelby' assumption that the polymer matrix is extended to infinity should not generate substantial errors since the diameter of the aluminum inclusions was about an order of magnitude smaller than the thickness of the polymer layer between the woven plies.

Table 3a. X-ray and numerical strains inside aluminum inclusions without bending

X-ray Strains*			Numerical Strains*		
ϵ_{11}	ϵ_{22}	ϵ_{33}	ϵ_{11}	ϵ_{22}	ϵ_{33}
509 ± 108	517 ± 93	-376 ± 106	724 ± 35	724 ± 35	-988 ± 76

* all data in $\mu\epsilon$

Table 3b. X-ray and numerical stresses inside aluminum inclusions without bending

X-ray Data			Numerical Data		
σ_{11} [MPa]	σ_{22} [MPa]	σ_{33} [MPa]	σ_{11} [MPa]	σ_{22} [MPa]	σ_{33} [MPa]
67 ± 16.9	67.4 ± 17.1	20.5 ± 18.6	66.5 ± 10.9	66.5 ± 10.9	-23.4 ± 13

The residual strains and stresses in the Al inclusions determined from the model are presented in Tables 3a and 3b and compared with the data obtained from the XRD measurements. In addition, the close range strains and stresses, caused by the mismatch in the stiffness properties and CTEs of the polymer matrix and the Al inclusions, were

also determined. These stresses at room temperature for the volume fraction of inclusions used were found to be $\sigma_{11} = \sigma_{22} = \sigma_{33} = -14.2$ MPa.

4.4 Residual Stresses in the Composite from the X-ray strains

As already shown in Refs. 1 and 2, if the state of stress in the embedded Al inclusions is measured using the XRD technique, the residual stress in the polymer matrix ϵ^{Res} can be calculated without using CLPT. In order to do so, the special case of equations (8) was used with $\epsilon^{\text{Res}}(f)$ considered as an unknown and both $\epsilon^{\text{Res}}(i-1)$ and $\epsilon^{T^*}(i-1)$ equal to zero for $i = 1, \dots, f$.

In order to correctly determine the residual stresses in the polymer layer from the X-ray strains in the inclusions, the contribution from the close range stresses should also be considered. The procedure for the determination of the residual stresses in the polymer from XRD data can be summarized as follows:

1. Use equations (8a-b) to model the final stage of the post curing cycle, assuming that ϵ^{Res} is zero for each i . The resulting stresses are the close range stresses in the inclusions.
2. For a fixed value of the index i (no summation) corresponding to $T = 30^\circ\text{C}$ and $\sigma_{\text{Inclusion}}$ equal to the stress that was obtained from XRD minus the stress calculated in step 1 (close range stresses), use equations (8a-b) to calculate ϵ^{Res} at $T = 30^\circ\text{C}$
3. From ϵ^{Res} calculate σ^{Res} at room temperature and compare with the residual stress from CLPT.

Table 4. Interlaminar residual stresses in the 8HS composite from XRD measurements and the Eshelby model as well as from CLPT obtained with linear-elastic and visco-elastic assumptions.

	X-ray with Eshelby			Plate theory		
	σ_{11} [MPa]	σ_{22} [MPa]	σ_{33} [MPa]	σ_{11} [MPa]	σ_{22} [MPa]	σ_{33} [MPa]
Linear elastic (*)	70.7 ± 17	71.1 ± 17	36.7 ± 16	94	94	0
Visco-elastic (**)	67.3 ± 17	67.6 ± 16	33 ± 16	63.1	63.1	0

(*) for $\alpha = 44.8 \cdot 10^{-6} \text{ } ^\circ\text{K}^{-1}$ and $G = 1.6 \text{ GPa}$ (properties of PMR-15 at room temperature)

(**) for 48 time steps with $\alpha = f(T)$ and $G = f(t, T)$

The thermal residual stresses in the 8HS composite determined from CLPT and from the XRD measurements are shown in Table 4. The results presented in Table 4 were obtained with two assumptions. In the first case the computations were performed under linear elastic conditions (with constant CTE and G for PMR-15) whereas in the second case the computations were fully visco-elastic with the CTE and G for PMR-15 taken according to equations 2 and 3.

4.5 Total strains and stresses in the Al Inclusions as a function of bending

In the previous three sections the residual stresses and strains in the interlaminar regions of the 8HS composite as well as the residual stresses and strains in the embedded Al inclusions were determined without considering the effects of externally applied loads on the XRD measurements. An approach similar to that used in [2] for unidirectional graphite/polyimide composites can be used with the woven composites to determine how the externally applied loads influence the states of strain and stress in embedded crystalline inclusions.

The generalization of the Eshelby model that takes into consideration the presence of an external bending load is quite straightforward, since it requires only adding the additional

term $\varepsilon^{\text{Bend}}$ multiplied by the corresponding stiffness matrix to both sides of equation 8a in the last step of the recursive procedure. The magnitude of $\varepsilon^{\text{Bend}}$ inside a polymer ply could be easily calculated using the CLPT. It should also be pointed out that in the present analysis the stiffness tensor of the polymer matrix is constant since the changes of strain and stress in the Al inclusions are caused by four point bending applied at room temperature. In order to consider bending, the Eshelby equations can be written in the following forms:

$$\sum_{i=0}^{f-1} C_I \left(S\varepsilon^T(i) + \varepsilon^R(i) + \varepsilon^{\text{Res}}(i+1) - \varepsilon^{\text{Res}}(i) - \varepsilon^T(i) + \varepsilon^{\text{Bend}}(i) \right) = \sum_{i=0}^{f-1} C_M (\xi(f) - \xi(i)) \left(S\varepsilon^T(i) + \varepsilon^R(i) + \varepsilon^{\text{Res}}(i+1) - \varepsilon^{\text{Res}}(i) - \varepsilon^T(i) + \varepsilon^{\text{Bend}}(i) \right) \quad (9a)$$

$$\varepsilon^R(j) + V_f \left(S\varepsilon^T(j) - \varepsilon^T(j) \right) = 0, \text{ for } j=0, 1, 2, \dots, f \quad (9b)$$

$$\sigma_{\text{inclusion}}(f) = \sum_{i=0}^{f-1} C_I \left(S\varepsilon^T(i) + \varepsilon^R(i) + \varepsilon^{\text{Res}}(i+1) - \varepsilon^{\text{Res}}(i) - \varepsilon^T(i) + \varepsilon^{\text{Bend}}(i) \right) \quad (9c)$$

where the strain $\varepsilon^{\text{Bend}}$ is equal to zero for all values of i , except for $i = f$, and $\varepsilon^{\text{Bend}}(f)$ can be calculated using classical laminated plate theory. Of course the strain $\varepsilon^{\text{Bend}}$ is not constant inside a polymer ply, but it was assumed to be so in the Eshelby analysis. This assumption was made because of the fact that the thickness of the polymer layer ($50 \mu\text{m}$) was much smaller than the thickness of the whole laminate; therefore the changes in the strains along the x_3 direction could not cause substantial errors.

The numerical strains and stresses inside the Al inclusions caused by the combined effect of residual thermal stresses in the composite and the stresses generated by bending are shown in Figures 9a and 9b as functions of the axial strain as measured by a strain gage on the tensile side of the specimen. Despite large scatter in the data some trends are clearly visible. First of all, the ε_{11} and ε_{22} strain components follow quite closely the numerical prediction (see Figure 9a). Obviously, bending generates slightly different ε_{11} and ε_{22} except at an axial strain equal to zero (no bending). However, there is a large

difference between the experimentally and numerically determined ϵ_{33} strain components. Similar to the strains, the stresses in the inclusions also follow the numerical data quite well with the exception of the σ_{33} stress component, which significantly diverges from the numerical predictions (see Figure 9b).

One of the reasons why the XRD bending tests were performed was to further verify the experimental and numerical results obtained from the tests without bending. This can be accomplished by comparing the stress and strain data in the inclusions from the two tests if the tests with and without bending are treated independently. The stresses and strains inside the inclusions obtained from the tests with bending should converge to the stresses and strains in the inclusions from the tests without bending if the axial strain generated by the fixture is zero. In a perfect case the residual stresses in the laminate obtained from all the XRD data from the tests with bending should be exactly the same as the residual stresses in the composite determined from the tests without bending. This will be further discussed in the section below.

5. Discussion

The methodology developed in Refs. 1 and 2 for the determination of residual stresses in unidirectional polymer matrix composites was successfully applied in this study to evaluate thermal residual interlaminar stresses in an 8HS woven graphite/PMR-15 composite. The residual thermal stresses for the unidirectional graphite/PMR-15 composite presented in Refs. 1 and 2 can be compared with the residual stresses for the woven 8HS material. This comparison is meaningful since the composite constituents of the two systems are the same and the same manufacturing process was used in both cases. Furthermore, the analytical and experimental techniques used to evaluate the stresses were also the same for the two composite systems. The comparison is shown in Table 5.

Table 5. Comparison between the interlaminar residual stresses in the unidirectional [1,2] and woven (8HS) graphite/PMR-15 composites.

	Excluding bending			Including bending			Area fraction of Al inclusions*
	σ_{11} [MPa]	σ_{22} [[MPa]]	σ_{33} [MPa]	σ_{11} [MPa]	σ_{22} [MPa]	σ_{33} [MPa]	
unidirectional	53.5 ± 9	39.6 ± 8	25 ± 5	55 ± 6	40.5 ± 5	26.6 ± 4	$40 \pm 7\%$
8HS woven	67.3 ± 17	67.6 ± 16	33 ± 16	62.3 ± 8	61.7 ± 8	27.6 ± 7	$46 \pm 7.4\%$

* from SEM cross-sections.

Two sets of data for the unidirectional and woven composites are shown in Table 5. The first set represents the interlaminar residual stresses from the XRD experiments, with the application of the visco-elastic Eshelby method, obtained from the specimens tested without externally applied four point bending. The second set represents the residual stresses obtained from the specimens tested with and without bending (all results). The agreement between the two sets of data is quite good. It can therefore be concluded that the XRD tests with and without bending provided close estimates of the residual stresses in the composite within measurement error.

It can also be observed in the data presented in Table 5 that the residual stresses in the unidirectional graphite/PMR-15 composite are noticeably lower than for the woven composite. This is not surprising since the relaxation of the stresses in the woven composite during the final stages of the post curing process must have been significantly constrained by the presence of graphite fibers in both the 11 and 22 directions. It can also be noticed that the σ_{11} and σ_{22} stress components for the woven material are almost the same.

Another important observation that can also be made is the fact that the state of stress in the polymer matrix between either the unidirectional or woven plies is three dimensional in nature with significant tensile stresses (σ_{33}) present in the specimen thickness direction. As can be noticed in the data presented in Table 4, CLPT does not provide the

stresses in this direction since it assumes plate stress conditions. The σ_{33} stresses are caused by the fact that the thickness of the polymer layers between either the unidirectional or woven plies is not constant and can vary substantially along the specimens. This effect has been thoroughly discussed in Ref. 1 for the case of the unidirectional system. The fact that plain stress conditions were assumed in the CLPT computations can also be seen in the data presented in Figures 9a,b. The actual three-dimensional state of stresses in the interlaminar regions of the woven composite was responsible for the large differences between the numerical and experimental ε_{33} and σ_{33} strain and stress components in the Al inclusions subjected to bending.

The noticeable scatter observed in the X-ray strains and stresses in the embedded Al inclusions determined from the tests with and without bending is related to the uneven distribution of the inclusions in the interlaminar regions of the composite. This scatter affects obviously the final estimates of the residual stresses in the composite from the XRD measurements and the Eshelby model. The noticeable variations in the determined residual stresses in the inclusions and the composite could be significantly minimized by optimize the inclusion distributions by making them more uniform. From the composite manufacturing point of view, however, this is not a straightforward task.

Conclusions

1. It has been shown in this research that the thermal residual interlaminar stresses can be determined in woven 8HS graphite/PMR 15 composites using the methodology developed in Refs. 1 and 2 based on the XRD measurements of residual strains in embedded metallic inclusions. The stresses are three dimensional in nature with significant stresses present between the woven plies in the thickness direction of the specimen.
2. There is a good agreement between the thermal residual stresses in the directions of the tows determined from the XRD measurements in conjunction with application of the

visco-elastic Eshelby model for multiple inclusions, with the stresses from the visco-elastic plate theory. Only the stresses through the thickness are entirely different.

3. The thermal residual stresses in the interlaminar regions of the 8HS woven graphite/PMR-15 composite are noticeably higher than in the case of the unidirectional system. Especially, the large tensile stresses along the tows (62.3 ± 8 MPa) might create cracking of the polyimide layers in service since they are only slightly lower than the tensile strength of the PMR-15 resin, which is approximately 80 MPa. They might be even higher in graphite/polyimide composite structures subjected to large temperature variations in-service.

References

1. B. Benedikt, M. Kumosa, P.K. Predecki, L. Kumosa, M.G. Castelli and J. K. Sutter, An Analysis of Residual Thermal Stresses in a Unidirectional Graphite/PMR-15 Composite Based on the X-ray Diffraction Measurements, *Composite Science and Technology*, in press.
2. B. Benedikt, P. K. Predecki, L. Kumosa, D. Armentrout, J. K. Sutter and M. Kumosa, The Use of X-ray Diffraction Measurements to Determine the Effect of Bending Loads on Internal Stresses in Aluminum Inclusions Embedded in a Unidirectional Graphite Fiber /PMR-15 Composite, *Composites Science and Technology*, in press.
3. H. E. Gascoigne, Residual Surface Stresses in Laminated Cross-ply Fiber-epoxy Composite Materials, *Experimental Mechanics*, vol. 34, p. 27-36, 1994
4. H. Fukuda, K. Takahashi and S. Toda, Thermal deformation of Anti-symmetric Laminates at Cure, *Proc. ICCM-10*, vol. 3, p. 141-148, 1995

5. P. G. Ifju, X. Niu, B. C. Kilday, S. C. Liu and S. M. Ettinger, Residual Stress Measurement in Composite Using the Cure-referencing Method, *Experimental Mechanics*, vol. 40, p. 22-30, 2000
6. G. Jeronimidis and A. T. Parkyn, Residual Stress in Carbon Fiber-Thermoplastic Matrix Laminates, *Journal of Composite Materials*, vol. 22, p. 401- 415, 1988
7. T. M. Wang and M. Daniel, Thermoviscoelastic Analysis of Residual Stresses and Warpage in Composite Laminates, *Journal of Composite Materials*, vol. 26, p. 883-899, 1992
8. S. R. White and Y. K. Kim, Process-Induced Residual Stress Analysis of AS4/3501-6 Composite Material, *Mechanics of Composite Materials and Structures.*, vol. 5, p.153-186, 1998
9. P. Predecki and C. S. Barrett, Stress Measurement in Graphite/Epoxy Composites by X-ray Diffraction from Fillers, *J. Comp. Mat.*, vol. 13, p. 61-71, 1979
10. P. Predecki, C. S. Barrett, Residual Stresses in Resin Matrix Composites, In E. Kula, editor, *28th Sagamore Army Materials Research Conference*, p. 409-424, Lake Placid, July 13-17 1981
11. C. S. Barrett and P. Predecki, Stress Measurements in Graphite/Epoxy Uniaxial Composites by X-rays, *Polymer Composites*, vol. 1, p. 2-6, 1980
12. I. C. Noyan and J. B. Cohen, Residual Stress. Measurement by Diffraction and Interpretation. Springer-Verlag, New York, 1987
13. G. D. Roberts, D. C. Malarik and J. O. Robaidek Viscoelastic Properties of Addition-Cured Polyimides Used in High Temperature Polymer Matrix Composites, Composites Design, Manufacturing, and Applications; *Proceedings of the Eight International*

Conference on Composite Materials, S. W. Tsai and G. S. Springer, Eds., Society for Advanced Materials and Process Engineering, Covina, CA 1991, p. 12-H-1 to 12-H-10

14. T. Ishikawa and T.W. Chou, Nonlinear Behavior of Woven Fabric Composites, *Journal of Composite Materials*, vol. 17, p.399-413, 1983
15. T. Ishikawa and T.W. Chou, In-plane thermal expansion and thermal bending coefficients of fabric composites, *Journal of Composite Materials*, vol. 17, p.92-104, 1983
16. T. W. Chou, Microstructural design of fiber composites, *Cambridge University Press*, Cambridge 1992
17. K. Searles, G. Odegard, M. Kumosa, Micro- and mesomechanics of 8-harness satin woven fabric composites: I- evaluation of elastic behavior, *Composites: Part A applied science and manufacturing*, in press.
18. Z. Hashin, Analysis of Properties of Fiber Composites with Anisotropic Constituents, *Journal of Applied Mechanics*, vol. 46, p. 543-550, 1979
19. J. N. Reddy, Mechanics of Laminated Composite Plates. Theory and Analyses., CRC Press, 1997
20. J. D. Eshelby, The Determination of the Elastic Field of an Ellipsoidal inclusion, and Related Problems, *Proc. R. Soc. London*, vol. A241, p. 376-396, 1957
21. T. Mura, *Micromechanics of Defects in Solids*, 2nd edition, Martinus Nijhoff Publishers, Dordrecht, 1987
22. T. Mori and K. Tanaka, Average Stress in Matrix and Average Elastic Energy of Materials with Misfitting Inclusions, *Acta Metall.*, vol. 21, p. 571-574, 1973

Acknowledgements

This research has been supported by the Air Force Office of Scientific Research and NASA Glenn research Center under grants F49620-1-0426 (AFOSR) and F49620-00-1-0159 (AFOSR and NASA).

Table and Figure Captions

Table 1. Area fraction of Al inclusions in %.

Table 2. X-ray diffraction data as a function of axial strain.

Table 3a. X-ray and numerical strains (a) and stresses (b) inside aluminum inclusions without bending.

Table 4. Interlaminar residual stresses in the 8HS composite from XRD measurements and the Eshelby model as well as from CLPT obtained with linear-elastic and visco-elastic assumptions.

Table 5. Comparison between the interlaminar residual stresses in the unidirectional [1,2] and woven (8HS) graphite/PMR-15 composites.

Figures 1a,b. Aluminum inclusions distributed between the first and second plies of the 8HS composite.

Figure 2. The definition of angles ϕ and ψ with respect to the specimen coordinate system X_1 , X_2 and X_3 .

Figure 3. X-ray four point bend tests; (a) four point bend fixture mounted on the Siemens D-500 goniometer and (b) specimen configuration inside the fixture.

Figure 4(a-d). Examples of plots of $\epsilon_{\phi\psi}$ as a function of $\sin^2(\psi)$ for two different values of axial strain; (a) $\epsilon = 900 \mu\varepsilon$, $\phi = 0^\circ$, (b) $\epsilon = 900 \mu\varepsilon$, $\phi = 90^\circ$, (c) $\epsilon = 2000 \mu\varepsilon$, $\phi = 0^\circ$, (d) $\epsilon = 2000 \mu\varepsilon$, $\phi = 90^\circ$

Figure 5. Crimp and bridging models

Figure 6. Q Reduced stiffness constants Q_{ij} versus time for the unidirectional tows and the unit cell at room temperature and at 315°C .

Figure 7. Thermal expansion coefficients (CTEs) for the neat PMR-15 resin, unidirectional tows (from the Hashin model) and the woven plies (from the unit cell)

Figure 8. Interlaminar residual stresses obtained from visco-elastic CLPT as a function of the number of time steps.

Figure 9. X-ray and numerical strains and stresses inside Al inclusions as a function of ϵ_{11} ; (a) strains and (b) stresses.

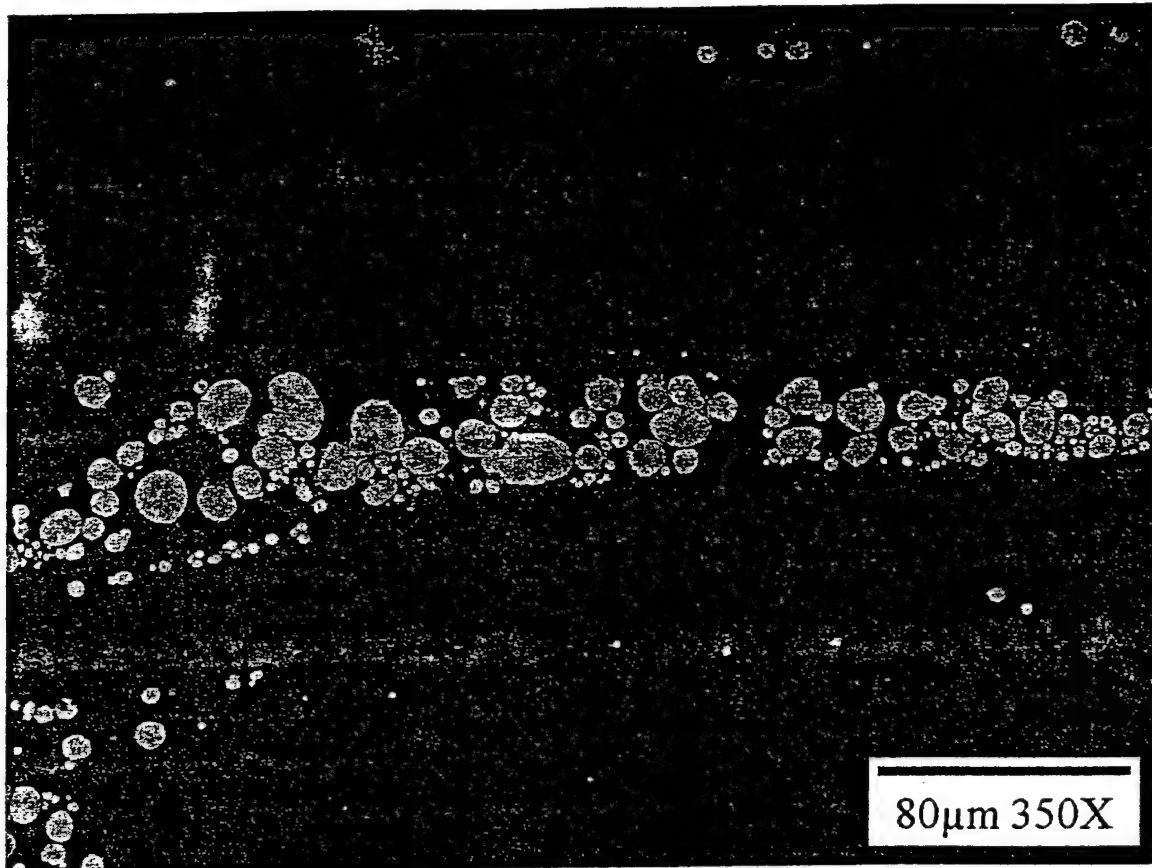


Figure 1a

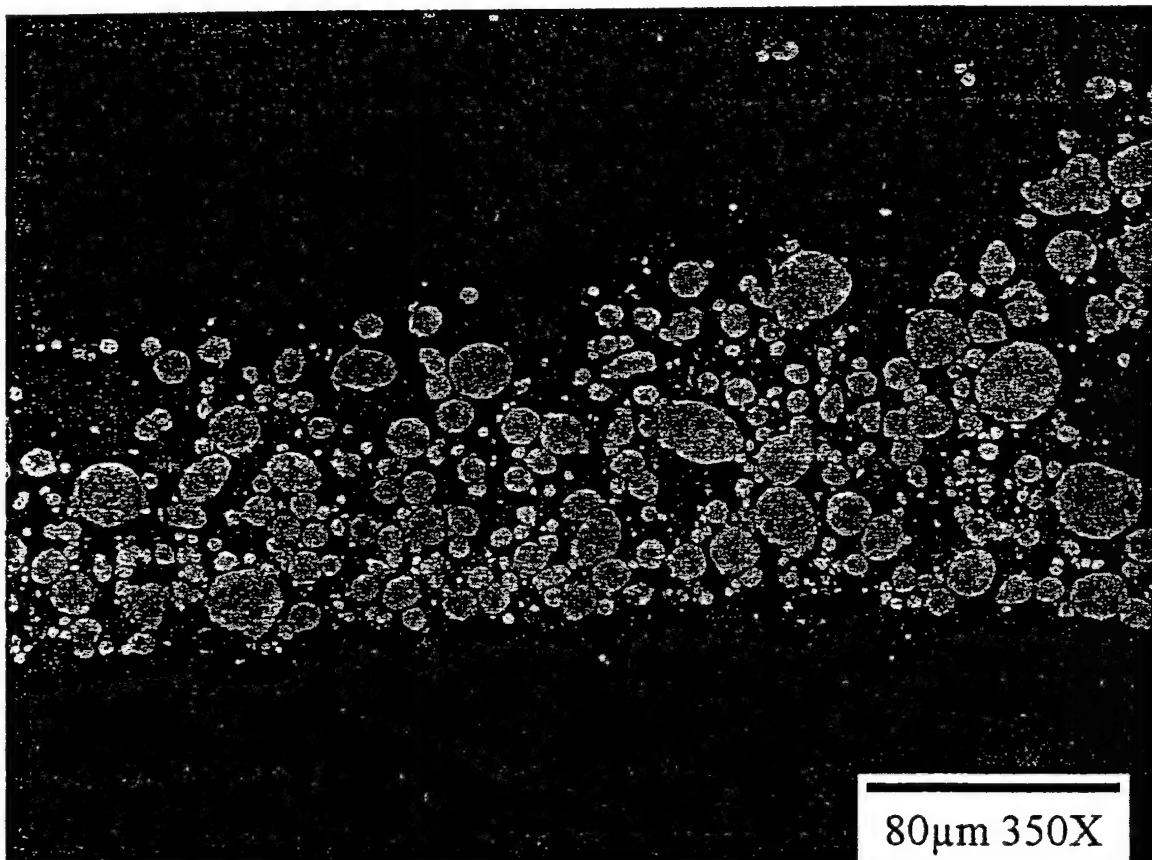


Figure 1b

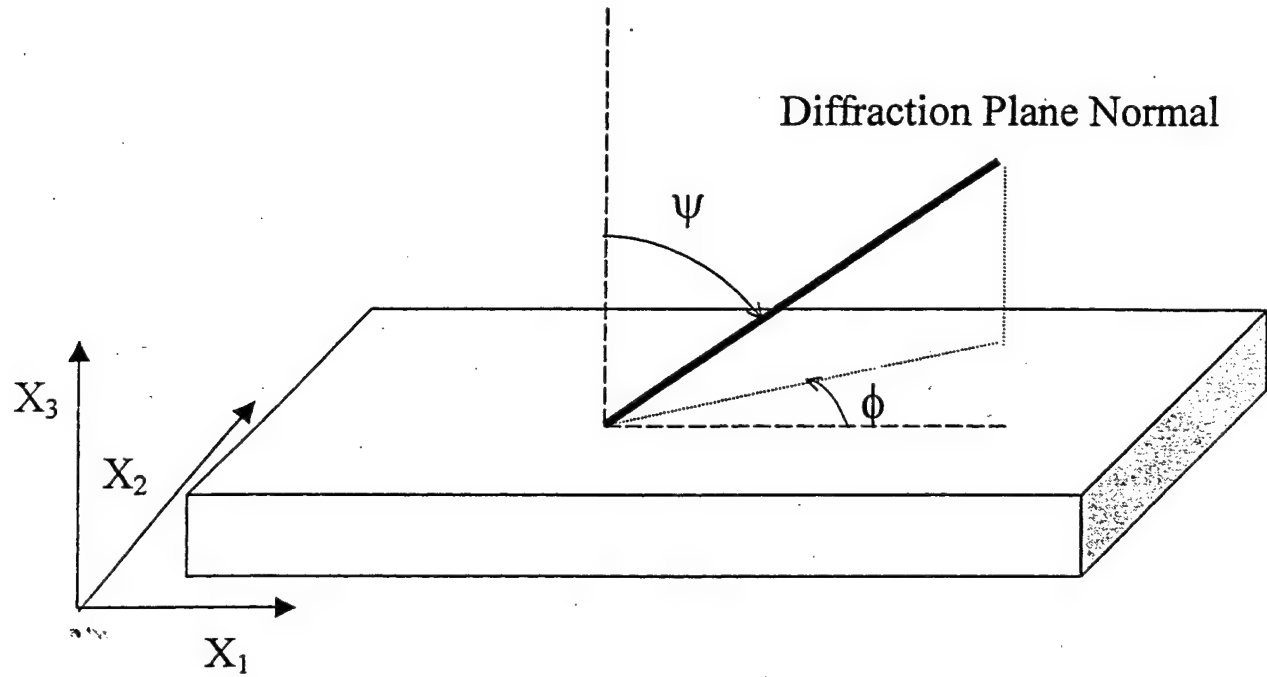


Figure 2

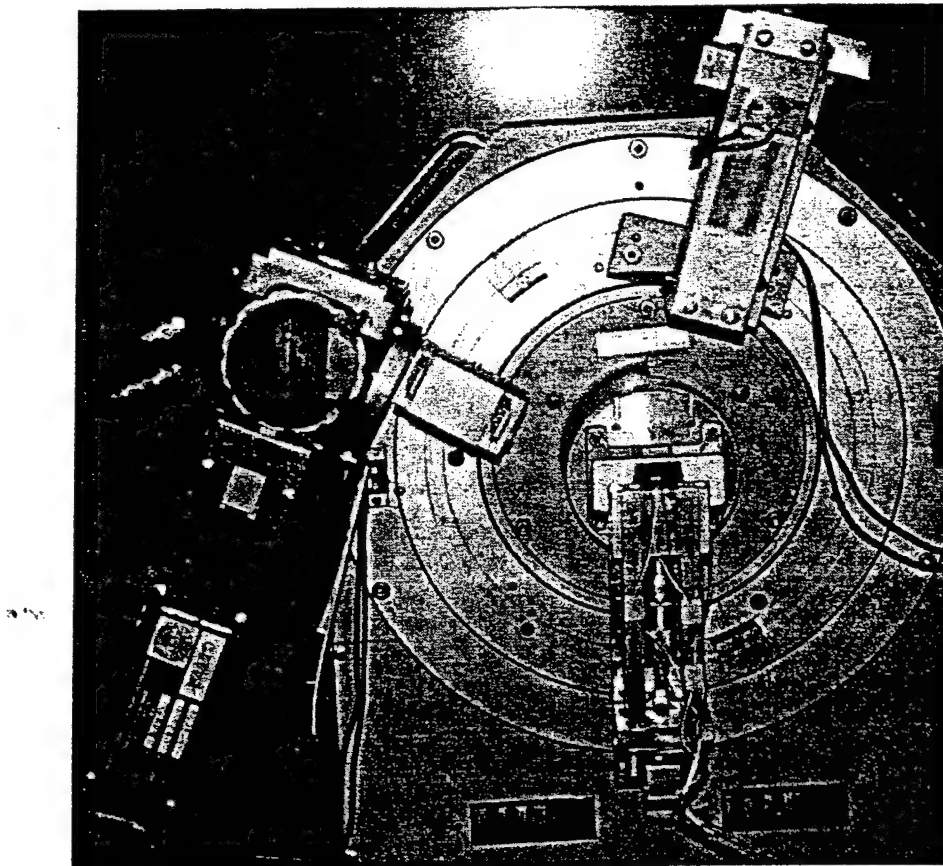


Figure 3a

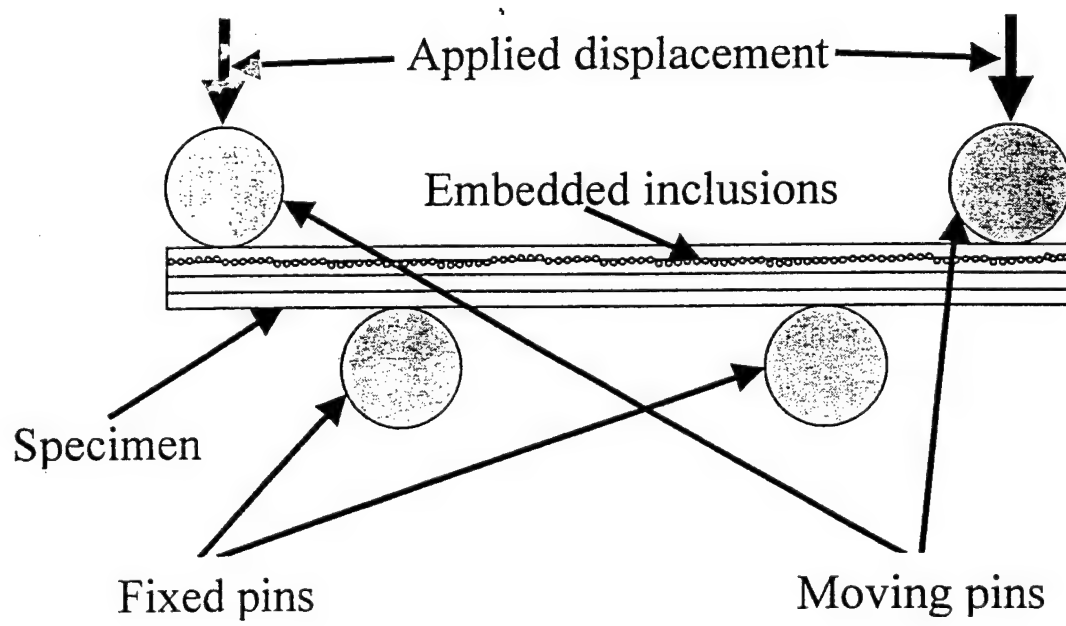


Figure 3b

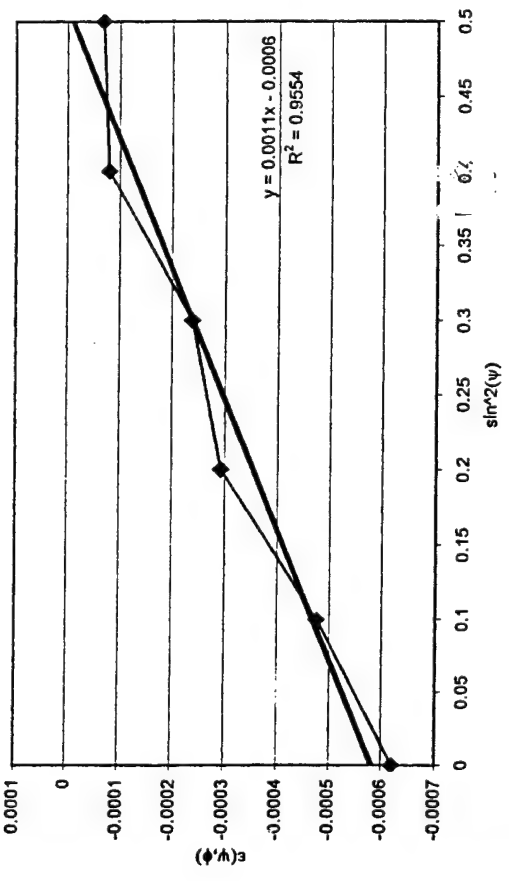


Figure 4a

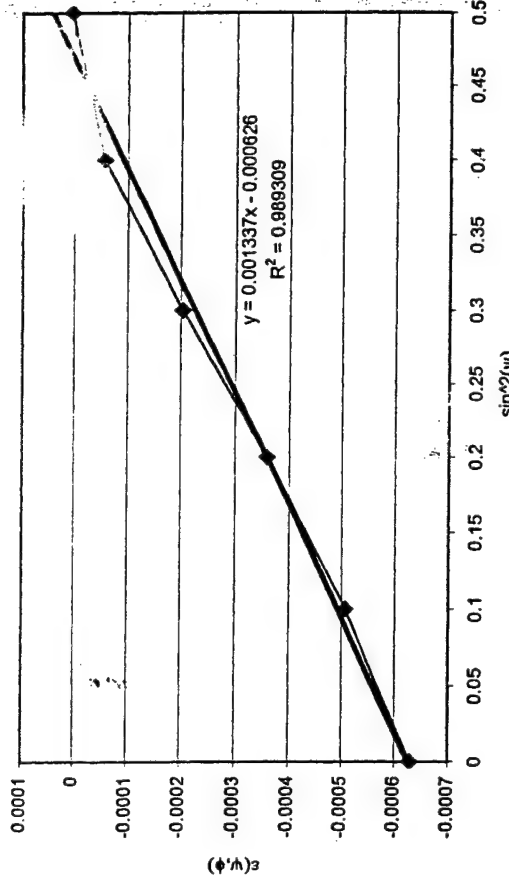


Figure 4c

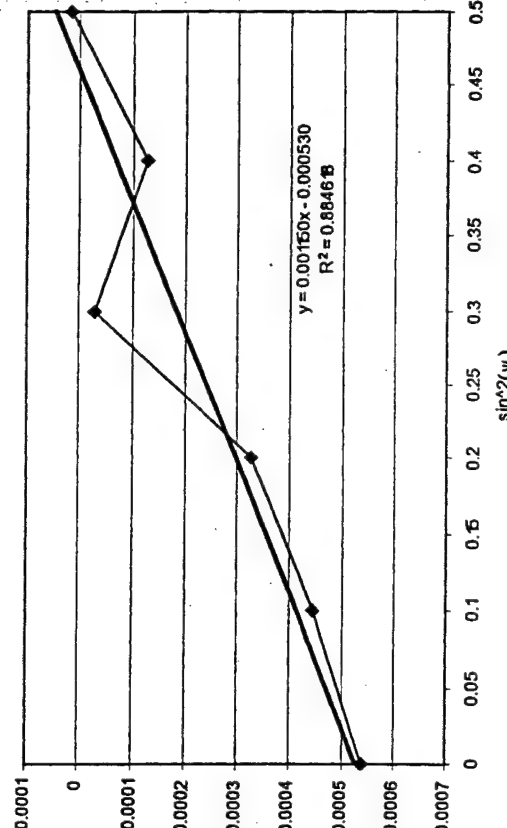
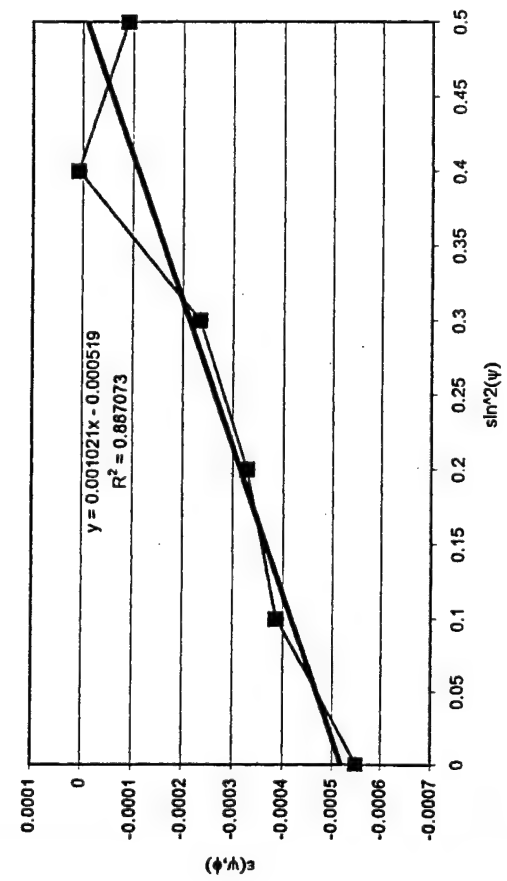


Figure 4d

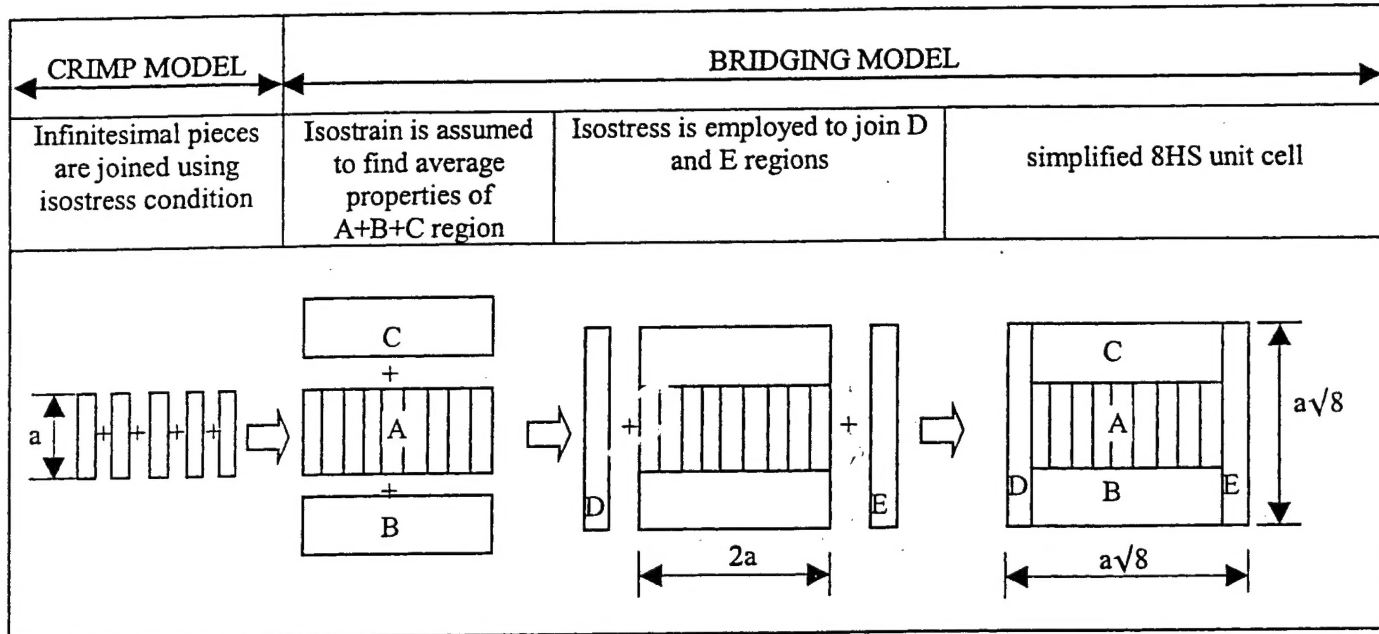


Figure 5

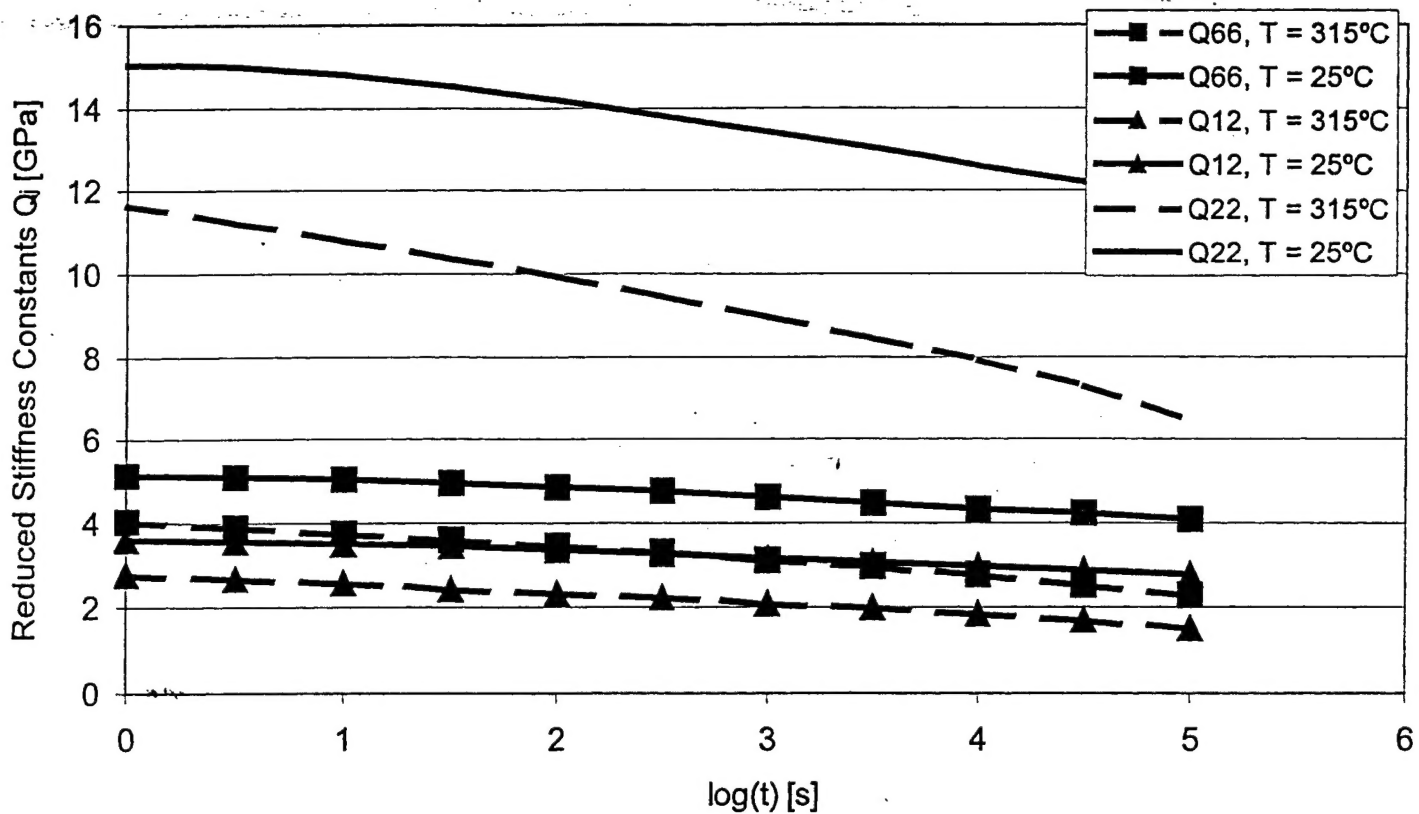


Figure 6a

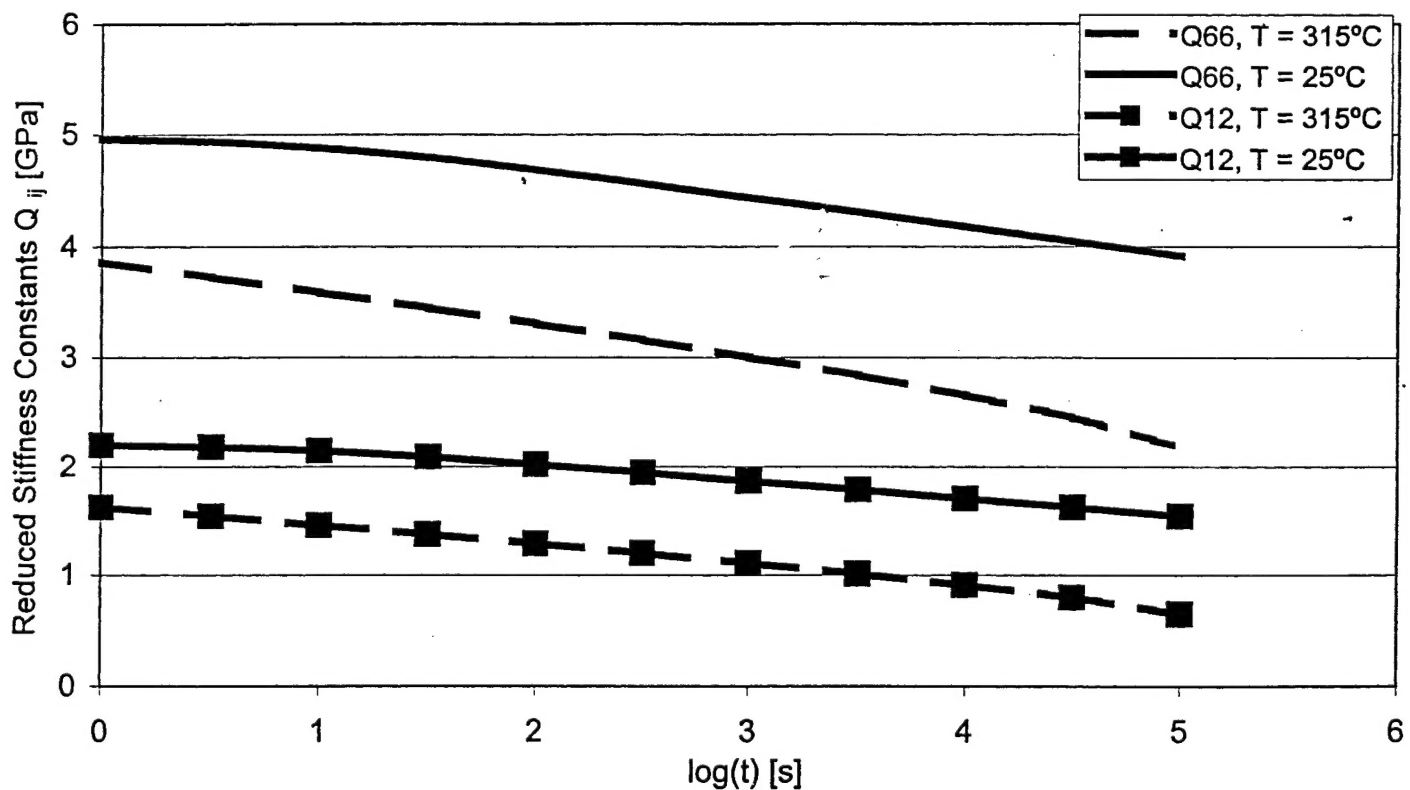


Figure 6b

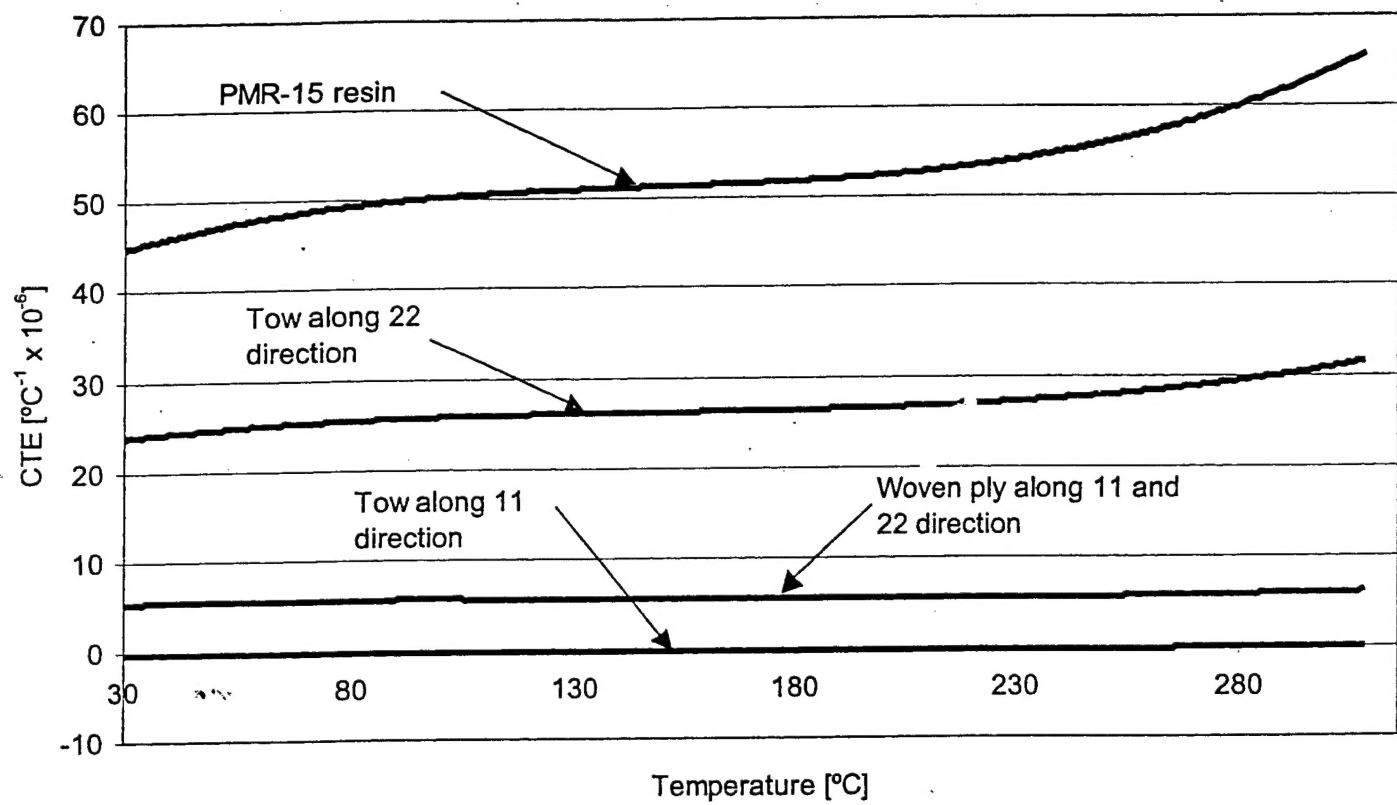


Figure 7

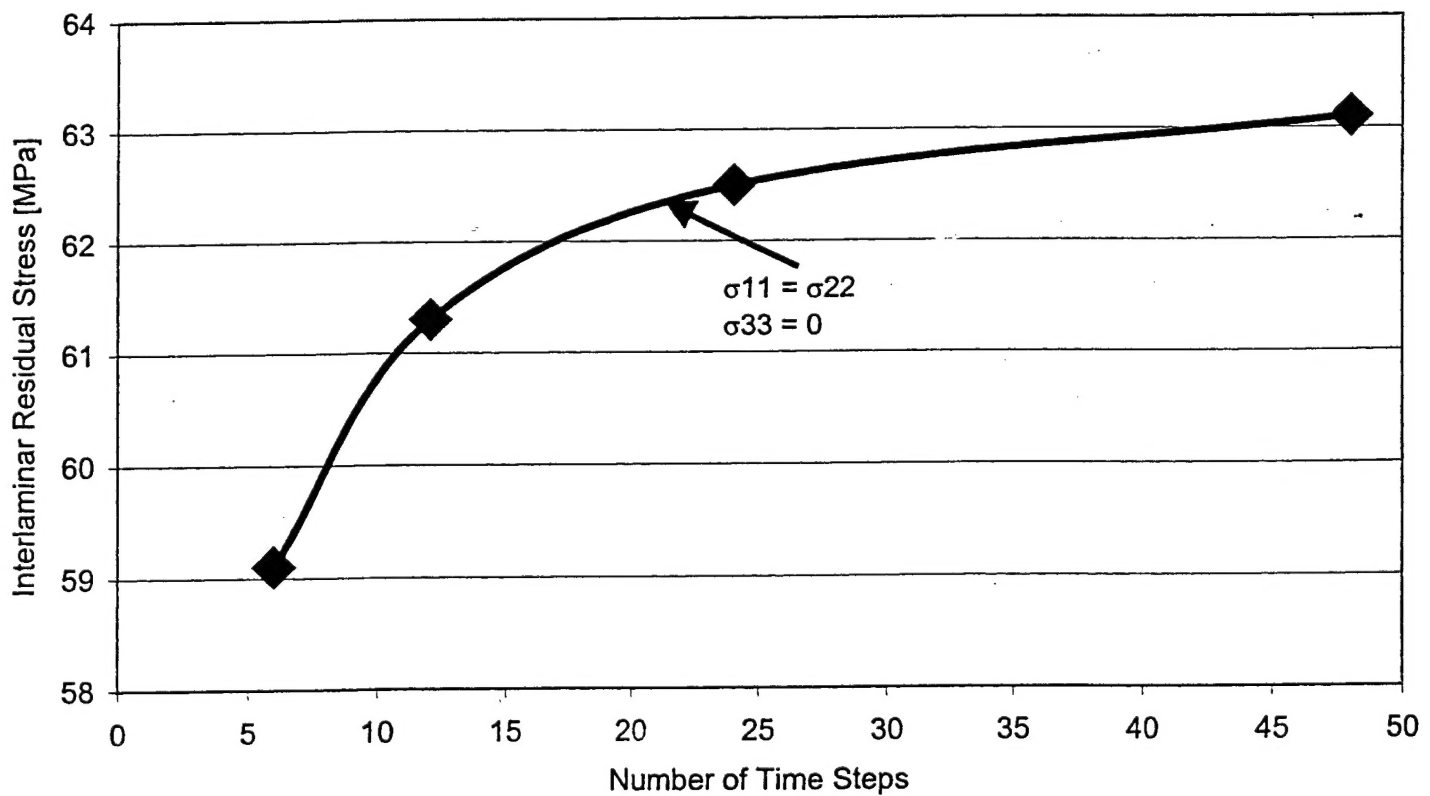


Figure 8

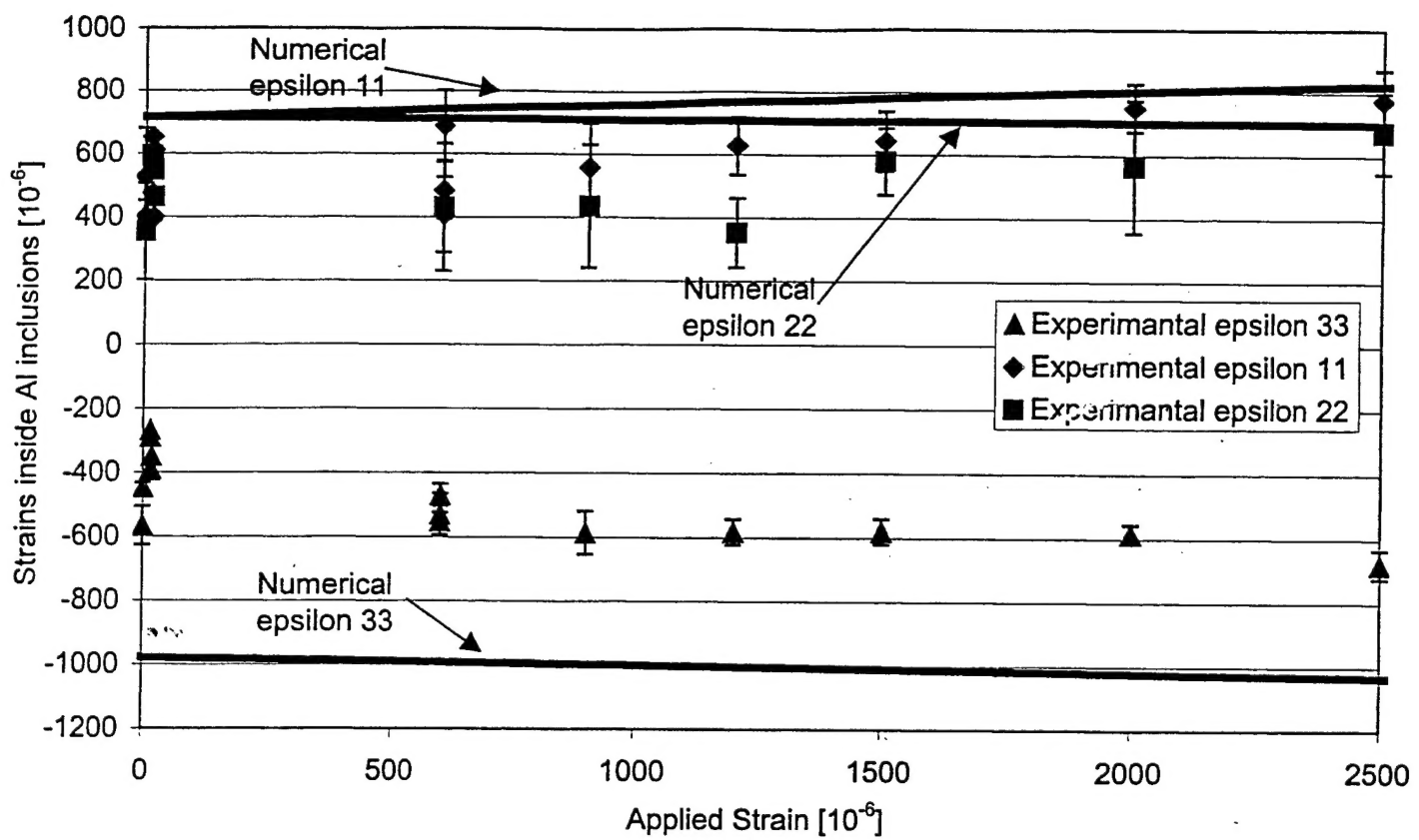


Figure 9a

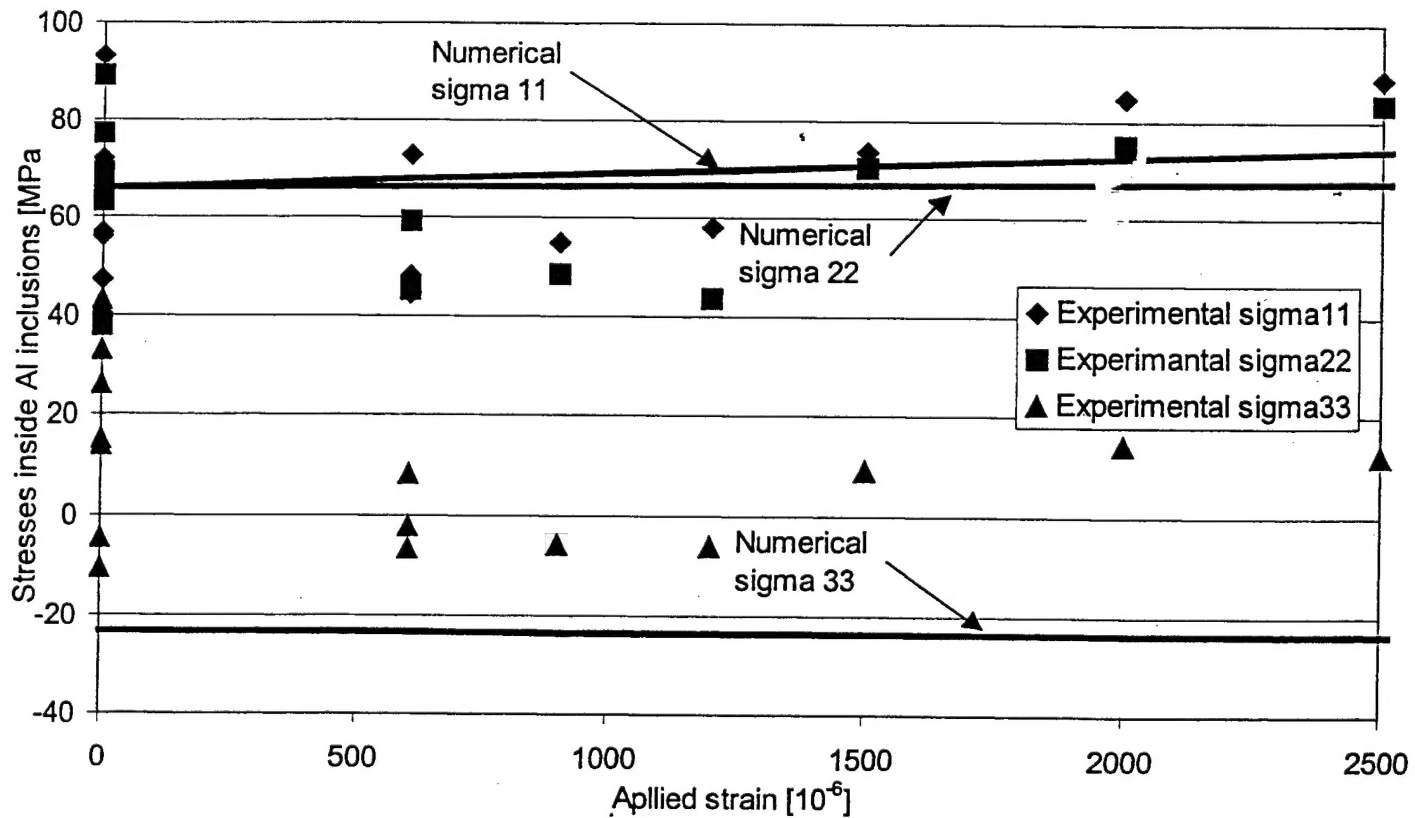


Figure 9b